

SCIENCE REQUIREMENTS DOCUMENT

MEASUREMENT OF VISCOSITY NEAR THE  
LIQUID-VAPOR CRITICAL POINT OF XENON

Robert F. Berg and Michael R. Moldover  
National Institute of Standards and Technology

7 December 1993

NATIONAL AERONAUTICS AND SPACE ADMINISTRATION

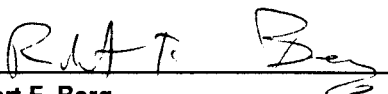
# SCIENCE REQUIREMENTS


FOR A  
SPACE FLIGHT EXPERIMENT  
ENTITLED

## CRITICAL VISCOSITY OF XENON

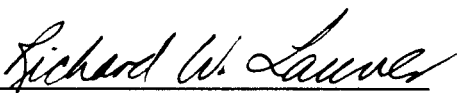
Document: 60009-DOC-006  
Revision: Initial  
Date: 5/3/94

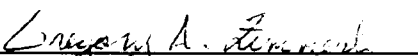
Prepared by:

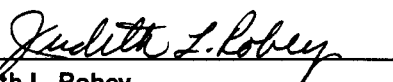
  
Robert F. Berg  
Principal Investigator  
National Institute for Standards  
and Technology, Gaithersburg, MD


  
Michael R. Moldover  
Co-Investigator  
National Institute for Standards  
and Technology, Gaithersburg, MD

Concurrence:


  
Richard W. Lauver  
Project Manager  
Space Experiments Division  
Lewis Research Center

  
Gregory A. Zimmerli  
Project Scientist  
NYMA/ADF  
Lewis Research Center

  
Judith L. Robey  
Program Manager  
Microgravity Science and Applications  
Division, NASA HQ

  
Brad M. Carpenter  
Program Scientist  
Microgravity Science and Applications  
Division, NASA HQ

Approved by:

  
Roger K. Crouch  
Chief Scientist  
Microgravity Science and Applications  
Division, NASA HQ

## SCIENCE REQUIREMENTS DOCUMENT

### MEASUREMENT OF VISCOSITY NEAR THE LIQUID-VAPOR CRITICAL POINT OF XENON

Robert F. Berg and Michael R. Moldover  
National Institute of Standards and Technology

7 December 1993

We propose to measure in low gravity the viscosity of xenon close to its critical point. The accuracy will be sufficient to eliminate uncertainties currently associated with the analysis of 1-g experiments. The measurements will provide the first direct observation of the predicted power-law divergence of viscosity in a pure fluid. The measurements will also strengthen Zeno's test of mode coupling theory by greatly increasing the reliability of the extrapolation of viscosity to low reduced temperatures. Our scientific objectives are described in more detail in one of the attached reports [1].

The low-gravity experiment will be the final stage of a program whose completed ground-based stages are: (1) theoretical studies by one of the principal investigators (MRM) and coworkers [2,3], (2) critical viscosity measurements of binary liquid mixtures [4], (3) critical viscosity measurements of pure fluids in 1-g [5,6], and development of a suitable vibration-insensitive viscometer [7]. Our technical approach is described in the draft Science Requirements Document [7].

One of us (MRM) has reviewed opportunities for critical phenomena research in low gravity [8,9]. Both of us were co-principal investigators in the Thermal Equilibration Experiment in the Critical Point Facility, flown on IML-1 in 1992. From this experience, and from the technical maturity of our ground-based work, we believe our critical point viscometer is ready for development as a flight experiment.

This Science Requirements Document consists of the original SRD supplemented by eight reports written in the last 14 months. The supplemental reports address issues raised at the Conceptual Design Review or in the following year. Their titles and the pertinent sections of the original SRD are listed below.

<u>Abbreviated report title</u>	<u>SRD section</u>
Scientific objectives	2E
Temperature gradients on the cell wall	4E
Shuttle's vibration environment	4F
Calibration of the oscillating screen viscometer	4G
Nonhydrodynamic characteristics of the oscillator	4G
Effect of bulk viscosity	4G
Need for communication during flight	5C
Feasibility of electrostriction for detecting $T_c$	7

The viscometer's design has undergone several small changes since the Conceptual Design Review. The most important is the exclusion of any independent means for locating the critical temperature in orbit. The report on electrostriction contains more detail. Other changes include changing the material of the electrodes from indium-coated glass to brass and adding a conductive coating to the sapphire window. The conductive coating was found necessary to eliminate an oscillator nonlinearity associated with charge fixed on the window.

The most important procedural change is the technique for calibration of the viscometer. Because the oscillator is overdamped, it is effectively self-calibrating for measurements of viscosity relative to a reference state of the sample. This concept has been demonstrated by measurements described in the report on calibration.

References

1. R.F. Berg and M.R. Moldover, report to NASA (1992).
2. M.R. Moldover, J.V. Sengers, R.W. Gammon, and R.J. Hocken, Rev. Mod. Phys. 51, 79 (1979).
3. M.R. Moldover, R.J. Hocken, R.W. Gammon, and J.V. Sengers, Overviews and Justifications for Low Gravity Experiments on Phase Transition and Critical Phenomena in Fluids, NBS Technical Note 925 (U.S. Government Printing Office, 1976); also published as NASA Contractor's Report CR-135070.
4. R.F. Berg and M.R. Moldover, Int. J. Thermophys. 7, 675 (1986); J. Chem. Phys. 89, 3694 (1988).
5. R.F. Berg and M.R. Moldover, J. Chem. Phys. 93, 1926 (1990).
6. R.F. Berg and M.R. Moldover, Phys. Rev. A 42, 7183 (1990).
7. R.F. Berg and M.R. Moldover, Science Requirements Document (1992).
8. M.R. Moldover and R.W. Gammon, NASA Contractor's Report CR174637 (1983).
9. M.R. Moldover, Opportunities for Research in a Low-Gravity Environment, ed. G. Hazelrigg and J.R. Reynolds (AIAA, New York, 1986).

SCIENCE REQUIREMENTS  
FOR THE  
CRITICAL VISCOSITY EXPERIMENT

Robert F. Berg and Michael R. Moldover  
Thermophysics Division, National Institute of Standards and Technology  
Gaithersburg, MD, 20899  
NASA Contract C-32001-K  
[6 October 1992]

## TABLE OF CONTENTS

1. INTRODUCTION	3
2. BACKGROUND	4
A. Critical phenomena	
B. Viscosity near the critical point	
C. Fluctuation relaxation time	
D. Previous work	
E. Objectives of the flight experiment and the connection to Zeno	
3. JUSTIFICATION FOR A LOW-GRAVITY EXPERIMENT	9
A. Stratification near the critical point	
B. Reducing stratification without space flight	
4. DESCRIPTION AND TESTS OF THE NEW VISCOMETER	11
A. The immersed oscillator	
B. General layout	
C. Sample cell	
D. Drive and detection electronics	
E. Thermostat design and operation	
F. Low-level vibration tests	
G. Hydrodynamic models of the oscillator	
H. Summary of the viscometer's tests	
5. REQUIREMENTS	26
A. Viscometer requirements	
B. Environment requirements	
C. Control and data requirements	
6. EQUILIBRATION: IS A STIRRER NEEDED?	31
A. Evolution of inhomogeneities induced by temperature gradients	
B. Validity of the equilibration model	
C. Four possible causes of density inhomogeneity	
D. Avoiding density gradients with a slow ramp	
E. Upper bound on density variations caused by temperature changes	
F. Miscellaneous concerns	
G. Stirrer requirements	
7. TURBIDITY FOR VERIFICATION OF $T_c$	41
A. $T_c$ defined by viscosity	
B. $T_c$ defined by turbidity	
C. Turbidity while crossing $T_c$	
D. Summary	
8. PROPOSED FLIGHT EXPERIMENT	45
A. Temperature vs. time	
B. Components	
9. INVOLVEMENT OF THE PRINCIPAL INVESTIGATORS	47
A. Supporting ground-based testing	
B. Preparation of the flight experiment	
C. Post-flight data analysis	
D. Reflights	
REFERENCES	48
FIGURE CAPTIONS	51

## 1. INTRODUCTION

The experiment proposed in this document is a series of measurements of the viscosity of xenon. What makes the measurements both interesting and worthy as a low-gravity experiment is performing them near the liquid-vapor critical point.

The low-gravity experiment would be the final stage of a program whose completed ground-based stages are: (1) theoretical studies by one of the principal investigators (MRM) and coworkers [1,2], (2) critical viscosity measurements of binary liquid mixtures [3], and (3) critical viscosity measurements of pure fluids in 1-g [4,5]. Our goal is to measure the viscosity of xenon close to its critical point with accuracy sufficient to eliminate uncertainties currently associated with the analysis of 1-g experiments. As shown by Fig. 1.1, the limits of gravity close to the critical point and of crossover to noncritical viscosity far from the critical point keep present experiments out of the asymptotic region close to the critical point. With gravity removed, we will be able to measure the critical exponent for viscosity to  $\pm 1\%$  without significant corrections from the theories of stratification and crossover.

Much of this document is a description of a new viscometer, dubbed the oscillating screen, developed specifically for a flight experiment. Our old viscometer, with which we successfully measured the viscosity of carbon dioxide and xenon [4], held the sample within a high-Q, 1 Hz, torsion oscillator. Unfortunately, as more information about the Shuttle's vibration environment became available during the last few years, it became clear that successful operation of the high-Q viscometer in orbit would require vibration isolation technology not yet developed [6]. Our new viscometer immerses the oscillator inside the sample. In so doing, the oscillator's Q has been reduced from about 1000 to less than one, with a comparable reduction in vibration sensitivity.

One of us (MRM) has reviewed opportunities for critical phenomena research in low gravity [7,8]. Both of us were co-principal investigators in the Thermal Equilibration Experiment in the Critical Point Experiment, flown on the Space Shuttle in January 1992. From this experience, and from the technical maturity of our ground-based work, we believe our critical point viscometer is ready for development as a flight experiment.

## 2. BACKGROUND

### A. Critical phenomena

A pure fluid such as water or carbon dioxide has an equilibrium vapor–liquid curve in the pressure–temperature plane which extends upward from the triple point to the critical point (Fig. 2.1). At the critical point, the liquid and vapor phases become indistinguishable. A thought experiment useful for visualizing an approach to the critical point is to imagine a sealed container filled roughly halfway with water and slowly heated up to its critical temperature  $T_c$ . The density of the vapor will increase due to evaporation while the liquid density will decrease due to thermal expansion. If just the right amount of water is put into the container (namely the critical density) then the liquid–vapor meniscus will rise from about 1/3 of the container height to the middle. At the critical temperature, the two phases will become identical in all respects.

Much of our quantitative understanding of the behavior of fluids both near and far from  $T_c$  is due to the work of Van der Waals and others who were stimulated by his creation of the equation of state which bears his name [9]. In particular, mathematical descriptions of various features of the phase diagram (coexistence curve, critical isotherm, etc.) and derived thermodynamic properties (e.g. heat capacity) are made possible through simple assumptions about the equation of state and its derivatives at the critical point. However, the validity of these descriptions was known to be limited by experiment from even the time of Van der Waals [10]. More than a half century passed before the necessary generalizations of fluid equations of state were made which allowed this rift between theory and experiment to begin healing.

An important stimulus for the new theories was the experimental discovery by Voronel and coworkers [11] in the early 1960's of a singularity in the heat capacity of gases near the liquid–vapor critical point. This was not predicted by the "classical" theories which assumed that the equation of state was always an analytic function of temperature and density. Generalization by Widom [12] of the classical equation of state to allow nonanalyticity led to the modern theories which have been successful at describing thermodynamic experiments even very near the critical point. In the last twenty years theory, experiment, and computer simulations have come together to yield a consistent description of static fluid properties near the critical point. Three reviews of this progress are given by References 13–15. Reference 10 is a concise history of critical phenomena studies from the time of Van der Waals.

To understand the non-analytic behavior of fluid properties near the critical point it is helpful to consider what happens to the microscopic structure of a fluid near the critical point. In particular consider again the container of water sealed at the critical density. As  $T_c$  is approached from below, the free energies of the liquid and vapor phases become similar so that the energy needed to create a vapor bubble in the liquid phase (or a liquid droplet in the vapor phase) approaches zero. These spontaneous fluctuations in density of both the liquid and the vapor phase become large close to  $T_c$ . The characteristic size  $\xi$  of the density fluctuations is called the "correlation length" and this size diverges at the critical temperature according to

$$\xi = \xi_0 \epsilon^{-\nu}, \quad (1)$$

when  $T_c$  is approached from below as visualized above. If  $T_c$  is approached from high temperatures at constant density (as in the Critical Viscosity Experiment), then

$$\xi = \xi_0 \epsilon^{-\nu}. \quad (2)$$

In Eqs.(1) and (2),

$$\epsilon \equiv |T-T_c|/T_c \quad (3)$$

is the "reduced temperature" and  $\xi_0^-$  and  $\xi_0$  are constants. Because the exponent  $\nu$  is not equal to 1 (as in the Van der Waals theory) this divergence of the correlation length is a manifestation of the nonanalytic behavior of the correlation function and can be viewed as the origin of the divergences of thermodynamic properties such as the compressibility and heat capacity at the critical point. Moreover, because the correlation length near  $T_c$  is so much greater than interparticle distances, the nonanalytic thermodynamic behavior near  $T_c$  does not depend on the details of short-range intermolecular interactions. Instead, systems in the same "universality class" behave similarly. These classes are enumerated only by spatial dimension and the tensorial nature of the "order parameter". For example, a fluid such as water, with density as its order parameter, is in the same universality class as a uniaxial ferromagnetic solid, which has magnetization as its order parameter. This is because both order parameters are scalar and both are three-dimensional systems.

Although our understanding of thermodynamics near the critical point is not entirely complete, the agreement between experiment and theory is in general very good, about 2% for the exponent  $\nu$ , for example. Improving the understanding of a transport property near the critical point is the primary motivation for the Critical Viscosity Experiment.

The ideas of modern critical thermodynamics (static properties) are important for the Critical Viscosity Experiment in two ways. First, it is the divergence of the fluid compressibility near  $T_c$  which leads to the difficulties associated with gravity. Second, dynamic generalizations of the static theories are used to describe the viscosity of near-critical fluids, as sketched in the next section.

#### B. Viscosity near the critical point

Dynamic fluid properties (thermal conductivity, viscosity, diffusion, etc.) are understood less than static properties because the associated theory and experiments are more difficult. Universality classes, defined by the number of spatial dimensions and the tensorial nature of the order parameter, must be further subdivided according to which conservation laws are pertinent to the system dynamics [16]. Thus a uniaxial ferromagnet and a fluid which belong to the same static universality class might belong to different dynamic universality classes because the dynamics of diffusing spins and particles are quite different [16].

Transport properties typically exhibit divergences near  $T_c$  which can be either "strong" (large divergence exponent) or "weak" (small exponent). Our interest is in the weak enhancement of viscosity near the critical point. Fig. 2.2 illustrates the viscosity increases seen in 1-g measurements [5]. However, viscosity increases of only 10–20% are observed in pure fluids on earth [17]. Experiments on liquid mixtures and the dynamic renormalization group theory [17] suggest that the enhancement is asymptotically a divergence:

$$\eta \sim (T-T_c)^{-\gamma} \quad (4)$$

or, in terms of the correlation length and using Eq.(2),

$$\eta = \eta_0 (Q\xi)^x \eta \quad (5)$$

$$= [\eta_0 (Q\xi_0)^x \eta] \epsilon^{-\nu x} \eta \quad (6)$$

$$= [\eta_0 (Q\xi_0)^x \eta] \epsilon^{-y} \quad (7)$$

The quantity in brackets in Eq.(7) is the divergence amplitude and includes the noncritical viscosity  $\eta_0$ , a characteristic wavevector  $Q$ , and the correlation length amplitude  $\xi_0$ , all of which are fluid-dependent. The divergence is characterized by the exponent

$$y = \nu x_\eta, \quad (8)$$

which is small: about 0.04 according to experiment [5,12,18].

Eqs.(5-7) are a fusion of two theoretical schemes, the mode-coupling scheme and the dynamic renormalization group results. The mode-coupling approach employs the idea that nonlinear couplings between relevant hydrodynamic modes (thermal diffusion and transverse momentum diffusion for a pure fluid) can affect the values of the kinetic coefficients and thus the transport coefficients. Approximately, one has two coupled integral equations [16] which relate wave-vector dependent thermal conductivity  $\lambda(k)$  to the wave-vector dependent viscosity  $\eta(k)$ :

$$\lambda(k) = \lambda_0 + g_0^2 k^{-2} \int \frac{d^3 p}{(2\pi)^3} \chi(p_+) \frac{(k \cdot \tau_p \cdot k)}{\eta(p_-) p_-^2 + \lambda(p_+) \chi^{-1}(p_+) p_+^2} \quad (9)$$

$$\eta(k) = \eta_0 + g_0^2 k^{-2} \int \frac{d^3 p}{(2\pi)^3} \chi(p_-) \frac{[\chi^{-1}(p_+) - \chi^{-1}(p_-)] (p \cdot \tau_k \cdot p)}{\lambda(p_+) \chi^{-1}(p_+) p_+^2 + \lambda(p_-) \chi^{-1}(p_-) p_-^2} \quad (10)$$

Here

$$\tau_k^{\alpha\beta} \equiv \delta_{\alpha\beta} - k_\alpha k_\beta / k^2 \quad (11)$$

is a projection operator which selects for vectors transverse to  $k$  and

$$p_\pm \equiv p \pm k \quad (12)$$

$$g_0 \equiv (\rho k_B T_c)^{-1/2}. \quad (13)$$

The "background" or noncritical thermal conductivity and viscosity are  $\lambda_0$  and  $\eta_0$  respectively. Boltzmann's constant is  $k_B$  and the fluid density is  $\rho$ . Eqs.(9) and (10) relate thermal conductivity and viscosity at wavevector  $k$  to each other through the  $k$ -dependent susceptibility (compressibility)  $\chi(p)$ .

Further approximations lead to the prediction of a logarithmically diverging viscosity,

$$\eta = \eta_0 [1 + x_\eta \ln(\xi)] . \quad (14)$$

However this form is inconsistent with the dynamic renormalization group result that, if  $\eta_0$  can be neglected, the viscosity diverges as a power of the correlation length:

$$\eta \sim \xi^x \eta . \quad (15)$$

Ohta [19] pointed out that, if Eq.(14) is viewed as the first term of a power law expansion, consistency can be restored. The result is Eq.(5). Its form is useful because it specifies how to treat the noncritical background viscosity  $\eta_0$ . For all fluids, and especially binary liquid mixtures, the temperature dependence of  $\eta_0(T)$  cannot be ignored in the analysis of experimental data (see Fig. 2.3). One can either attempt an extrapolation of  $\eta_0(T)$  from the noncritical region into the critical region or fit the experimental viscosity to a product of a simple analytic function and a divergent term. We found the latter approach successful in describing our viscosity data for four binary liquid mixtures [3]. With only three free parameters, it allowed a description of the data over four decades in reduced temperature and yielded consistent values for the viscosity exponent  $y$ .

In contrast, for our measurements on the pure fluids carbon dioxide and xenon [4], we found the use of a "crossover function" necessary for matching the purely noncritical noncritical viscosity  $\eta_0(T)$  to the asymptotic form of Eq.(7). Although crossover required an additional free parameter in the fits and the viscosity increase was limited by gravity, the pure fluids had the advantage of a weak background viscosity temperature dependence easily separated from the critical point divergence.

### C. Fluctuation relaxation time

A key feature of near-critical dynamics is the slow relaxation of fluctuations, which can be characterized by a relaxation time  $\tau$  diverging as

$$\tau \cong \tau_0 \epsilon^{-(3\nu+y)} \cong \tau_0 \epsilon^{-1.93} . \quad (16)$$

The time  $\tau$  is that required for a fluctuation region of size  $\xi$  to return to equilibrium and is an intrinsic property of the fluid. For xenon, the relaxation time amplitude is

$$\tau_0 \cong \frac{6\pi\xi_0^3\eta_0}{1.03 k_B T_c} \cong 1.7 \times 10^{-12} \text{ s} . \quad (17)$$

Far from  $T_c$  the fluctuation relaxation time is of the order of nanoseconds and is of no consequence for a viscosity measurement. In contrast, at the reduced temperature of  $1 \times 10^{-6}$ , the relaxation time  $\tau$  is almost one second, and this constrains both the frequency and shear rate of a viscosity measurement. Otherwise, the fluid will exhibit viscoelasticity at frequencies  $\omega$  such that  $\omega\tau \gg 1$  and reduced viscosity at shear rates  $S$  such that  $S\tau \gg 1$ . Both the viscoelastic [20,21] and shear [22] effects have been modeled, allowing appropriate viscometer design. We verified the viscoelastic effect in two binary liquids [3].

### D. Previous work

The theory of dynamic critical phenomena were reviewed in 1977 by Hohenberg and

Halperin [16]. References 23 and 24 are earlier reviews and the most recent reviews are by Sengers [17] and Nieuwoudt and Sengers [18].

Our previous measurements near the critical points of carbon dioxide and xenon [4] used our old high- $Q$  torsion oscillator viscometer (Fig. 2.4) and took careful account of stratification. The resulting exponents fell into the range  $y=0.041\pm0.001$ . There have been few other pure fluid viscosity measurements made on the critical isochore near  $T_c$ . These include measurements on xenon and ethane by Strumpf, Collings, and Pings [25], on  $\text{CO}_2$

by Bruschi and Torzo [26], and on  $^3\text{He}$  and  $^4\text{He}$  by Agosta et al. [27]. The results from these groups fell into the range of  $0.031 < y < 0.038$ .

Previous measurements of  $y$  for binary liquids have also varied widely. Values from 0.032 to 0.042 were listed in the review of Ref. 17, for example. Although much of this variation has been later eliminated by corrections to the data [18,28], our measurements on four mixtures [3] were the only ones not requiring shear corrections close to  $T_c$ . Our

viscosity exponents from both binary liquids and pure fluids fell into the range  $0.040 < y < 0.044$ , evidence that both types of fluids are in the same universality class.

The agreement among our experimental values of  $y$ , as displayed in Fig. 2.5, is remarkable given the varied experimental problems one encounters in determining  $y$  for this wide range of fluid systems. Nevertheless, these results depend on the multiplicative hypothesis and, in the case of the pure fluids, the correctness of the theories of stratification and crossover.

#### E. Objectives of the flight experiment and the connection to Zeno

In common with all scientific measurements, the Critical Viscosity Experiment will test existing theory as well as look for unanticipated features of nature. We expect the general result to be a small divergence of the viscosity near the critical temperature  $T_c$  superimposed on a slowly varying background viscosity temperature dependence.

Current theories of the critical viscosity divergence make three predictions which the Critical Viscosity Experiment will address. The first is the value of the exponent characterizing the divergence. Recent work by Hao and Ferrell [29] obtained the value

$$y = \nu x_\eta \simeq 0.040 \quad (18)$$

(assuming the exponent  $\eta=0.04$ ), superseding earlier calculations [16,30–33].

The second is the form of the crossover function mentioned above. Work by Olchowy and Sengers [34] improved the consistency of the descriptions of thermal diffusivity and viscosity, but is equivalent to the simpler form of Bhattacharjee et al. [35] for viscosity alone.

The third prediction is the integral equation pair, Eqs.(9) and (10), which connects the critical viscosity to the critical thermal conductivity. A similar pair of relations can be written for the viscosity and the linewidth of light scattered from a near-critical fluid [36]. Testing this prediction will require results from independent viscosity and light scattering experiments on the same substance and is an objective of combining the results of the Zeno experiment (Critical Fluid Light Scattering) and the Critical Viscosity Experiment.

### 3. JUSTIFICATION FOR A LOW-GRAVITY EXPERIMENT

#### A. Stratification near the critical point

The compressibility  $\chi$  of a pure fluid becomes very large near its critical point (a million-fold increase occurs in our thermostat). This divergence, which goes as

$$\chi \sim (T - T_c)^{-1.24} \quad (1)$$

causes a nearly critical fluid to settle under its own weight in Earth's gravity (see Fig. 3.1). This leads to significant experimental problems which were reviewed by Moldover, et al. [1]. Additional interesting intrinsic effects occur when the density gradient is important over even a correlation length [1,37] but will not be important for the viscosity experiment. Instead, our concern is how the gravity-induced density profile near  $T_c$  obscures the interesting near-critical region. Low gravity greatly reduces this problem of sample inhomogeneity and, thanks to the well-developed theory of static critical phenomena, we can quantitatively estimate this improvement below.

Because an oscillating viscometer (approximately) measures  $(\eta\rho)^{1/2}$ , stratification of the sample density  $\rho$  leads to a change in the oscillator's response via three ways, represented by the terms of the following equation:

$$\frac{\Delta(\eta\rho)^{1/2}}{(\eta\rho)^{1/2}} \approx \frac{1}{2} \left[ \frac{1}{\rho} + \frac{1}{\eta} \frac{\partial \eta}{\partial \rho} + \frac{1}{\eta} \frac{\partial \eta}{\partial \xi} \frac{\partial \xi}{\partial \rho} \right] \Delta\rho. \quad (2)$$

The first and second terms are noncritical fluid effects so that the errors in the sample's top and bottom cancel to first order. The third term is negative for both the top and bottom and does not cancel out.

Reference 1 reviews gravitational effects in critical fluids and gives formulas for quantitative calculation of stratification effects. In particular, for a cell of height  $h$  in a field  $g^*$  ( $g^* \approx 1$  on earth), the reduced temperature  $\epsilon$  at which the viscosity error becomes  $\Delta\eta/\eta$  is given by

$$\epsilon = \left[ \frac{g^* h}{2aH_0} \left[ \frac{(\nu b^2 - 0.16)}{(\Delta\eta/\eta)/x_n} \right]^{1/2} \right]^{1/\beta\delta} \quad (3)$$

where  $\beta$ ,  $\delta$ , and  $\nu$  are static critical exponents,  $x_\eta = \nu$  is the viscosity exponent,

$b^2 = 3/(3-2\beta) = 1.28$ , and  $a$  and  $H_0$  are fluid-dependent quantities. On earth, for xenon in our old 1 mm tall cell, the minimum reduced temperature allowed for  $\Delta\eta/\eta = 0.5\%$  is  $\epsilon = 5 \times 10^{-5}$ . On the Space Shuttle,  $g^* = 10^{-4}$  is a conservative estimate. However, the acceleration vector is not necessarily "vertical". Therefore, as a worst case, the longest oscillator dimension must be used for  $h$ . Setting  $h = 10$  mm, typical of both our and old new viscometers, and  $g^* = 10^{-4}$  then gives a minimum possible reduced temperature of  $\epsilon = 6 \times 10^{-7}$ , almost two decades of improvement.

#### B. Reducing stratification without space flight

Moldover et al. [1] stated three classes of techniques for suppressing gravitational stratification on Earth: measuring the sample in a nonequilibrium state, counteracting gravity with another body force, and measuring only in a thin region near the plane where

$\rho = \rho_c$ . Except for the first, all of the methods below fall into one of these three classes. All are presently unsuitable or infeasible.

### 1. Parabolic trajectories using drop towers, aircraft, or rockets

These facilities provide low gravity for only short periods, the longest being about six minutes for sounding rockets, much less than the hours required for equilibration at even moderate reduced temperatures.

### 2. Rotation of the sample cell

We considered averaging Earth's gravity by slowly rotating the sample cell about a horizontal axis. For example, rotation of a 1 cm radius cell at 0.1 Hz would produce a constant radial acceleration of only  $4 \times 10^{-4} g$  while averaging Earth's gravity over  $2\pi$  during a period of 10 s. Although specific predictions do not exist, the best case would be if the slow relaxation time for the density profile (much greater than 10 s) inhibited the formation of any significant density gradient. In compensation, a vertical temperature gradient would be established, about 2 mK across the diameter of a xenon-filled cell. The result would therefore be an inhomogeneity in temperature instead of density, and the accuracy  $\Delta\eta/\eta$  of the viscosity measurement would be compromised below a reduced temperature of

$$\epsilon \cong \frac{y}{(\Delta\eta/\eta)} \frac{\Delta\epsilon}{\Delta\eta/\eta} \cong \frac{(0.04)(0.002 \text{ K}/290 \text{ K})}{(0.005)} = 6 \times 10^{-5}, \quad (4)$$

comparable to the previous limit on the stratified 1 mm sample.

### 3. Stirring the sample

We considered homogenizing the sample by stirring. However, this leads to three problems. First, before making a viscosity measurement, the stirred fluid must settle for at least one viscous relaxation time ( $\sim 4$  min). Second, if no significant density profile should develop during this interval and during the following viscosity measurement (2–20 min), a compensating temperature gradient will be established in the sample, as pointed out above. Third, we are not aware of an appropriate stirrer of sufficiently low power. The section on equilibration has more details concerning the use of a stirrer.

### 4. Use of a thin viscometer

We considered reducing the height of our old torsion oscillator viscometer sufficiently to go a factor of 10 closer to  $T_c$  without encountering significant stratification errors. According to Eq.(4) above, this would require reducing the 1 mm height down to 0.03 mm, leading to two problems. First, the sample would be effectively "locked" to the walls because the container would be much smaller than the viscous penetration depth. (The necessary low frequencies require penetration depths of 0.05 to 0.1 mm.) Therefore, the viscometer would have little sensitivity. Second, the sample's pressure would inevitably cause bowing out of the viscometer's horizontal walls, changing the container shape in a significant but poorly known manner.

### 5. Use of electric or magnetic fields

In principle, an intense, spatially varying, electric or magnetic field could couple to the fluid's electric or magnetic susceptibility and produce a body force counteracting Earth's gravity. Moldover et al. [1] briefly reviewed this possibility, including possible problems caused by a spatially varying  $T_c$ . If such an arrangement could even be demonstrated, it would place additional constraints on the design of the viscometer.

#### 4. DESCRIPTION AND TESTS OF THE NEW VISCOMETER

##### A. The immersed oscillator as a viscometer

The requirements of low frequency and small amplitude of our old torsion oscillator viscometer greatly exacerbated its sensitivity to vibrations. Our analysis of this problem [38] showed that, to obtain an adequate signal-to-noise ratio on the Shuttle, ambient accelerations in the neighborhood of the resonant frequency would have to be lowered to a level of  $4 \times 10^{-8} \text{ g/Hz}^{1/2}$ . Lacking appropriate vibration isolation for the Space Shuttle's environment, we reviewed the behavior of a damped oscillator in the context of our viscometer's requirements and compared the size scaling of the elastic (coupled to the oscillator's spring), inertial (coupled to the oscillator's mass), and viscous (coupled to the oscillator's geometry) forces. Insensitivity to vibration requires the inertial force to be smaller than viscous force, yet low frequency requires the inertial force to be large compared to the elastic force. The result was a need for an oscillator with a light mass, a large surface area, and a weak spring.

Before we describe the oscillating screen as the practical embodiment of this requirement, we will show in general what is needed to use an oscillator as a viscometer. When driven by a force  $F(t)$ , the equation for a simple harmonic oscillator of mass  $m$ , damping constant  $\nu$ , and spring constant  $k$  is

$$m \frac{d^2 x}{dt^2} + \nu \frac{dx}{dt} + kx = F. \quad (1)$$

(We will use a translation oscillator for this illustration.) If the force is sinusoidal,

$$F(t) = F_0 e^{-i\omega t}, \quad (2)$$

then the oscillator's amplitude will be

$$x(t) = x_0 e^{-i\omega t} e^{-i\beta}. \quad (3)$$

Solving for their ratio, namely the oscillator's frequency response, gives

$$\frac{x_0 e^{-i\beta}}{F_0} = (m\omega_0^2)^{-1} \left[ (1 - \Omega^2) - i \left[ \frac{\nu}{m\omega_0} \right] \Omega \right]^{-1}, \quad (4)$$

where

$$\omega_0 = (k/m)^{1/2} \quad (5)$$

is the resonance frequency without damping, and

$$\Omega \equiv \omega/\omega_0 \quad (6)$$

is the reduced frequency. In principle, if one already knows  $m$  and  $\omega_0$ , a measurement of the frequency response at only one frequency will yield the damping constant  $\nu$  at that frequency. In practice, however, absolute calibration of the ratio of amplitude to force requires a second measurement at a frequency far below  $\omega_0$ , where damping is negligible.

For the immersed oscillator, the damping constant, or viscous impedance factor,  $\nu$  is

a complex function of frequency. For low Reynolds number flow,  $\nu(\omega)$  depends only on the geometry of the oscillator and the fluid's density and viscosity. If one knows this dependence from either theory or calibration, then a measurement of  $\nu(\omega)$ , knowledge of the fluid density, and use of Eq.(4) yield the fluid viscosity.

The miniature screen in our viscometer has the drawbacks of hydrodynamics which are difficult to model and a wire size which is difficult to measure. We therefore intend to rely on calibration as the ultimate arbiter of the true form of  $\nu(\omega)$ . However, we also intend to use hydrodynamic theory both as a check on the correctness of our calibration and to provide the most efficient form for the calibration interpolation function.

### B. General layout

Our viscometer consists of a small piece of nickel "screen" suspended by torsion fibers. Its dimensions were determined by a compromise between low-frequency sensitivity, separation of the torsion and bending modes, and ease of construction. The oscillator is driven by an oscillating electrostatic force and its motion is detected by changes in its capacitance relative to four surrounding stationary electrodes.

The general layout, shown in Fig. 4.1, relies on a commercial spectrum analyzer (Hewlett-Packard 35660A) to create a swept sine wave ("chirp") drive, record its voltage in channel 1, and record the voltage proportional to the screen's position in channel 2. The former voltage is transformed by a "square root" amplifier before reaching the cell. The latter voltage is the output of a 10 kHz lock-in amplifier which detects capacitance changes caused by motion of the oscillating screen.

### C. Sample cell

#### 1. Oscillator and electrodes

We constructed the oscillator from commercially available grid formed by electrodeposition of nickel (Buckbee-Mears electroformed mesh, 30 lines/inch). Although the size of a unit square is accurately  $847 \mu\text{m}$ , the thickness and width of the "wires" depend on details of the deposition parameters and on their location within the  $0.08 \text{ m}^2$  sheet supplied by the manufacturer. We took a piece of mesh adjacent to that used for the oscillator and, using a conventional micrometer, measured its thickness to be about  $14 \mu\text{m}$ . When combined with the piece's weight, we inferred a wire width of  $12 \pm 2 \mu\text{m}$ . However, comparison with a fine wire of known diameter under a microscope gave a width of  $27 \pm 3 \mu\text{m}$ . This discrepancy implies the wire was not rectangular in cross-section.

As shown in Fig. 4.2, the inertial element consists of  $7 \text{ mm} \times 19 \text{ mm}$  rectangle, and the torsion fiber consists of two supporting strands of mesh. The screen was lightly creased along its length to stiffen and flatten it. We then soldered the fibers, under  $0.011 \text{ N}$  tension, to a copper bracket. The base of the bracket was soldered to the middle electrical feedthrough.

The four stationary electrodes consisted of  $10 \text{ mm} \times 11 \text{ mm}$  glass microscope cover slips covered with indium. They were soldered to  $1.0 \text{ mm}$  wires soldered to the other four electrical feedthroughs. The gap between opposing stationary electrodes was  $8 \text{ mm}$  and the equilibrium angle of the screen was adjusted for symmetry by twisting the oscillator until exceeding the elastic limit of the torsion fiber.

#### 2. Container

The container consisted of a brass cylinder of  $19 \text{ mm}$  inner diameter,  $38 \text{ mm}$  outside diameter, and  $36 \text{ mm}$  length, with a stainless steel capillary soldered through the wall. Using gold o-rings, we sealed one end with the brass feedthrough plate and the other end with a  $5 \text{ mm}$  thick sapphire window. See Fig. 4.3.

While pumping on the cell it was twice heated to  $80^\circ \text{C}$ , during which the oscillator's mechanical  $Q$  and resonant frequency  $\omega_0$  were measured. Both the  $Q$  (560) and

$\omega_0$  (11.03 Hz) were stable at room temperature for three days after isolating the cell from the vacuum pump, indicating little outgassing. We also observed the dependence of  $\omega_0$  on orientation, its dependence on the stationary electrodes' DC voltage, and the frequency of the bending mode (54 Hz). Fig. 4.4 shows an example measurement of  $\omega_0$ .

### 3. Filling and installation in the thermostat

After initially flushing with xenon gas, the cell was first filled with dense xenon to a density  $\rho$  greater than the critical density  $\rho_c$  by connecting it to a supply bottle (Matheson "99.999%") through a particle filter and stainless capillary, then immersing it in methanol cooled by dry ice to about  $-30^\circ\text{C}$ . The fluid density was then lowered to near  $\rho_c$  by holding the cell just below  $T_c$  in a water bath, bleeding the cell, then observing the meniscus after shaking. The capillary was then crimped near the cell, the cell was removed from the bath, and the capillary was cut and brazed shut. Two partially cancelling errors (the crimper was prematurely removed and a small leak in the brazed seal went unrepaired for 50 days) caused the final density to be about 1% over  $\rho_c$ .

We buried a 10 kohm thermistor in a hole filled with heat sink compound in the cell's wall and attached a thin film heater to the cell with contact adhesive. The four #30 (0.26 mm) lead wires attached to these devices were heat sunk to the cell body with fiberglass adhesive tape, then fed through 30 cm of thin-walled plastic tubing for organization and strain relief.

The feedthroughs for the four stationary electrodes were connected in pairs, then each pair was attached to a coaxial cable (Alpha 9475). The screen's feedthrough was attached to a third cable and grounded copper foil shielding was placed between neighboring feedthroughs. The three coaxial cables were then clamped to the cell body, wrapped 1.5 turns around the cell diameter, then soldered to miniature connectors (Malco Microdot 142-0000-0002) mounted on a bracket attached to the end of the cell. More fiberglass tape was wrapped around the cell body for mechanical security.

We placed the window end of the cell against the rear spacer nested inside the thermostat's inner shell. The front of the cell was then clamped by three radial PVC brackets bolted to a PVC ring also nested in the inner shell.

We grouped the three cables inside an insulating "string of beads" made of polyethylene foam tubes. This 35 cm assembly and the 30 cm length of tubing holding the four #30 wires were coiled inside the inner shell, then brought to the outside of the inner shell's end cap where the wires and cables were heat sunk with fiberglass tape. Similar arrangements were used to bring the conductors to the outside of the thermostat, where the two thermistor wires were soldered to the ohmmeter's four voltage and current leads and the cables were soldered to BNC connectors held by a bracket attached to the thermostat's outer shell.

### D. Drive and detection electronics

An oscillating electric field forces the screen to move, and this motion is detected by the resulting changes in the interelectrode capacitances. To accomplish this, we used the electronic circuit of Fig. 4.5, which includes a 10 kHz oscillator, a ratio transformer, a lock-in detector, and a spectrum analyzer which records the outputs of the lock-in and the spectrum analyzer's internal source. The source voltage is modified by a custom "square-root" amplifier to drive the screen motion, followed by a low-pass filter to attenuate 10 kHz noise.

Also shown are the cell's electrodes. The low-frequency drive voltages and the 10 kHz carrier voltage for detection of the screen's position share the four stationary electrodes surrounding the screen. Electrodes A and D are at a common potential, as are

electrodes B and C. The screen is connected to the input of the lock-in detector. This electrode configuration has the advantage that, in comparison with the torsion mode of the screen, the undesired bending mode is only weakly excited and detected.

### 1. Differential capacitance bridge

As illustrated by Fig. 4.6, the screen's position determines the capacitance differences  $C_A - C_B$  and  $C_C - C_D$ . Thus, after the ratio transformer has nulled the lock-in amplifier's output of the initially stationary screen, the lock-in's voltage is proportional to the screen's displacement  $x$ . For an ideal symmetric parallel-plate geometry with electrode areas  $A$  and stationary gaps  $x_0$ , the electrode capacitances are

$$C_A = C_C = \frac{\epsilon A}{(x_0 - x)} = \frac{\epsilon A}{x_0(1 - x/x_0)} \equiv C_0(1 - x/x_0)^{-1}, \quad (7)$$

and

$$C_B = C_D = C_0(1 + x/x_0)^{-1}, \quad (8)$$

where,  $\epsilon$  is the dielectric constant of xenon at the critical density and, for the present viscometer,

$$C_0 \equiv \frac{\epsilon A}{x_0} \approx 0.3 \text{ pF}. \quad (9)$$

The capacitance bridge reads the summed difference of

$$\Delta C = (C_A - C_B) + (C_C - C_D) = 4C_0 \left[ (x/x_0) + (x/x_0)^3 + \dots \right]. \quad (10)$$

Compared with a conventional bridge, the differential capacitance has the advantages of stability (no external reference) and linearity (the second-order term cancels in Eq.(10)). In practice, accidental asymmetries of the electrode placement and their finite aspect ratio give a small second-order term as well. However, this turns out to be negligible because the ratio  $x/x_0$  does not exceed 0.01 in normal operation.

### 2. Electrostatic drive

The electrostatic force applied to the screen can be estimated by again assuming an ideal parallel-plate geometry. If electrode A has a voltage  $V_0 + \Delta V$  relative to the screen, the screen feels a force

$$F_A = \frac{C_0(V_0 + \Delta V)^2}{2x_0} (1 - x/x_0)^{-2}, \quad (11)$$

and adding this to the opposing force exerted by electrode B with voltage  $V - \Delta V$  gives, to first order,

$$F_A - F_B \approx \frac{2C_0 V_0^2}{x_0} \left[ -\frac{\Delta V}{V_0} + \frac{x}{x_0} \right]. \quad (12)$$

Through cancellation of terms as before, the opposing electrodes help linearize the total

force with respect to the varied voltage  $\Delta V$ . However, note that the second term represents a negative spring constant.

In other contexts, electrostatic drives typically use a small sinusoidal voltage  $\Delta V$  added to a large DC bias  $V_0$  to avoid problems of nonlinearity in the drive force. However, we avoided the use of a large DC bias because it would contribute to nonlinearities not included in Eq.(12) above and because of the danger of pulling the screen to one of the electrodes. Instead we used voltages whose squares include an accurate sine waves, namely

$$V_A = V_0[1 + f_V \sin(\omega t)]^{1/2} \quad (13)$$

Although Eq.(12) above is insensitive to the sign of the DC voltage  $V_0$ , harmonic generation was minimized when  $V_0$  on electrode A was opposite that on electrode B. We believe this is due to the effect of fringing fields, unaccounted for in Eq.(12). Thus the voltage on electrode B was

$$V_B = -V_0[1 - f_V \sin(\omega t)]^{1/2} \quad (14)$$

Fig. 4.7a shows the electrode voltage waveforms used to obtain pure 1 Hz motion of the screen.

### 3. Separation of the drive and detection voltages

The electrostatic force on the screen comes from adding 20–40 V low-frequency voltages to the 1 V, 10 kHz voltage already present on the electrodes used for position detection. The choices for the various component values in Fig. 1 were made so that the drive and detection systems would not interfere with each other. Fig. 4.8 is a simplified circuit for illustrating the competition of several requirements. First, the isolating capacitor  $C_2$  must not significantly attenuate the bridge voltage at frequency  $\omega_2 = 10$  kHz; this requires  $C_2 \gg C_0$ . However, in order to prevent the combination  $R_1 C_2$  from attenuating the drive voltage at frequency  $\omega_1 = 10$  Hz,  $C_2$  is also limited by  $R_1 C_2 \omega_1 \ll 1$ . The resistor  $R_1$  must also be sufficiently large to prevent attenuation of the the bridge voltage, namely  $R_1 C_2 \omega_2 \gg 1$  and  $R_1 C_{\text{cable}} \omega_2 \gg 1$ . Finally, the screen must be effectively grounded at low frequencies without unduly attenuating the bridge voltage at 10 kHz, leading to  $R_0 C_0 \omega_1 \ll 1 \ll R_0 C_{\text{cable}} \omega_2$ . To summarize, the choices for  $C_2$  and  $R_1$  were limited by

$$\frac{\omega_2}{\omega_1} C_2 \gg \frac{1}{\omega_1 R_1} \gg C_2 \gg C_0, \quad (15)$$

and the choice of  $R_0$  was limited by

$$\frac{1}{\omega_1 C_0} \gg R_0 \gg \frac{1}{\omega_2 C_{\text{cable}}}. \quad (16)$$

The capacitance  $C_{\text{cable}}$  was minimized by the use of low-capacitance cable. Nevertheless, at 300 pF, it attenuated the 10 kHz signal by a factor of about 1000.

#### 4. Tests of the drive and detection system

Fig. 4.9a shows the magnitude and phase of the oscillator's frequency response operated under nominal conditions. We tested the total drive and detection system for linearity in two ways. First, we increased the AC drive amplitude ( $f_V$  of Eqs.(13) and (14)) from the nominal level by a factor of 1.4, the maximum allowed for a DC level of  $V_0=30$  V, and found no effect on the magnitude of the frequency response except for a 0.9% decrease in the region near 3 Hz. Decreasing the drive level from nominal by a factor of 2.0 caused a corresponding decrease of 0.4%. The frequency region affected is also where the screen's velocity is highest, suggesting that this small nonlinearity is a hydrodynamic effect.

Second, we measured harmonics present in the screen's motion when the drive input was a pure sine wave. At the nominal drive amplitude, and below 10 Hz, harmonic distortion was less than 0.4%, provided that the DC voltages  $V_0$  were opposite for

electrodes A and B. (We also obtained low harmonic distortion with DC voltages of the same sign when, as suggested by calculation, we used a static magnetic field to adjust the equilibrium position of the screen about 10%. This latter method is unnecessary.)

We compared the electrostatic drive scheme against the magnetic drive scheme used in an earlier version of the viscometer (an external oscillating field couples to the screen's permanent magnetic moment). When driven to the same amplitudes, the magnitude of the ratio of frequency responses obtained by the two methods for the same screen amplitude was constant from 1 to 12 Hz, but deviated by as much as 4% at lower frequencies. This deviation was roughly proportional to the screen amplitude, suggesting a low-frequency nonlinear mechanism. As this nonlinearity was not present in the electrostatic drive, we concluded the deviation was due to the magnetic drive. The phase differences between the frequency responses obtained by the two drive methods were  $0^\circ \pm 1^\circ$ .

We estimated the signal-to-noise ratio by comparing successive measurements of the frequency response. Fig. 4.9b shows the magnitude of the ratio of two successive frequency response measurements.

#### D. Thermostat design and operation

##### 1. Thermostat construction

Our thermostat, consisting of three cylindrical shells, is similar to those used by others for careful temperature control near the critical point. To guarantee small temperature gradients at the sample cell we used thick shells with poor coupling to each other. Although this causes slow response times, on the order of an hour, because the response time of the sample itself is much longer over most of the temperature region of interest, this is not a significant drawback. In exchange, the thermostat is easily made mechanically robust, is easily modeled, and is insensitive to errors of design and construction.

Fig. 4.10 shows the nested arrangement of the three thermostat shells, made of 6.4 mm thick anodized aluminum, and the sample cell, made of brass. (The flight cell is to be made of copper.) Separating the shells are toroidal spacers machined from 6.4 mm thick, glass-filled polycarbonate sheet (see Fig. 4.11). Notches in each shell's end plates and in the spacers allow the passage of wires. We glued thin film heaters onto each shell and buried a control thermistor in the shell under one heater some 20 mm from the end of the shell. The wires necessary for measurement and control of the four thermistors and four heaters and the cables to the viscometer cell are indicated by Fig. 4.12. To ease installation of the sample cell, its associated wiring was brought out the right side; all other wiring was brought out the left side. The 38 mm gaps between the ends of the shells allowed easy placement of the wire loops necessary for thermal isolation.

For connections to the heaters and thermistors, we used #30 (0.26 mm dia) copper wire. To reduce the wiring complexity only two wires were connected from each thermistor

to the electrical connector mounted on the outside of the outer shell. The additional resistance is equivalent to a constant negligible offset of 1.4 mK. Changes in the thermostat of 1 K caused changes in this offset of 5  $\mu$ K, again negligible. For the viscometer signal we used small diameter coaxial cable (Alpha 9475) whose main thermal conductance consisted of a central #30 wire and a #30 drain wire.

At the cell and at each shell, the wires and cables were taped down for thermal grounding. The wires running between shells were organized by a single length of PTFE spaghetti. Taping the spaghetti ends at each shell provided strain relief (See Fig. 4.13). The three coaxial cables were fed through a series of polyethylene foam tubes. This organized the cables and prevented thermal short circuits in the loop of cable between shells. The ends of the middle and outer shells were lined with a 3 mm thick ring of foam insulation as an additional precaution. The total thermal conductivity of the wires and cables was less than 2% of the total conductivity between shells.

All of the #30 wires were connected to two RS-232 connectors mounted on the outside of the outer shell. A 3 mm foam blanket was wrapped around the outer shell and the shell placed on a foam cradle inside a commercial ("1.7 cu ft") refrigerator.

## 2. Calculated gradients

In equilibrium, the temperature gradient on any thermostat component has two causes: that imposed by a temperature gradient on the surrounding shell and that generated by a local power source. Calculating the thermostat's temperature distribution to 10% accuracy would require a two-dimensional finite-element model. Instead, we made analytic estimates to place bounds on the gradients accurate to about a factor of two.

First consider Fig. 4.14a, where a gradient is imposed on shell number 2 by the surrounding shell number 1, in the limit where all of the significant heat flow occurs at the sides and not at the ends. (This is the case for the present thermostat; see Table 1). The heat flow equation is

$$[\lambda_{Al} A_2] \left[ \frac{d^2 T_2(x)}{dx^2} \right] = \left[ \frac{2\pi \lambda_{air}}{\ln(R_1/R_2)} \right] [T_2(x) - T_1(x)], \quad (17)$$

where  $\lambda_{Al}$  and  $\lambda_{air}$  are the thermal conductivities of aluminum and air and  $A_2$  is the cross section area of shell 2. If the temperature distribution on the outer shell is linear, namely

$$T_1(x) \equiv T_0 + ax, \quad (18)$$

then the temperature distribution on the inner shell will be

$$T_2(x) = T_0 + a \left[ x - \frac{d \sinh(x/d)}{\cosh(x_2/d)} \right]. \quad (19)$$

The characteristic length  $d$ , defined by

$$d \equiv \left[ \frac{A_2 \lambda_{Al} \ln(R_1/R_2)}{2\pi \lambda_{air}} \right]^{1/2}, \quad (20)$$

is the length over which air conduction between shells dominates metal conduction along the shell. For the present thermostat, the length  $d$  is about 1 m for each component, much greater than the lengths of the shells (Table 1). This allows a further approximation in estimating the gradient reduction ratio. For example, this ratio for the thermostat's inner

shell is

$$\frac{\left[\frac{dT_2}{dx}\right]}{a} x_2 \cong \frac{1}{2} \left[\frac{x_2}{d}\right]^2 = 4 \times 10^{-4} \quad (21)$$

If radial conduction is ignored and only heat flow at the ends of the cylinders is considered, then the gradient reduction ratio is approximately

$$\frac{\left[\frac{dT_2}{dx}\right]}{a} \cong \left[\frac{x_2}{x_1}\right] \left[ \frac{\lambda_{air}}{\lambda_{Al}} - \frac{\pi R_2^2}{A_2} \right] = 6 \times 10^{-4}, \quad (22)$$

where the thermostat's inner shell was again used as an example.

The gradient reduction ratios calculated above are not achieved in practice for several reasons, for example the effects of radiation and spacers. The most important cause is power dissipated directly on the shell. Consider the case of Fig. 4.14b, where a heater of power  $P$  is placed at the right end of shell 2. For the case where heat flows only through the ends, the resulting gradient is

$$\frac{dT_2}{dx} \cong \frac{P}{A_2 \lambda_{Al}}. \quad (23)$$

The power  $P$  raises the average temperature of shell 2 by the amount  $T_2 - T_1$ . Relating the gradient to this temperature difference, and assuming only air conduction, gives

$$\frac{dT_2}{dx} \cong \frac{\pi R_2^2}{A_2} \frac{\lambda_{air}}{\lambda_{Al}} \frac{T_2 - T_1}{x_1} = (0.005 \text{ m}^{-1})(T_2 - T_1), \quad (24)$$

where the inner shell was used as an example.

For the more realistic case where radial conduction dominates over end conduction, the temperature gradient is

$$\frac{dT_2}{dx} \cong \left[\frac{x_2}{d}\right]^2 \frac{T_2 - T_1}{x_2} = (0.10 \text{ m}^{-1})(T_2 - T_1), \quad (25)$$

a factor of 20 greater for the example of the inner shell. If the heater is split into a heater at each end, each dissipating  $P/2$ , the estimate of Eq.(25) is reduced by only a factor of four.

### 3. Thermostat characteristics

Table 1 lists, in SI units, various properties of the cell and shells, referenced to Fig. 4.14a. The quantities  $\kappa_{side}$  and  $\kappa_{end}$  are the air conductivities between shells for the cylinder sides and end caps. The quantities  $\kappa_{sp}$  and  $\kappa_{rad}$  are the conductivities of the plastic spacers and that contributed by radiation (where we assumed  $T=290$  K and an emissivity of 0.3). The total conduction  $\kappa$  and heat capacity  $C$  then give the relaxation time  $\tau_{ext}$  for relaxation to the temperature of the surrounding shell. The shell's internal

relaxation time (for equilibration between the left and right ends) is  $\tau_{\text{int}}$ .

The cell's characteristics are the most important. Although there are uncertainties in  $\kappa_{\text{sp}}$  (due to complicated geometry) and  $\kappa_{\text{rad}}$  (due to emissivity), the measured relaxation time  $\tau_{\text{ext}}$  for the cell agreed within 7% with the estimate of Table 1. Note that the cell's spacer conductivity  $\kappa_{\text{sp}}$  is almost half of the total conductivity  $\kappa$ .

Table 1: Calculated thermostat characteristics

Shell	$R_2/m$	$R_1/m$	$x_2/m$	$x_1/m$	$d/m$
1 (out)	0.076	0.1 ?	0.159	0.1 ?	1.15
2 (mid)	0.057	0.070	0.114	0.038	0.85
3 (in)	0.038	0.051	0.070	0.038	0.82
4 (cell)	0.019	0.032	0.030	0.030	0.74

Shell	$\kappa_{\text{side}}$	$\kappa_{\text{end}}$	$\kappa_{\text{sp}}$	$\kappa_{\text{rad}}$
1 (out)	0.167	0.008	0.059	0.312
2 (mid)	0.160	0.012	0.078	0.169
3 (in)	0.069	0.005	0.026	0.071
4 (cell)	0.017	0.001	0.031	0.016

Shell	$\kappa/(W/K)$	$C/(J/K)$	$\tau_{\text{int}}/s$	$\tau_{\text{ext}}/s$
1 (out)	0.546	2747	105	5031
2 (mid)	0.419	1455	54	3473
3 (in)	0.171	576	20	3368
4 (cell)	0.065	159	3	2446

#### 4. Temperature control

The temperature of each shell was controlled through a digitally computed feedback loop. We used a commercial temperature controller (Quantum Design 1802) with four inputs to measure the temperature of the three shells and surrounding air. Its two output channels were used to control the temperatures of the inner and middle shells. The outer shell's temperature was controlled through a digitally programmed power supply. To minimize gradients, we did not control the cell's temperature. Its temperature was measured with a commercial digital ohmmeter (Hewlett-Packard 3458A).

The commercial controller was limited to a single-bit resolution of 0.5 mK. This was adequate for all but the slowest sweeps where, as Fig. 4.15 indicates, the time between bit changes was longer than the cell's (metallic) relaxation time. The commercial ohmmeter, adequate for the 1-g measurement, cannot be used for the flight experiment because its 2 ppm stability is equivalent to  $\pm 0.3$  mK. Also, although the power dissipated in the thermistor is only  $6 \mu\text{W}$  when averaged over the 10 s cycle time currently used, there may be a significant gradient created near the thermistor as the heat from each current pulse dissipates.

For temperatures below  $25^\circ\text{C}$ , we modified the commercial refrigerator to bring electrical cables inside. With the air stirred by a small fan and the operation of a 30 W heater attached to evaporator, the air temperature was typically  $5^\circ\text{C}$ . The typical offsets between the outer shell and the refrigerator's air was thus about 12 K. We also maintained 0.3 K between the middle and outer shells and 0.03 K between the inner and middle shells. The thermistors mounted on the shells were calibrated against the cell's thermistor to obtain accurate offsets between shells.

### 5. Thermostat programming

The temperature program typically started at least 3 K above  $T_c$  for sample equilibration, then ramped the temperature linearly down toward  $T_c$ , making step changes in the rate as  $T_c$  was approached. For example, when the reduced temperature has changed by a factor of 10, the ramp rate was reduced by a factor of 10. The ramp rate was left unchanged for the final few mK during the crossing of  $T_c$ . Fig. 4.16 shows an example of part of a temperature history.

### F. Low-level vibration tests

We used a similarly constructed viscometer in a series of tests which quantified the viscometer's sensitivity to vibration. Combination of this information with data on the Shuttle's vibration environment allows us to predict the effect of the orbiting Shuttle's "g-jitter" on the viscometer's signal-to-noise ratio.

We first attached the viscometer, an accelerometer, and a shaker to a bracket resting on rollers. This us allowed to measure effects due to translation vibrations in three orthogonal directions. Then we used a bracket mounted on a horizontal bearing to measure effects due to rotation vibration around three orthogonal axes. We obtained acceleration frequency response data, essentially the ratio of screen motion divided by the applied acceleration. We also measured the signal-to-noise ratio of a normal frequency response measurement when degraded by vibrations.

As expected, the most sensitive mode was rotation about the screen's torsion axis. The next most sensitive mode was translation along the long axis of the screen. Although unexpected, this response was consistent with a model which took asymmetry into account (the angle between the screen's left and right arms was less than  $180^\circ$ ).

Also as expected, the signal-to-noise ratio of the vibration-perturbed frequency response improved as  $N^{1/2}$ , where  $N$  was the number of frequency responses averaged by the spectrum analyzer.

We found agreement between the signal-to-noise level of the vibration-perturbed frequency response and the prediction based on the ratio of the oscillator's response to acceleration and its response to the oscillator's drive. (Magnetic drive was used for this study.) With this verification of our understanding of the oscillator's behavior, we can specify a limit on the allowed vibration levels, denoted  $g/\text{Hz}^{1/2}$ .

$$\left[ g/\text{Hz}^{1/2} \right] = \left[ \frac{\Delta\eta}{2\eta} \right] \left[ \frac{\text{drive response } V/V}{\text{vibration response } V/g} \right] \left[ N^{1/2} \right] \left[ \text{drive } V/\text{Hz}^{1/2} \right] \quad (26)$$

The allowed vibration level can be increased either by increasing the number of measurements  $N$  or by increasing the drive level. The latter is limited by the amplitude effects discussed in the section on requirements and by the nonlinearity effects discussed in the section on drive and detection.

The precision  $(\Delta\eta/\eta)$  used in Eq.(26) refers to the signal-to-noise ratio at a single frequency within the spectrum analyzer's frequency window. Our particular analyzer obtained a frequency resolution of  $1/400$  of the measured 12.5 Hz interval by requiring a single measurement to last 32 s. Because the frequency response varies slowly with frequency, one can immediately improve the limit above by averaging the frequency response over several adjacent bins. For example, averaging over a 0.5 Hz interval improves the limit of Eq.(26) by factor of

$$\left[ \frac{0.5 \text{ Hz}}{12.5 \text{ Hz}} (400) \right]^{1/2} = 4. \quad (27)$$

### G. Hydrodynamic models

Extraction of the viscosity from the oscillator's frequency response requires knowledge of the viscous impedance factor  $\nu(\omega)$  from either theory or calibration. No theory exists for the ideal geometry most similar to our screen, namely a grid of squares of length  $b$  formed by "wires" of roughly rectangular cross-section. However, a sufficiently accurate approximation should be possible for three reasons. First, the unit square of size  $b$  is at least 10 times greater than the viscous penetration length  $\delta$ , so that  $\nu(\omega)$  is only weakly dependent on the grid size  $b$ . Second, the expected variation of the viscosity in the flight experiment will be weak, probably less than 40%. Third, the viscous penetration diameter is at least four times the width of the screen's "wires". Thus  $\nu(\omega)$  should be only moderately sensitive to the exact shape of the wire's cross-section.

We were provided with two very different candidate models for  $\nu(\omega)$ . They and numerical simulation work by Chait are summarized below. Although the models give a remarkably good description of the viscometer's frequency response function at any one temperature, the temperature dependence of our data is not understood. Thus, explicit calibration of the viscometer using one of the models as an interpolating function will be required.

#### 1. Oscillating cylinder model

Using modern notation, Dill [39] reviewed the literature related to the problem of a transversely oscillating cylinder, first solved by Stokes. Consider a grid formed of wires of cylindrical cross-section with radius  $R$ . In the limit where the length  $b$  of a unit square is much longer than any other length, the viscous impedance factor for a unit square is

$$\nu(\omega) = 2\pi R^2 b \rho \omega (k' - ik), \quad (28)$$

where the functions  $k$  and  $k'$  can be expressed in terms of Kelvin functions. The functions  $k$  and  $k'$  depend on the parameter

$$M = 2^{-1/2} \frac{R}{\delta}, \quad (29)$$

proportional to the ratio of the radius  $R$  to the viscous penetration length,

$$\delta \equiv \left[ \frac{2\eta}{\rho\omega} \right]^{1/2}. \quad (30)$$

#### 2. Oscillating grid model

The second analytic model assumes that the screen can be modeled as an infinite grid of infinitesimally thin wires. Davis [40] used periodic point force singularities to describe the flow field through the oscillating grid. His final result for the viscous impedance factor of a unit square is

$$\nu(\omega) = 8\pi \eta b A_0, \quad (31)$$

where  $b$  is the length of a unit square and the complex parameter and the complex number  $A_0$  was obtained from the solution of a system of linear equations. The quantity  $A_0$  depends on the parameters  $\epsilon$  and  $\Delta$ , where

$$\epsilon \equiv -\frac{2x_1}{b} 1 - \quad (32)$$

is the ratio of the wires half-width  $x_1$  to the grid length  $b$  and  $\Delta$  is defined by the ratio of the two lengths, the grid length  $b$  and the viscous penetration length  $\delta$ , namely

$$\Delta \equiv \frac{1}{2} \left[ \frac{b}{\pi \delta} \right]^2. \quad (33)$$

### 3. Numerical simulation

Chait [41] has modeled the oscillating screen by incorporating a moving coordinate grid into the package FIDAP for incompressible fluid dynamics. His two-dimensional simulations modeled the oscillations of a wire of rectangular cross-section at various frequencies and choices of wire widths and thicknesses. At amplitudes similar to our nominal conditions, Chait found the nonlinear term of the Navier-Stokes equation contributes 0.27% to the magnitude of  $\nu$  at 5 Hz.

### 4. Torsional vs. translational oscillator

Although our modeling assumes a translation oscillator, our viscometer is of course a torsion oscillator. However, in the limit where the screen's area is divided into infinitely many small squares and the angular amplitude is infinitesimally small, the translation model is exact. The equation of motion for a torsion oscillator with moment of inertia  $I$ , viscous torque  $\nu_\theta(d\theta/dt)$ , and torsion spring constant  $k_\theta$  driven by a torque  $\tau_{\text{drive}}$ , is

$$I \frac{d^2 \theta}{dt^2} + \nu_\theta \frac{d\theta}{dt} + k_\theta \theta = \tau_{\text{drive}} \quad (34)$$

By denoting the screen's total mass, length, and width as respectively  $M$ ,  $2R$ , and  $W$  the moment of inertia  $I$  can be rewritten in terms of the mass  $m$  and size  $b$  of a single square according to

$$I = \frac{1}{3} MR^2 = \frac{1}{3} \left[ \frac{2RW}{b^2} \right] mR^2 = \left[ \frac{2R^3W}{3b^2} \right] m \equiv Km. \quad (35)$$

The viscous torque can be rewritten as

$$\nu_\theta \frac{d\theta}{dt} = 2W \int_0^R \nu' \frac{dx}{dt} r dr, \quad (36)$$

where the viscous impedance per unit area  $\nu'$  is defined in terms of the viscous impedance  $\nu$  per square of side  $b$ :

$$\nu' \equiv \frac{\nu}{b^2}. \quad (37)$$

The viscous torque can then be rewritten as

$$\nu_\theta \frac{d\theta}{dt} = 2W \int_0^R \frac{\nu}{b^2} r^2 \frac{d\theta}{dt} dr = K \frac{d\theta}{dt}. \quad (38)$$

Use of Eqs.(35) and (38) then allows Eq.(34) to be rewritten in the same form as Eq.(1),

$$m \frac{d^2 \theta}{dt^2} + \nu \frac{d\theta}{dt} + \frac{k}{K} \theta = \frac{\tau_{drive}}{K}, \quad (39)$$

so the analogy holds.

#### 5. Comparisons with frequency response data

We first compared the predictions of the two analytical models to the oscillator's frequency response at one temperature. Fig. 4.17 shows the magnitude and phase of the frequency response obtained at the reduced temperature of  $3.45 \times 10^{-4}$  and also the predicted response of an oscillating cylinder with a diameter of 26.7 micrometers. The two free parameters for the calculated curve are the diameter, which is consistent with that observed under the microscope, and the magnitude of the response at very low frequency, which contains poorly known electronic drive and detection factors. The overall agreement is very good.

Although Davis' oscillating grid model gave a somewhat less accurate description, the wire width  $x_1$  giving the best result was close to the radius  $R$  used for the oscillating cylinder model.

#### 5. Accuracy: Comparisons at different temperatures

We measured the frequency response of the oscillating screen as a function of temperature to characterize the viscometer's precision, reproducibility, and accuracy. Anticipating effects due to stratification of the fluid density close to  $T_c$ , we kept the screen in a vertical plane. Thus, when stratification required us to integrate the fluid's viscosity and density over the height of the screen, the calculation was insensitive to small geometrical imperfections such as bowing of the screen.

Fig. 4.18 shows the results of measurements obtained over the 30 K range above  $T_c$ . In order to minimize data storage and allow two-dimensional plots, we recorded only the ratio of magnitudes,

$$\frac{|\text{frequency response at } 5 \text{ Hz}|}{|\text{frequency response at "0" Hz}|},$$

where the 5 Hz value was obtained by an average over the 16 points between 4.75 and 5.25 Hz and the "0" Hz value was inferred from a linear fit to the 16 points between 0.125 and 0.625 Hz. This normalization cancels the prefactor  $(m\omega_0^2)^{-1}$  of Eq.(4) as well as the imperfectly known factors relating the instrument's detection and drive voltages to the oscillator's displacement and applied force.

The curves of Fig. 4.18 have three main features: From the reduced temperature of  $10^{-1}$  to  $10^{-2}$  the decreasing noncritical viscosity causes the frequency response to increase. From  $10^{-2}$  to  $10^{-4}$  the viscosity again increases, causing the frequency response to decrease. From  $10^{-4}$  to  $10^{-6}$  the viscometer is limited by the effects of gravitational stratification. Above  $10^{-4}$  the data were reproducible independent of temperature history as verified by measurements obtained with (slow) positive, negative, and zero sweep rates. Close to  $T_c$ , the data were reproducible to within 0.3% at sweep rates slower than  $3 \times 10^{-7}$  K/s (including the result of a two-day equilibrium run at 10 mK above  $T_c$ ). However, the time constant inferred from the evolution of the frequency response at any

constant temperature never exceeded 5 hours; presumably stratification reduced this from the value expected from that calculated later in Section 6.

We used two free parameters in drawing the calculated curves of Fig. 4.18, the effective radius of the screen's wire, and the height of the screen's center relative to the plane where  $\rho = \rho_c$ . The former parameter was required by our insufficient knowledge of the wire's cross section shape, and the latter parameter was necessary because of uncertainties in the xenon's density and in the height of the screen's center in the cell. The mass  $m$  and the temperature-dependent resonance frequency in vacuum  $\omega_0(T)$  were fixed by independent measurement.

There are three discrepancies between the calculated curve and our experimental data. The first is a temperature dependence whose origin we do not understand. This can be seen by comparing data on opposite sides of the maximum occurring near  $10^{-2}$ .

The second discrepancy is centered near the reduced temperature of  $10^{-3.3}$ . One possible cause is excitation of the "sloshing" mode of the cell's stratified fluid. At this reduced temperature, the sloshing frequency is approximately

$$f_{\text{slosh}} \approx \frac{1}{2\pi} \left[ \frac{g}{R} - \frac{\Delta\rho}{\rho_c} \right]^{1/2} = 0.5 \text{ Hz}, \quad (40)$$

where  $g$  is the gravitational constant,  $R$  is the cell radius, and  $\Delta\rho$  is a typical stratified density difference. At larger reduced temperatures, the amplitude of this mode is weak in the absence of stratification. At smaller reduced temperatures, the mode is stronger but its frequency falls above the range used for calculation of the "0" Hz value of the frequency response.

The third discrepancy is in the change of the frequency response with viscosity. Although partly masked by the first two discrepancies, the calculated viscosity derivative of the frequency response seems too large by 5–10%. Several pieces of evidence cause us to attribute this discrepancy to lack of a hydrodynamic theory accounting for the screen wire's true cross section. First, the theories of Stokes [39] and Davis [40], which assume cross-sections of a circle and an infinitesimally thin rectangle respectively, differ by a comparable amount (see Fig. 4.19). The numerical simulation of a rectangular cross-section, by Chait [41] gives a lower viscosity derivative than either analytical theory. Although we have not obtained scanning electron micrographs of a representative portion of screen, the factor of two discrepancy between the widths estimated by two different methods (Section 4.C) imply the cross-section is neither rectangular or circular.

Close to  $T_c$ , the two curves representing displacements of 0.0 and 0.9 mm of the screen's center from the plane where  $\rho = \rho_c$  demonstrate the sensitivity of the calculated description to this displacement. The discrepancy near the minimum at  $\epsilon = 10^{-4.3}$  is partially due to our present uncertainty about the viscometer's calibration.

## H. Summary of the viscometer's tests

### 1. Robustness

The characteristics of the present viscometer did not change significantly after undergoing launch vibration tests. A small initial leak went unrepaired in order to facilitate timely completion of the launch vibration tests. After repair, the leak rate was less than 0.03% over a period of three months.

### 2. Precision

The oscillator's signal-to-noise ratio is presently limited by the lock-in amplifier's

preamplifier noise to about  $\pm 0.07\%$ , corresponding to a viscosity sensitivity of about  $\pm 0.1\%$ .

### 3. Vibration sensitivity

The viscometer's sensitivity to vibration is sufficiently low to tolerate typical Shuttle vibrations up to about  $8 \times 10^{-5} \text{ g/Hz}^{1/2}$ .

### 3. Linearity

At the nominal operating amplitude of 14 microns, the viscometer's total nonlinearity, due to all causes, both in the drive or detection schemes and due to nonlinearity of the fluid flow itself, is of the order of 0.5%. The frequency dependence of this nonlinearity (its peak occurs at the frequency of the screen's maximum velocity) and its consistency with Chait's simulation suggest that it is due to the nonlinear term in the Navier-Stokes equation.

### 4. Reproducibility

The viscometer's frequency response has been reproducible to within 0.3% over a period of one month. Provided the temperature sweep rates do not exceed bounds which are consistent with both our equilibration calculations and the typical duration of a Shuttle mission, the viscometer's results are independent of temperature history.

### 5. Accuracy

At fixed temperature, the magnitude and phase of the viscometer's frequency response over the frequency range of 0.1 to 10 Hz are consistent with the hydrodynamics of the transversely oscillating cylinder to within 2%. This validates the general concept of the immersed oscillator as a viscometer and suggests a reliable form for a calibration function. However, an accurate description of the data requires the cylinder's effective radius to be a weak function of viscosity ( $\sim 1\%$  change over the viscosity range covered). Calibration against a fluid unaffected by a nearby critical point will be needed to extract the viscosity from the frequency response with an accuracy of 1%.

There are presently two additional limits on the viscometer. The first is what appears to be the effects of coupling to the sloshing mode in the stratified sample. Although this would not be a problem in the flight experiment, this connection cannot be established without further work. The second is a temperature dependence of unknown origin seen at higher temperatures. Use of the viscometer at temperatures more than 1 K above  $T_c$  would require this effect to be included in the calibration.

## 5. REQUIREMENTS

Although there are literally dozens of techniques for measuring viscosity, we found none suitable for the measurement of the viscosity of a pure fluid near its critical point. This led to the development of our old torsion oscillator viscometer. The additional constraint of insensitivity to vibrations led us to develop the new oscillating screen viscometer, and the following requirements were calculated in this context.

Improvement of an experiment with respect to one particular constraint without regard for other constraints represents unnecessary effort and usually leads to less than an optimum experiment. The quantitative limits stated below were derived with this in mind. For example, temperature control need not be better than the limits imposed by the frequency constraint.

### A. Viscometer

#### 1. Signal-to-noise ratio

To meet our nominal goal of measuring the viscosity exponent  $y$  to an accuracy of  $\Delta y/y = 0.01$ , we assumed the viscosity has approximately power-law dependence between the reduced temperatures  $\epsilon_1$  and  $\epsilon_2$  where

$$\epsilon_1 \equiv \text{onset of crossover to noncritical region} = 2 \times 10^{-4}, \quad (1)$$

$$\epsilon_2 \equiv \text{onset of viscoelasticity caused by 5 Hz} = 2 \times 10^{-6}. \quad (2)$$

The choice of  $\epsilon_1$  is extremely conservative (see Fig. 1.1). The choice of  $\epsilon_2$  is forced by the bandwidth of the oscillator and the knowledge that significant viscoelasticity begins at the reduced temperature  $\epsilon_2$  where [20,21,3]

$$\epsilon_2 = \left[ \frac{5}{\omega \tau_0} \right]^{-1/(3\nu+y)}, \quad (3)$$

where  $\tau_0$  is the amplitude of the fluctuation relaxation time.

The required precision of the viscosity measurements can thus be estimated as

$$\frac{\Delta \eta}{\eta} = y \ln(\epsilon_1/\epsilon_2) \frac{\Delta y}{y} = (0.04)[\ln(100)](0.01) = 0.0018 \cong 0.2\%. \quad (4)$$

This specification, which also gives the viscometer's signal-to-noise ratio, leads to the remaining requirements. Note that, in the asymptotic limit where the multiplicative hypothesis apparently holds, the exponent  $y$  is unchanged if the viscometer accuracy is in error by a constant factor.

#### 2. Temperature stability

Good temperature control means that the sample temperature is both constant in time and homogeneous throughout its volume. The viscosity error  $\Delta \eta$  induced by a temperature error  $\Delta T$  is

$$\frac{\Delta \eta}{\eta} = \frac{1}{\eta} \frac{\partial \eta}{\partial T} \Delta T \quad (5)$$

so that, assuming power-law dependence of viscosity, the allowed error is

$$\Delta T = -\frac{\epsilon T_c}{y} \frac{\Delta \eta}{\eta} . \quad (6)$$

At the closest approach to  $T_c$ , this is

$$\Delta T = -\frac{\epsilon_2 T_c}{y} \frac{\Delta \eta}{\eta} = \frac{(2 \times 10^{-6})(290 \text{ K})}{(0.04)} (0.002) = 29 \text{ } \mu\text{K} . \quad (7)$$

The precision requirement is relaxed far from  $T_c$ . From Eq.(6), the allowed relative error in the reduced temperature is

$$\frac{\Delta \epsilon}{\epsilon} = \frac{1}{y} \frac{\Delta \eta}{\eta} = 0.05 , \quad (8)$$

which is easily met. Absolute temperature accuracy is not crucial since the important parameter is the difference from the critical temperature  $T - T_c$ .

### 3. Sample density

Loading of the sample to its critical density must be done to an accuracy commensurate with the required minimum reduced temperature. To estimate the required loading accuracy, we assumed two-scale universality to plot contours of constant viscosity in  $(T, \rho)$ . At  $\epsilon_2 = 2 \times 10^{-6}$ , the sample density must be within 0.3% of the critical density to avoid viscosity errors greater than 0.2%.

### 4. Oscillator amplitude effects

This section estimates various effects depending on the oscillator's amplitude  $x_0$ .

The following three effects are estimated by using the nominal amplitude of the screen tip, inferred from visual observation to be 14 microns at 5 Hz.

#### 4.1 Shear rate

Excessive shear in the fluid can disrupt fluctuations, leading to a constraint on the oscillator's amplitude  $x_0$ . Our oscillator's shear rate  $S$  is approximately

$$S \approx \frac{\omega x_0}{\delta} \approx \frac{(2\pi \cdot 5 \text{ s}^{-1})(14 \times 10^{-6} \text{ m})}{(63 \times 10^{-6} \text{ m})} = 7 \text{ s}^{-1} , \quad (9)$$

where the viscous penetration length  $\delta$  is defined in terms of the fluid density  $\rho$ , viscosity  $\eta$ , and oscillator frequency  $\omega$ :

$$\delta \equiv (2\eta/\rho\omega)^{1/2} . \quad (10)$$

The reduced temperature where shear begins to degrade the viscosity measurement depends on the fluctuation relaxation time. We estimate this reduced temperature to be

$$\epsilon_{\text{shear}} = \left[ \frac{S\tau_0}{6\pi\lambda} \right]^{1/(3\nu+y)} = 1.4 \times 10^{-6} , \quad (11)$$

where we estimated [3] the value of Oxtoby's [22] parameter  $\lambda$  at 0.13 to correspond to a viscosity error of 0.5%. (A small shear rate effect can be corrected for.)

The low frequency and shear rate of the viscometer also ensure that viscous heating of the sample is negligible: of the order of picowatts.

#### 4.2 Acoustic and compression effects

Conceivably the oscillator could lose power by sound emission as well as by viscous drag. For the example of a sphere of radius  $R$ , oscillating in xenon at 10 Hz, the ratio of the acoustic force  $F_a$  to the real part of the viscous force  $F_\eta$  is

$$\frac{F_a}{F_\eta} = \frac{(2\pi)^3}{9(1 + \delta/R)} \left[ \frac{R^4}{\delta\lambda^3} \right] = 8 \times 10^{-13}, \quad (12)$$

completely negligible.

Although the associated acoustic pressure  $p_a$  is small, the fluid compressibility is very large. By relating to the compression caused by a reduced gravity  $g^*$ , we can place a bound on its effect:

$$g^* \equiv \frac{p_a}{\rho g h} = \frac{(1/2) R \omega^2 x_0}{g h} = 3 \times 10^{-5}, \quad (13)$$

where the frequency  $\omega/2\pi = 10$  Hz and cell height  $h = 0.01$  m were assumed. This is within the bound derived in the section on DC acceleration.

#### 4.3 Nonlinear hydrodynamic effects

Although the nonlinear hydrodynamics of our oscillator are not well known, for translational motion of an object of size  $R$ , one expects the onset of nonlinearity near a Reynolds number  $Re \approx 1$ . Using the nominal radius  $R$  as the characteristic length for our screen gives

$$Re \equiv \frac{R \dot{x} \rho}{\eta} = \frac{2 R x_0}{\delta^2} \approx \frac{2(15 \mu)(14 \mu)}{(60 \mu)^2} = 0.12, \quad (14)$$

close enough to unity to suggest the need for experimental checks.

### 5. Temperature gradient

The extreme sensitivity of the fluid density on temperature places strict limits on temperature gradients. The chief source of such gradients is relaxation of the sample following temperature changes and this is dealt with in the section on equilibration. Here we only place a limit on the cell wall's temperature gradient. This is most easily estimated by equating it to the effect of a reduced gravitational field  $g^*$ . Using the value for  $g^*$  calculated in the next section, we estimate

$$\frac{dT}{dx} = \frac{(T_c/H_0) g^*}{\left[ \frac{T}{P_c} - \frac{\partial P}{\partial T} \right]} = \frac{(290 \text{ K}/536 \text{ m})(2.4 \times 10^{-4})}{(5.8)} = 2.2 \times 10^{-5} \text{ K/m}. \quad (15)$$

### B. Environment

#### 1. DC acceleration

In 1-g, the effects of gravity are essentially saturated at the reduced temperature

$\epsilon=2\times 10^{-6}$ . However, because this is not the case in low gravity, we used the restricted model equation of state to calculate the acceleration causing  $\Delta\rho/\rho=0.3\%$  at  $\epsilon_2=2\times 10^{-6}$ , at 10 mm from the middle of the cell. (The screen length is 19 mm.) The requirement is that the reduced gravity  $g^*$  be no more than  $2.4\times 10^{-4}$ .

### 2. Ambient temperature

The temperature  $T_{\text{air}}$  of the air surrounding the thermostat must be less than the critical temperature for the outer shell's temperature  $T_{\text{out}}$  to be controllable but not so cold that the outer shell's power is excessive. Based on limited laboratory experience we propose the limits

$$1 \text{ K} < (T_{\text{out}} - T_{\text{air}}) < 13 \text{ K} . \quad (16)$$

### 3. Vibration

Based on our tests of a similar screen oscillator viscometer described earlier, the vibration level at the sample should not exceed  $2\times 10^{-4} \text{ m}\cdot\text{s}^{-2}/\text{Hz}^{1/2}$  to prevent the noise-to-signal ratio at any spectrum analyzer bin from exceeding 0.1%. However, as in our ground-based tests, we plan to extract an average of adjacent frequency bins spanning a 0.5 Hz interval. This allows the vibration limit to be increased to  $8\times 10^{-4} \text{ m}\cdot\text{s}^{-2}/\text{Hz}^{1/2}$  ( $8\times 10^{-5} \text{ g}/\text{Hz}^{1/2}$ ).

### C. Control and data requirements

The level of automation will be roughly similar to that of the Zeno experiment, requiring little or no crew intervention. A central microcomputer will control the thermostat temperatures, drive and detect the motion of the oscillator, and periodically record the temperatures of the cell and thermostat shells as well as miscellaneous variables such as the capacitance bridge's drive amplitude.

An occasional data link to Earth ( $\sim 10^4$  bits/second, though not "real time") will be needed to: (1) monitor the progress of the experiment, (2) input new software control variables (e.g. temperature settings) if needed, and (3) interrupt or restart the control program in case of unusual problems.

Crew involvement should not be necessary except for perhaps turning on the experiment itself. This assumes that some ground-based monitoring and control for troubleshooting purposes will be possible during the flight.

Most of the data storage will be needed to record the oscillator's drive and detection voltages. Recording two 16 bit channels at 25 Hz for 10 days will require 2.2 Mbyte if the frequency responses are averaged over 20 minutes, 82 Mbyte if not averaged.

Table 2: Summary of main requirements, assuming 5 Hz operation

Temperature range	$(T_c + 60 \text{ mK})$ to $(T_c + 0.6 \text{ mK})$	
Viscometer precision	$\Delta\eta/\eta$	0.18%
Density accuracy	$ \rho - \rho_c /\rho_c$	0.3%
Temperature stability	$\Delta T$	29 $\mu\text{K}$
Temperature resolution	$\Delta\epsilon/\epsilon$	0.05
Temperature gradient	$dT/dx$	22 $\mu\text{K}/\text{m}$
Shear rate	$S$	15 $\text{s}^{-1}$

DC acceleration/g  
Vibration

$g^*$

$$2.4 \times 10^{-4}$$
$$8 \times 10^{-4} \text{ m} \cdot \text{s}^{-2} / \text{Hz}^{1/2}$$

## 6. EQUILIBRATION: IS A STIRRER NEEDED?

After removing gravity as a cause of density inhomogeneity, the design of the Critical Viscosity Experiment must eliminate other causes as well. We show here that, based on our understanding of equilibration near the critical point gained in the last three years, we can reliably quantify these other causes. We pay particular attention to inhomogeneities caused by temperature changes and show that our use of a slow temperature ramp in the one-phase region eliminates the need for a stirrer.

The following discussion is based on the requirement that differences in the density from  $\rho_c$  within the viscometer must be less than 0.3% and uses the estimated heat capacity and thermal conductivity of xenon at 1 mK above  $T_c$  for illustrations. First, we mention the physics behind the problem of density inhomogeneities. Then, four possible causes of density inhomogeneity are identified, followed by discussions of stirrer design and an estimate of the ramp rate consistent with the homogeneity requirement.

### A. Evolution of inhomogeneities induced by temperature gradients

The thermal equilibration of a pure fluid is known to be greatly influenced by the extreme compressibility near the critical point. As a result, the conventional heat transfer equation for a closed cell of volume  $V$ ,

$$\dot{T} = D_T \nabla^2 T, \quad (1)$$

must be replaced by the modified heat transfer equation,

$$\dot{T} - (1 - \gamma_c^{-1}) \left[ \frac{1}{V} \right] \int \dot{T} d^3x = D_T \nabla^2 T, \quad (2)$$

where  $D_T$  is the thermal diffusivity and

$$\gamma_c \equiv \frac{c_P}{c_V} \quad (3)$$

is the ratio of heat capacities at constant pressure and constant volume. This result was first articulated by Onuki, et al. [42] in 1989 and other papers on this subject have followed [43–47]. The main consequence of Eq.(2) is that, for a typical experimental cell of 1 cm size at a temperature within 0.1 K above  $T_c$ , all but the final part of the temperature equilibration is extremely fast, on the order of seconds. The final residual temperature gradient is small, of order  $\gamma_c^{-1}$  of the original disturbance, and decays very slowly. Though small, it has a significant effect on the density through the diverging value of the susceptibility  $(\partial\rho/\partial T)_P$ . The resulting density inhomogeneity can significantly affect the correlation length, and thus the viscosity near  $T_c$ .

In general the size of the density inhomogeneity depends on its cause and, should the cause be removed, on the relaxation time required for the inhomogeneity to disappear. The longer the length over which a density inhomogeneity is created, the longer its relaxation time. Use of a stirrer does not change the relaxation times but it potentially can reduce the amplitudes of the inhomogeneities associated with the longest relaxation times.

### B. Validity of the equilibration model

Our conclusion that a slow temperature ramp eliminates the need for a stirrer will

come from an analysis based on Eq.(2). Our confidence in Eq.(2) comes from its successful use in the analysis of three previous experiments. The first of these, an analysis of relaxation in a helium thermal conductivity cell at Duke University, is the only quantitative verification so far published [46]. The relaxation observed following changes in the vertical temperature difference was well described using only the shortest length, namely the height of the disk-shaped cell, in the one-dimensional form of Eq.(2). Consideration of the relaxation of lateral gradients was not required, presumably because gravity and the thick copper ends minimized such asymmetries.

The second experiment was a series of measurements of the relaxation of lateral density profiles within a 10 mm diameter, disk-shaped cell containing  $\text{SF}_6$  near its critical point. The final, equilibrium profile was either non-uniform, due to gravitational stratification [48,49], or uniform, in low gravity [54]. For both cases, our analysis has used Eq.(2) and assumes that the relaxation is governed only by the diffusion of heat along the shortest length, namely the 1 mm gap between the sapphire windows defining the sample volume. Both gravity and lateral fluid flow (parallel to the window faces) are ignored [55]. Fig. 6.1 shows the time constants measured in 1-g. The slanted line, indicating the result of Eq.(2) and the above assumptions, falls about a factor of 2 below the measurements. Some, though not most, of this discrepancy can be attributed to the finite thermal conductivity of the sapphire windows. In contrast, if the sapphire windows were replaced by insulating walls, the radius of the cell would become important in the analysis, and the predicted time constants would increase by a factor of 17. Preliminary analysis of data from the 0-g measurements has yielded time constants in agreement with the 1-g time constants, verifying the assumption that gravity determines the final density profile but not the speed of the final approach to equilibrium.

The third experiment was the  $\text{SF}_6$  heat capacity experiment of Nitsche and Straub, flown on the D-1 Shuttle mission [50-52]. As Fig. 6.2 shows, low-gravity apparently greatly lengthened the equilibration time of their sample. Nitsche and Straub initially expected that the equilibration time would be governed by the height  $H$  of their disk-shaped cell according to

$$\tau_H = \frac{H^2}{\pi^2 D_T}, \quad (4)$$

and this was indeed consistent with their 1-g measurements before and after the flight. However, without gravity to hold the liquid phase to the bottom of the cell, a much longer time constant  $\tau_R$ , characteristic of the time needed to move heat along the cell radius  $R$ , came into play. Unlike the second example, where the sapphire windows provided a thermal "short circuit" along the diameter of the cell, Nitsche and Straub used thin stainless steel walls in order to reduce the container's heat capacity. We therefore estimated this time constant as the product of the heat capacity of the sample multiplied by the thermal resistance of the walls. Dropping most factors of order unity, we calculated

$$\tau_R \approx (\rho c_P R^2 H) \left[ \frac{R}{(0.4H)R\lambda_s} \right] = \left[ \frac{\lambda}{0.4\lambda_s} \right] \frac{R^2}{D_T} \quad (5)$$

where the factor of 0.4 is the ratio of wall to sample thicknesses and  $\lambda_s$  and  $\lambda$  are the steel wall and sample thermal conductivities. In Table 3 below, the times  $\tau_H$  and  $\tau_R$  are compared to the time required to sweep from  $T_c$  up to  $T$ , namely  $\tau_{\text{ramp}} \equiv (T - T_c)/\dot{T}$ , at

the speed of  $\dot{T}=10$  mK/hour. (The slowest ramp, at 3.6 mK/hour, stopped at 50 mK above  $T_c$ .)

Table 3: Times derived from the D-1 heat capacity experiment

$(T-T_c)/\text{mK}$	$\tau_H/\text{hours}$	$\tau_R/\text{hours}$	$\tau_{\text{ramp}}/\text{hours}$
10	0.64	107	1
30	0.31	27	3
100	0.12	6	10

Comparison of  $\tau_{\text{ramp}}$  to  $\tau_R$  suggests the sample never had sufficient time to homogenize the two-phase inhomogeneity. Therefore, after accounting for the thin walls of the cell, the equilibration effects seen by Nitsche and Straub are consistent with our present understanding of equilibration near the critical point.

To avoid large density gradients, our plan for the flight experiment will differ from the D-1 experiment in three important respects. First, the cell walls will be made of copper sufficiently thick to provide a thermal short circuit along the length of the cell. Second, our ramps will start above  $T_c$  to avoid density inhomogeneities caused by a large-amplitude "memory" of two-phase separation. Finally, our ramp rates will be sufficiently slow so that the viscosity measurements will yield results indistinguishable from measurements taken at constant temperature.

### C. Four possible causes of density inhomogeneity

#### 1: Starting the experiment in the two-phase region

Unlike the experiment of Nitsche and Straub discussed above, the plan for the Critical Viscosity Experiment calls for starting in a well-equilibrated state 3 K above  $T_c$ , where the equilibration time is about 1 hour, and collecting all data before crossing  $T_c$ . This avoids the problem of an initial density inhomogeneity created by the previous coexistence of liquid and vapor phases.

#### 2: Electric fields

The electric field associated with the viscometer's electrostatic drive is less than  $3 \times 10^4 \text{ V} \cdot \text{m}^{-1}$ . Density deviations caused by its spatial derivative will be negligible.

#### 3: Cell wall temperature gradient

A static temperature gradient ( $dT/dx$ ) along the cell wall will induce a density difference of

$$\Delta\rho = \left[ \frac{d\rho}{dT} \right]_P \left[ \frac{dT}{dx} \right] \Delta x. \quad (6)$$

Using the screen's half-length of 10 mm for  $\Delta x$  leads to the specification of

$$-\frac{dT}{dx} \leq 2.2 \times 10^{-5} \text{ K} \cdot \text{m}^{-1}. \quad (7)$$

This requirement can be met by careful thermostat design and operation.

#### 4: Changes in the cell temperature

This is the most troublesome source of inhomogeneity. After a change in the cell temperature, the xenon temperature, at radius  $r$  in the interior of the cylindrical cell, will lag behind the temperature of the wall at radius  $R$  and thus cause a radial density gradient. Following the initial fast equilibration, this density gradient will decay exponentially, so we first considered merely waiting several relaxation times for homogeneity following a temperature step. Unfortunately, at 1 mK above  $T_c$ , the viscometer's 19 mm diameter leads to an impractically long relaxation time of

$$\tau = \frac{R^2}{j_{11}^2 D_T} = \frac{(0.0095 \text{ m})^2}{(3.83)^2 (6 \times 10^{-12} \text{ m}^2 \cdot \text{s}^{-1})} = 12 \text{ days.} \quad (8)$$

Note that if the temperature step is sufficiently small, the amplitude of the induced density gradient will be less than 0.3%, thus allowing a valid viscosity measurement before waiting for complete relaxation. The limit of many such small temperature steps is of course a continuous temperature ramp, and the practicality of using a ramp is discussed in the next section.

#### D. Avoiding density gradients with a slow ramp

In order to cover the desired range of reduced temperature we plan to measure viscosity while the sample temperature is continuously ramped at the speed  $\dot{T}$ . Before considering the consequences of density variations caused by the ramp, we first note that the viscosity varies simply because the temperature varies during one viscosity measurement. In this length of time  $\Delta t$ , the viscosity will vary by an amount

$$\Delta\eta = (\dot{T} \Delta t) \frac{\partial\eta}{\partial T} + \frac{1}{2} (\dot{T} \Delta t)^2 \frac{\partial^2\eta}{\partial T^2} + \dots \quad (9)$$

Considering only the term of order  $\Delta t$  leads to a constraint on the ramp rate of

$$\dot{T} \leq \frac{1}{y} \left[ \frac{\Delta\eta}{\eta} \right] \left[ \frac{T - T_c}{\Delta t} \right] = \frac{1}{(0.04)} (0.002) \frac{(0.001 \text{ K})}{(1000 \text{ s})} = 5 \times 10^{-8} \text{ K} \cdot \text{s}^{-1}, \quad (10)$$

where  $y$  is the viscosity exponent. This constraint can be relaxed by noticing that the error need only be the difference between the viscosity averaged over  $\Delta t$  and the viscosity at the average temperature. The term of order  $\Delta t$  then cancels, leaving the constraint

$$\dot{T} \leq \left[ \left[ \frac{2}{y} \right] \left[ -\frac{\Delta\eta}{\eta} \right] \right]^{1/2} \left[ \frac{T - T_c}{\Delta t} \right] = 3 \times 10^{-7} \text{ K} \cdot \text{s}^{-1}. \quad (11)$$

Now consider the slower restriction on the ramp rate coming from viscosity errors of order

$$\Delta\eta = \Delta\rho \frac{\partial\eta}{\partial\rho}, \quad (12)$$

caused by the radial density difference induced by the temperature ramp. To estimate the induced density difference  $\Delta\rho$ , insert the form

$$T(r,t) = \sum a_n r^n + \dot{T}t \quad (13)$$

for the sample temperature into Eq.(2). One then finds that the sample temperature is quadratic in the radius,

$$T(r,t) = a_0 + \frac{T_r r^2}{4\gamma_c D_T} + T_t. \quad (14)$$

The density will therefore deviate from the average density  $\rho_c$  by the amount

$$\Delta\rho = \left[ \frac{\partial\rho}{\partial T} \right]_P [T(r) - T(r_c)] \quad (15)$$

where

$$r_c = 2^{-1/2} R \quad (16)$$

is the radius characterized by  $\rho(r_c) = \rho_c$ . Eq.(15) can be rewritten as

$$\left| \frac{\Delta\rho}{\rho_c} \right| \leq \frac{(j_{11}^2/8) \left[ \frac{A_c}{R^v} \right]}{\left[ \frac{T_c}{P_c} - \left[ \frac{\partial P}{\partial T} \right] \right] \frac{Z_c}{\rho_c}} \left[ \frac{T_r}{T_c} \right] \quad (17)$$

where, for xenon at 1 mK above  $T_c$ ,

$$\frac{A_c}{R^v} = \frac{(0.131 \text{ kg} \cdot \text{mole}^{-1})(1.01 \times 10^3 \text{ J} \cdot \text{kg}^{-1} \cdot \text{K}^{-1})}{(8.31 \text{ J} \cdot \text{mole}^{-1} \cdot \text{K}^{-1})} \cong 16 \quad (18)$$

$$Z_c = \frac{AP_c}{R\rho_c T_c} = \frac{(0.131 \text{ kg} \cdot \text{mole}^{-1})(5.84 \times 10^6 \text{ Pa})}{(8.31 \text{ J} \cdot \text{mole}^{-1} \cdot \text{K}^{-1})(1110 \text{ kg} \cdot \text{m}^{-3})(290 \text{ K})} = 0.286 \quad (19)$$

and

$$-\frac{T_c}{P_c} \left[ \frac{\partial P}{\partial T} \right]_{\rho_c} = 5.8. \quad (20)$$

Requiring that the density deviation  $|\Delta\rho/\rho|$  in Eq.(17) be less than 0.3% leads to a restriction on the ramp rate  $\dot{T}$  near  $T_c$ , namely

$$\dot{T} \leq 5 \times 10^{-8} \text{ K} \cdot \text{s}^{-1} \quad (21)$$

at  $T - T_c = 1 \text{ mK}$ . Though quite slow, this is nevertheless practical for a Shuttle mission.

(It happens that this same rate has already been used in a 1G measurement of the viscosity of  $\text{CO}_2$  near its critical point [4].) For example, the time required to cover the 5 mK region closest to  $T_c$  will be

$$\Delta t \approx \Delta T_c / T = (0.005 \text{ K}) / (5 \times 10^{-8} \text{ K} \cdot \text{s}^{-1}) = 1 \times 10^5 \text{ s} = 1 \text{ day}. \quad (22)$$

A strategy of adjusting the ramp rate to the reduced temperature will allow the full temperature range to be covered within four or five days.

#### E. Upper bound on density variations caused by temperature changes

The preceding estimate calculated the maximum ramp rate guaranteed to keep density deviations below 0.3%. However, the assumed temperature distribution of Eq.(14) is only the final steady state. Thus, close to  $T_c$ , the induced inhomogeneity will be less than the conservative prediction of Eq.(15). Here we calculate a bound on the density change  $\Delta \rho_{\text{in}}$  of the interior fluid resulting from an arbitrarily fast change in the wall temperature.

Imagine stepping the temperature of the cell wall from  $T_1$  down to  $T_2$ . This will create a thin, dense layer of fluid near the wall and lower the density in the rest of the cell by an amount

$$\Delta \rho_{\text{in}} = \int_{T_1}^{T_2} \left[ \frac{\partial \rho}{\partial T} \right]_S dT \quad (23)$$

Close to  $T_c$  this can be rewritten as

$$\frac{\Delta \rho_{\text{in}}}{\rho_c} = \frac{\rho_c}{P_c \left[ \frac{T}{P_c} \frac{\partial P}{\partial T} \right]} \int_{T_1}^{T_2} c_V dT. \quad (24)$$

Inserting a model form [1] for the heat capacity gives

$$\frac{\Delta \rho_{\text{in}}}{\rho_c} = \frac{0.143 \text{ ak}}{\alpha(1-\alpha)} \left[ \frac{T}{P_c} \frac{\partial P}{\partial T} \right]^{-1} [\epsilon_2^{1-\alpha} - \epsilon_1^{1-\alpha}], \quad (25)$$

where  $\epsilon_1$  and  $\epsilon_2$  are the initial and final reduced temperatures. Using the values for the parameters  $a$  and  $k$  for xenon and the extreme case of  $T_2 = T_c$ , one gets

$$\frac{\Delta \rho_{\text{in}}}{\rho_c} = -3.45 \epsilon_1^{1-\alpha}. \quad (26)$$

Thus, provided that starting state is homogeneous and less than 104 mK above  $T_c$ , the density in the cell's interior will change by less than 0.3% independent of the ramp rate toward  $T_c$ .

Several restrictions apply to the above bound on the density variation induced within the cell's interior. First, as is the case with the present viscometer, we assume the viscometer's oscillator operates entirely within the interior. Second, residual accelerations may cause the dense fluid layer to leave the wall and lead to problems, discussed in the next section in more detail. Finally, due to stratification, Eq.(26) does not apply in 1-g.

## F. Miscellaneous concerns

### 1: Movement of the dense wall layer to the interior

The residual "microgee" acceleration  $a$  in orbit is sufficient to cause the dense fluid layer, formed near the wall by a temperature change, to "fall" onto the oscillating screen within the relatively short time of

$$t_{\text{fall}} \leq \left[ \frac{2R}{a(\Delta\rho_{\text{wall}}/\rho_c)} \right]^{1/2} = \left[ \frac{2(0.0095)}{(9.8 \times 10^{-6})(0.003)} \right]^{1/2} = 804 \text{ s.} \quad (27)$$

This is not a problem provided the density deviation is 0.3% or less throughout the cell, as would be the case for a slow temperature ramp. However, even the formation of a dense fluid layer caused by a step down in the wall's temperature might be tolerable because, following the initial "fast equilibration" there are two competing processes: the layer "falls" in the direction of local gravity and the layer diffuses toward equilibrium density. When the layer has reached the thickness  $\Delta R$ , its diffusion time should be roughly

$$t_{\text{layer}} \approx \left[ \frac{\Delta R}{R} \right]^2 \tau \approx \left[ \frac{(\Delta\rho_{\text{in}})}{(\Delta\rho_{\text{wall}})} \right]^2 \tau, \quad (28)$$

where  $\Delta\rho_{\text{in}}$  and  $\Delta\rho_{\text{wall}}$ , the density deviations of the interior and of the wall layer, are related by conservation of mass. For the case of  $T - T_c = 1 \text{ mK}$  and  $\Delta\rho_{\text{wall}} = 0.003$ , the use of Eqs.(8) and (26) yields

$$t_{\text{layer}} \approx \left[ \frac{5 \times 10^{-5}}{0.003} \right]^2 (12 \text{ days}) = 290 \text{ s,} \quad (29)$$

uncomfortably close to the fall time. In other words, the wall layer can possibly fall into the center of the cell before it has sufficient time to diffuse back to equilibrium density. Therefore, in spite of Eq.(26)'s bound on the initial change of the interior fluid's density, the conservative ramp limits (e.g. Eq.(21)) calculated above should not be greatly exceeded.

### 2: Influence of the screen wire on the inhomogeneity.

The radius  $R_1$  of the nickel screen's wires is sufficiently small so that during a temperature change, heat goes directly from the wire into the fluid and not into the wall by metallic conduction. The cell's temperature distribution is thus affected by the presence of the wires. However, the following model suggests that, for a continuous ramp, this effect is negligible.

For the simplified case of a cylindrical cell containing a single nickel wire of radius  $R_1$  located on the axis of a cell of radius  $R_2$ , one can again solve Eq.(2) provided the form of Eq.(13) includes a logarithmic term:

$$T(r,t) = \sum a_n r^n + b \ln(r/R_1) + Tt. \quad (28)$$

The coefficient  $a_2$  remains the same and the coefficient  $b$  is determined by the requirement that, in steady state, the wire loses heat only through thermal conduction:

$$\pi R_1^2 \rho_1 c_1 T = 2\pi R_1 \left[ \frac{\partial T}{\partial r} \right]_{R_1}, \quad (29)$$

where  $\rho_1 c_1$  is the heat capacity per unit volume of the nickel wire. This leads to

$$b = \frac{R_1^2 T}{2\lambda} [\rho_1 c_1 - \rho_c c_V], \quad (30)$$

where  $\lambda$  is the fluid's thermal conductivity. Assuming  $R_1 = 10$  micrometers, at  $T - T_c = 1$  mK, the size of this term relative to the temperature difference formed without the wire's presence is

$$\frac{b \ln(R/R_1)}{a_2 R_2^2} = 2 \left[ \frac{\rho_1 c_1}{\rho_c c_V} - 1 \right] \left[ \frac{R_1}{R_2} \right]^2 \ln \left[ \frac{R_2}{R_1} \right] = 5 \times 10^{-5}. \quad (31)$$

The form of Eq.(31) suggests that the effect of a single screen wire is roughly proportional to its area of cross section. Thus the entire screen, which contains only 9 longitudinal wires, probably has a negligible effect on the temperature gradient, and thus also the density gradient.

#### G. Stirrer requirements

Instead of using such a slow ramp, we also considered making step changes in the temperature, using a stirrer to eliminate the long-wavelength inhomogeneities, and then waiting for the relaxation of any remaining short-wavelength inhomogeneities. Although this possibility would require further research we can estimate the requirements on such a stirrer, namely (1) the entire sample must be mixed within a time significantly shorter than longest density relaxation time, (2) the stirrer can occupy only part of the cell volume (say less than half) to make room for the viscometer itself, and (3) the stirrer must not create significant density gradients itself.

The need to avoid significant heating of the fluid leads to a lower bound on the time needed to stir the sample. To see this, we first note that the dissipation  $P$  produced by a perfectly efficient stirrer is of order

$$P \approx \rho L^2 v^3, \quad (23)$$

where  $\rho$  is the fluid density,  $L$  is the size of the stirrer, and  $v$  is the stirred fluid's velocity. The power  $P$  must not cause a density variation less than

$$\frac{\Delta \rho}{\rho} = \left[ \frac{T_c}{\rho_c} \frac{\partial \rho}{\partial T} \right] \frac{\Delta T}{T_c} \quad (24)$$

$$\approx \left[ \frac{T_c}{\rho_c} \frac{\partial \rho}{\partial T} \right] \frac{P}{L \lambda T_c} \quad (25)$$

$$\approx \left[ \frac{T_c}{\rho_c} \frac{\partial \rho}{\partial T} \right] \frac{\rho L v^3}{\lambda T_c} \quad (26)$$

This constrains the fluid velocity to be less than roughly

$$v = \left[ \frac{T_c \lambda \left[ \frac{\Delta \rho}{\rho} \right]}{\rho L \left[ \frac{T_c}{\rho_c} \frac{\partial \rho}{\partial T} \right]} \right]^{1/3} . \quad (27)$$

At 1 mK above  $T_c$ , and assuming  $L \approx 10$  mm, we estimate  $v \approx 4$  mm/s, which in principle should allow a similar size sample to be stirred in less than a minute. Note that Eq.(23) then gives a stirrer power of  $10^{-8}$  W, much lower than a previously reported miniature stirrer [53].

To our knowledge, no stirrer meeting the above requirements exists. Assuming one could be developed, necessary tests would include measurements of its power and its ability to efficiently mix the contents of the entire cell.

## 7. TURBIDITY FOR VERIFICATION OF $T_c$

The Critical Viscosity Experiment will need a precise location of the critical temperature  $T_c$  in order to correctly analyze the asymptotic behavior of the viscosity. This precision is approximately the same as the temperature stability required for the viscosity measurement nearest  $T_c$ , about  $\pm 29 \mu\text{K}$ . In a fluid at critical density, the location of  $T_c$  can be unambiguously defined by the appearance of separate liquid and vapor phases and, upon slowly cooling to just below  $T_c$ , one can see the time-dependent phenomena of growing domains and meniscus formation. Unfortunately, the Critical Viscosity Experiment does not allow visual observation, so some other indicator of  $T_c$  will be needed.

Here we compare the relative merits of using viscosity and using turbidity for detection of  $T_c$ . Both the accuracy and the precision of the detection are important. In both sections we first address the question of accuracy, namely whether the apparent  $T_c$  obtained from the viscosity data is the true  $T_c$ . Then we estimate whether the method has the required precision of  $\pm 29 \mu\text{K}$ .

### A. $T_c$ defined by viscosity

In our previous measurements near critical points [3,4] we used the viscosity itself to determine  $T_c$  by leaving it as a free parameter in the fit describing the temperature dependence of the viscosity. We justified this procedure by the theoretically expected dependence of viscosity on temperature. For the binary mixtures, this assumption predicted that the highest viscosity, and thus the highest oscillator decrement, would occur at the  $T_c$  found by the fitting procedure. Within experimental precision, we indeed found this to be the case for all but one of the 17 experimental runs.

For the pure fluids in 1g, the temperature dependence of the decrement is more complicated, with the maximum decrement occurring a few mK above  $T_c$ . Again we assumed the correctness of the theoretical description of this effect of stratification, found  $T_c$  by fitting to the data, and obtained both a good description of the data as well as viscosity exponents comparable to those for the binary mixtures. Thus the fitted  $T_c$ 's from our 1g experiments seem to be accurate to within the experimental precision.

The  $T_c$  obtained by fitting to low gravity viscosity data will have a precision which can be estimated by assuming that an error in the fitted value of  $T_c$  will cause the most corresponding error in the viscosity exponent (and not, for example, the amplitude). Then, assuming negligible noise in the temperature measurement, the error in  $T_c$  will be related to the relative error ( $\Delta y/y$ ) in the viscosity exponent by approximately

$$\Delta T_c = \epsilon_2 T_c (\Delta y/y) \ln(\epsilon_1/\epsilon_2), \quad (1)$$

where  $\epsilon_2$  and  $\epsilon_1$  are the closest and farthest reduced temperatures. As a check on Eq.(1) we substituted values from Table III of Ref. 2, defined  $\epsilon_1$  and  $\epsilon_2$  by the extrema of the decrement curves in Figs. 6 and 7 from Ref. 4, and subsequently found agreement between the estimated and actual  $\Delta T_c$ 's to within a factor of three. Thus Eq.(1) should be reliable for estimating how  $\Delta T_c$  will decrease when the viscosity measurement is pushed closer to  $T_c$ .

Because the low-gravity viscosity data will show significant temperature dependence a factor of 10 closer to  $T_c$  than the 1g data, the uncertainty  $\Delta T_{c,0g}$  in low gravity will be less than the uncertainty  $\Delta T_{c,1g}$  in the 1g measurement. Using the actual value of  $\Delta T_{c,1g}$  from Ref. 4 and assuming comparable precision in the viscosity measurement, from Eq.(1) we estimate

$$\frac{\Delta T_{c,0g}}{\Delta T_{c,1g}} = \frac{(\epsilon_{2,0g})}{(\epsilon_{2,1g})} \frac{[\ln(\epsilon_1/\epsilon_2)]_{0g}}{[\ln(\epsilon_1/\epsilon_2)]_{1g}}, \quad (2)$$

which gives  $\Delta T_{c,0g} = \pm 30 \mu K$ . This is slightly greater than the nominal specification of  $\pm 29 \mu K$ . However, in practice the effect on the precision of the viscosity exponent should be negligible because  $\Delta y/y$  is already less than 1% for the 1g data.

#### B. $T_c$ defined by turbidity

The turbidity is theoretically expected to increase monotonically as  $T_c$  is approached from above. Kopelman et al. [42] approached the critical point of a binary mixture of methanol and cyclohexane to within  $30 \mu K$  and found the temperature dependence of the turbidity agreed with theory. Their  $T_c$  was not a free parameter. Instead they located it to within  $3 \mu K$  by the onset of time dependence of the turbidity caused by growing domains of liquid and vapor. To within experimental precision, the  $T_c$  determined by one-phase turbidity measurements agreed with the actual  $T_c$ .

Using the time-independent portion of the turbidity  $\tau$  to locate  $T_c$  from a single turbidity measurement requires a precision  $\Delta \tau$  determined by

$$\Delta \tau = \left[ \frac{d\tau}{d \ln(\epsilon)} \right] \left[ \frac{d \ln(\epsilon)}{d\epsilon} \right] \left[ \frac{d\epsilon}{dT_c} \right] \Delta T_c. \quad (3)$$

Close to  $T_c$ , the turbidity depends linearly on  $\ln(\epsilon)$ :

$$\tau = a - b \ln(\epsilon), \quad (4)$$

where, using quantities defined in Ref. 41,

$$b = \frac{2\nu\tau_0}{(q_0\xi_0)^2}. \quad (5)$$

Thus the needed precision in the turbidity measurement is

$$\Delta \tau = -b \frac{\Delta T_c}{(T - T_c)}. \quad (6)$$

From Eq.(5), the value of  $b$  for xenon is

$$b = \frac{(2)(0.63)[(3.84)(9.6 \times 10^{-4} \text{ m}^{-1})]}{[(2\pi)(1.14)(6.33 \times 10^{-7} \text{ m}^{-1})^{-1}(1.9 \times 10^{-10} \text{ m})]^2} = 1.0 \times 10^3 \text{ m}^{-1}. \quad (7)$$

where the value of  $\tau_0$  for xenon was found from the known value for  $\text{SF}_6$  by

$$\frac{\tau_0(\text{Xe})}{\tau_0(\text{SF}_6)} = \frac{[(\partial n^2/\partial \rho)\chi_0]_{\text{Xe}}}{[(\partial n^2/\partial \rho)\chi_0]_{\text{SF}_6}} = 3.84 \quad (8)$$

Assuming a closest usable approach to  $T_c$  of  $\epsilon_2 = 2 \times 10^{-6}$ , Eq.(6) then estimates

$$\Delta\tau = (1.0 \times 10^3 \text{ m}^{-1}) \left( \frac{29 \text{ } \mu\text{K}}{580 \text{ } \mu\text{K}} \right) = 50 \text{ m}^{-1} . \quad (9)$$

Although this is comparable to the precision of roughly  $\pm 30 \text{ m}^{-1}$  in the measurements near  $T_c$  of Kopelman et al., the required relative turbidity error  $\Delta\tau/\tau$  for xenon will be about 2%, smaller than the  $\sim 20\%$  achieved in the methanol + cyclohexane mixture using an optical table layout. Thus a one-phase turbidity measurement would not have the required precision unless  $T_c$  was approached about 10 times more closely than required for the viscosity experiment. This would amount to observing the turbidity during a  $T_c$  crossing and is discussed in the next section.

### C. Turbidity while crossing $T_c$

If, as proposed for the Critical Viscosity Experiment, the temperature sweeps slowly down through  $T_c$ , below  $T_c$  the observed turbidity will include both the fluctuation-driven part discussed above, which occurs both above and below  $T_c$ , and an explicitly time-dependent part due to the growth of liquid and vapor domains. The domains' growth speed depends on the reduced temperature, and sufficiently close to  $T_c$  this second part will be suppressed. This behavior is suggested by recent test data from Zeno [56], where the transmission of a xenon sample was recorded during a temperature sweep of about  $-2 \text{ } \mu\text{K/s}$ . If the minimum transmission corresponds to  $T_c$  then  $T_c$  can be located to a precision of  $\Delta T_c \leq 24 \text{ } \mu\text{K}$ , sufficient for the purposes of the the viscosity experiment.

The shape of the curve of transmission vs. time is not yet quantitatively understood. Qualitatively it is consistent with two effects: an absolute minimum corresponding to the fluctuation-driven, time-independent part of the turbidity and a later local minimum caused by the time-dependent growth of two-phase domains. These two minima might become close enough to merge for a ramp rate slower than  $2 \text{ } \mu\text{K/s}$ , planned for our flight experiment. Assigning  $T_c$  to the minimum transmission may then be incorrect.

### D. Summary

Both viscosity and turbidity can be expected to locate  $T_c$  to within the required precision of  $29 \text{ } \mu\text{K}$ . The main advantage of adding a " $T_c$  detector" that uses turbidity is that it can provide an estimate of  $T_c$  independent from the viscosity measurement. This would add a desirable enhancement of the scientific credibility of the analysis of the viscosity data. However, before adding a turbidity apparatus to the flight experiment, three issues must be addressed:

(1) A turbidity " $T_c$  detector" will require an approach about 10 times closer to  $T_c$  than needed for the viscosity measurement; crossing  $T_c$  will be inevitable. Are there possible

problems caused by slow sample equilibration? Understanding the recently CPF experiment will be helpful here.

(2) Achieving sufficient precision  $\Delta\tau/\tau$  without significant heating of the sample must be demonstrated.

(3) We must be able to assign  $T_c$  with confidence to the observed minimum transmission when the xenon sample is ramped through  $T_c$  at a rate as slow as  $-0.3 \mu\text{K/s}$ .

## 8. PROPOSED FLIGHT EXPERIMENT

### A. Temperature vs. time

The execution of the flight experiment will be similar to that of the ground measurements. Frequency response and thermometry data will be recorded three times per hour as the temperature is swept down toward the critical temperature. However, a first set of measurements will be needed to verify the thermometer's location for  $T_c$  to within about 1 mK by equilibrating at  $T_c + 1\text{K}$ , dropping to  $T_c + 0.03\text{ K}$ , then sweeping down through  $T_c$  at  $-1 \times 10^{-6}\text{ K/s}$ . Although density disequilibrium caused by this fast rate may prevent the oscillator's maximum damping from occurring exactly at  $T_c$ , within 12 hours these measurements should locate  $T_c$  within the 3 mK needed for later runs.

The next set of measurements would start at  $T_c + 0.1\text{ K}$ , the temperature where 1-g effects become large, and go down toward  $T_c$ , with the ramp speed reducing twice per decade of reduced temperature until reaching  $T_c + 3\text{ mK}$ , after which the ramp rate would be  $-3 \times 10^{-8}\text{ K/s}$  until crossing  $T_c$ . This set would last about three days. A final set, lasting six days, would begin at  $T_c + 3\text{ K}$  and go down through  $T_c$ , with similar decreases of the the ramp speed.

### B. Components

To the extent allowed by the choice of carrier, the flight experiment's apparatus and procedure should be the same as that of the ground apparatus. However, in the following list we will include two important changes from the current laboratory version. One is addition of a simple measurement of turbidity as a verification of the location of  $T_c$ . The other is a change in the method of temperature measurement and control.

#### 1. Sample cell

The sample will be identical to the cell already described except (1) it will be made of copper instead of brass and (2) it will be some 3 mm longer to accommodate prisms for the turbidity measurement. The cell will be built and filled with xenon to within 0.3% of the critical density by the principal investigators.

#### 2. Thermostat

The flight viscometer should be very similar to that used for the tests described earlier. Minimal modifications may be needed to accommodate a turbidity measurement or to meet flight specifications of materials.

#### 3. Vibration isolation

The viscometer is designed to obtain useful data in the 0–10 Hz vibration environment typical of the Shuttle [57]. Shock mounting of the thermostat may be necessary to prevent damage during launch.

#### 4. Electronics

##### 4.1 Ratio transformer

We currently use a commercial 6-decade programmable model (Eaton PRT-10C) to set the initial null of the capacitance bridge. Further adjustments are required only by density distribution changes caused by gravity, and then only when the plane of the screen is horizontal. However, although a fixed ratio transformer should therefore be sufficient for the flight experiment, launch stress changes might possibly change the screen's equilibrium

position. We therefore propose a limited range device having a ratio equal to the nominal ratio  $+ (0.004)N$  where  $N$  can be integer between  $-16$  and  $+16$ .

#### 4.2 Capacitance bridge oscillator

This provides a 10 kHz sine wave at a 1–2 V amplitude, stable to 0.1%.

#### 4.3 Capacitance bridge lock-in amplifier

We currently use Ithaco's model 393 at 10 kHz and at fixed phase on the  $30 \mu\text{V}$  range with the minimum 1.25 ms time constant. A smaller substitute must have comparable linearity, gain, and time constant and include a preamplifier with comparable input noise and impedance.

#### 4.4 Screen driver

We currently use the chirp source of the spectrum analyzer as input to a square root amplifier. A substitute circuit should have comparable specifications of noise and of amplitude and frequency accuracy. We propose emulation of the chirp waveform used by Hewlett Packard, namely a 12.5 Hz sweep lasting 32 s.

#### 4.5 Screen force and position measurement

The voltage proportional to the force applied to the screen (item 4.4) and the voltage proportional to the screen's position (item 4.3) must be periodically recorded for later construction of the frequency response. We propose a recording rate of 25 Hz, namely emulation of our commercial spectrum analyzer. Accuracy and linearity must be comparable as well.

#### 4.6 Temperature measurement and control

Although AC resistance bridges are commonly used for low-power measurement of temperature, the need for only 5% accuracy in the measurement of the reduced temperature (Eq.(8) of the Requirements section) suggests the use of a "preset" bridge whose null occurs close to  $T_c$ . Consider the circuit of Fig. 8.1 containing three fixed resistors  $R_0$  and a thermistor  $R_T(T)$ . The ratio of the output voltage  $V$  to the excitation voltage  $V_0$  is

$$\frac{V}{V_0} = 2 \left( \frac{R_T - R_0}{R_T + R_0} \right), \quad (1)$$

and, in the ideal case where the fixed resistors equal the resistance of the thermistor at  $T_c$ , namely

$$R_0 = R_T(T_c) \equiv R_c, \quad (2)$$

the output voltage is approximately proportional to the reduced temperature. The reduced temperature could then be inferred from the bridge's output voltage provided the stability and linearity of the electronics were better than the requirement on  $\Delta\epsilon/\epsilon$ , namely 5%.

In actuality,  $T_c$  can be determined on ground to no better than 1 mK. Suppose the error is as much as 10 mK. Then, at the closest approach to  $T_c$  the allowed error in the bridge's output voltage would be

$$\frac{\Delta V}{V} = \frac{\Delta T}{\Delta T_c} = \frac{(29 \mu K)}{(10 mK)} \approx 0.3\% . \quad (3)$$

Although such performance might require gain calibration of the lock-in amplifier following the bridge, it appears possible.

We therefore propose to measure the cell's temperature using a "preset" bridge detected by a lock-in amplifier. Because the reduced temperature will cover a range of more than  $10^5$  it will be necessary to have at least one step in the gain of the lock-in or in the amplitude of the bridge's exciting voltage.

The averaging time for the frequency response will be about 20 minutes. If only one number for the cell's temperature is recorded during this time period, it must be the temperature averaged over the same 20 minutes to allow proper comparison with the frequency response.

Measurement of the shell thermistors is less crucial and could be done by an ohmmeter, for example. However, we note that the steps  $\Delta T_{in}$  of the inner shell's temperature must be fine enough to produce a smooth ramp of the cell's temperature, namely

$$\Delta T_{in} = T \tau_{ext} = (3 \times 10^{-8} \text{ K/s})(2446 \text{ s}) = 70 \mu K . \quad (4)$$

#### 4.7 Turbidity

As discussed earlier, this would be a highly useful addition. The components would consist of a collimated, attenuated, solid-state laser, a silicon photodetector, and a pair of mirrors mounted on the end plate of the thermostat's outer shell. In addition, a pair of prisms defining the light path through the fluid would be glued to the inside of the cell's window. See Fig. 8.2.

#### 4.8 Acceleration

Crew motion or Shuttle maneuvers may occasionally create accelerations detrimental to either the sample homogeneity or the viscometer's performance. A continuous record of the acceleration of the viscometer will allow unambiguous interpretation of any disturbed viscosity data. The minimum requirement would be a record of the times when the local acceleration exceeded the vibration requirement stated earlier.

#### 4.9 Computer, telemetry, etc.

The requirements for remaining equipment must be compatible with the above requirements.

## 9. INVOLVEMENT OF THE PRINCIPAL INVESTIGATORS

### A. Supporting ground-based testing

It will be crucial to measure the sample's viscosity in the same cell and thermostat before flight. This will be a final test of the complete apparatus including the sample. The test will create a 1-g baseline for understanding the low-g measurements and reduce uncertainty in  $T_c$  caused by drift in either the sample's impurity level or in the thermometry electronics. A similar post-flight experiment, while less crucial, will verify the stability of sample and oscillator during the low-g experiment.

Weighing before and after flight will be necessary to verify that the sample cell did not leak during the flight. A pre-flight to post-flight waiting period of up to two years is acceptable.

The oscillating screen must be calibrated against the known viscosity of a comparable fluid in the absence of significant critical point effects. This will improve the present accuracy of about 10% to the required accuracy of 1%.

### B. Preparation of the flight experiment

The principal investigators will construct, fill, and characterize three to six more viscometer cells, one of which will be used for the flight experiment. Consultation with the flight engineers will be necessary to ensure that the flight experiment's scientific requirements are met. The principal investigators also anticipate undergoing NASA-required meetings and training in connection with flight experiment.

### C. Post flight data analysis

The raw data from the viscosity measurements will consist of the oscillator's frequency response and the sample temperature, as well as miscellaneous data such as shell temperatures and acceleration. NASA's assistance will be required to put the raw data into a format usable by the principal investigators. After this has been done, data analysis will be handled in the same manner as for the pre-flight tests except the acceleration record will be used to cull out invalid viscosity measurements.

Once the viscosity data have been properly reduced we will compare them against theoretical predictions as outlined in the Background section. An archival compilation of the data will also be prepared.

### D. Reflights

Examples of possibilities for reflights of the Critical Viscosity Experiment include measurements along isochores other than the critical one (i.e.  $\rho \neq \rho_c$ ) and measurements of another pure fluid such as  $\text{SF}_6$ ,  $\text{CO}_2$ , or a fluorocarbon. Measurement of nonzero frequency and shear effects in a near-critical fluid would be a next level challenge to the theory of dynamic critical phenomena. This would require a well-understood oscillator capable of operation up to 100 Hz. Closer approaches to the critical point without significant viscoelastic effects would require redesign of the oscillator to achieve a lower vacuum resonance frequency.

## REFERENCES

1. M.R. Moldover, J.V. Sengers, R.W. Gammon, and R.J. Hocken, *Rev. Mod. Phys.* 51,79 (1979).
2. M.R. Moldover, R.J. Hocken, R.W. Gammon, and J.V. Sengers, Overviews and Justifications for Low Gravity Experiments on Phase Transition and Critical Phenomena in Fluids, NBS Technical Note 925 (U.S. Government Printing Office, 1976); also published as NASA Contractor's Report CR-135070.
3. R.F. Berg and M.R. Moldover, *Int. J. Thermophys* 7,675 (1986); *J. Chem. Phys.* 89,3694 (1988).
4. R.F. Berg and M.R. Moldover, *J. Chem. Phys.* 93,1926 (1990).
5. R.F. Berg and M.R. Moldover, *Phys. Rev. A* 42, 7183 (1990).
6. R.F. Berg and M.R. Moldover, report to NASA (1989).
7. M.R. Moldover and R.W. Gammon, NASA Contractor's Report CR174637 (1983).
8. M.R. Moldover, Opportunities for Research in a Low-Gravity Environment, ed. G. Hazelrigg and J.R. Reynolds (AIAA, New York, 1986).
9. J.D. Van der Waals, Doctoral dissertation, Leiden (1873).
10. J.M.H. Levelt Sengers, *Physica* 73,73 (1974).
11. M.I. Bagatskii, A.V. Voronel, and V.G. Gusak, *JETP* 16,517 (1963); A.V. Voronel, V.G. Snigirev, and Yu.R. Chashkin, *JETP* 21,653 (1965); A.V. Voronel, Yu.R. Chashkin, *JETP* 24,263 (1967).
12. B.J. Widom, *J. Chem. Phys.* 43,3898 (1965).
13. J.V. Sengers and J.M.H. Levelt Sengers, *Ann. Rev. Phys. Chem* 37,189 (1986).
14. S.C. Greer and M.R. Moldover, *Ann. Rev. Phys. Chem.* 32,233 (1981).
15. M.R. Moldover, in Phase Transitions: Cargese 1980, ed. M. Levy, J.C. Le Guillou, and J. Zinn-Justin, (Plenum, New York, 1982).
16. P.C. Hohenberg and B.I. Halperin, *Rev. Mod. Phys.* 49,435 (1977).
17. J.V. Sengers, *Int. J. Thermophys.* 6,203 (1985).
18. J.C. Nieuwoudt and J.V. Sengers, *J. Chem. Phys.* 90,457 (1989).
19. T. Ohta, *J. Phys. C* 10,791 (1977).
20. J.K. Bhattacharjee and R.A. Ferrell, *Phys. Lett.* 76A,290 (1980); *Phys. Rev. A* 27,1544 (1983).
21. J.C. Nieuwoudt and J.V. Sengers, *Physica A* 147,368 (1987).
22. D.W. Oxtoby, *J. Chem. Phys.* 62,1463 (1975).

23. H.L. Swinney and D.L. Henry, Phys. Rev. A 8,2586 (1973).
24. J.V. Sengers, in Transport Phenomena — 1973, ed. J. Kestin, AIP Conf. Proc. No. 11, p. 229, (American Institute of Physics, New York, 1973).
25. H.J. Strumpf, A.F. Collings, and C.J. Pings, J. Chem. Phys. 60,3109 (1974).
26. L. Bruschi and G. Torzo, Phys. Lett. 98A,265 (1983).
27. C.C. Agosta, S. Wang, L.H. Cohen, and H. Meyer, J. Low Temp. Phys. 67,237 (1987).
28. P. Calmettes, Phys. Rev. Lett. 39,1151 (1977).
29. H. Hao, Ph.D. thesis, University of Maryland (1991).
30. K. Kawasaki, Ann. Phys. (N.Y.) 61,1 (1970).
31. R. Perl and R.A. Ferrell, Phys. Rev. Lett. 29,51 (1972); Phys. Rev. A 6,358 (1972).
32. T. Ohta and K. Kawasaki, Prog. Theor. Phys. 55,1384 (1976).
33. J.K. Bhattacharjee and R.A. Ferrell, Phys. Rev. A 28,2363 (1983).
34. G.A. Olchowy and J.V. Sengers, Phys.Rev. Lett. 61,15 (1988).
35. J.K. Bhattacharjee, R.A. Ferrell, R.S. Basu, and J.V. Sengers, Phys. Rev. A 24,1469 (1981).
36. K. Kawasaki, in Phase Transitions and Critical Phenomena, vol. 5A, p.165, ed. C. Domb and M.S. Green, (Academic, New York, 1976).
37. J.V. Sengers and J.M.J. van Leeuwen, Int. J. Thermophys. 6,545 (1985).
38. R.F. Berg and M.R. Moldover, report to NASA Lewis Research Center (1989).
39. G.G. Stokes, Mathematics and Physical Papers, Vol. III, p.11, Cambridge University: London (1922); reviewed by L.H. Dill and A.A. Oyediran, report to NASA Lewis Research Center, (1992).
40. A.M.J. Davis, report to NASA Lewis Research Center, contract C-32008-A (1992).
41. A. Chait, private communication.
42. A. Onuki, H. Hao, and R.A. Ferrell, Phys.Rev. A 41, 2256 (1990).
43. H. Boukari, J.N. Shaumeyer, M.E. Briggs, and R.W. Gammon, Phys. Rev. A 41, 2260 (1990).
44. B. Zappoli, D. Bailly, Y. Garrobos, B. Le Neindre, P. Guenon, and D. Beysens, Phys. Rev. A 41, 2264 (1990).
45. A. Onuki and R.A. Ferrell, Physica A 164, 245 (1990).

46. R.P. Behringer, A. Onuki, and H. Meyer, *J. Low Temp. Phys.* 81, 71 (1990).
47. H. Boukari, M.E. Briggs, J.N. Shaumeyer, and R.W. Gammon, *Phys. Rev. Lett.* 65, 2654 (1990).
48. L. Eicher, Semesterarbeit, Technical University, Munich (1991).
49. R.A. Wilkinson, R.F. Berg, R.W. Gammon, L. Eicher, M.R. Moldover, and J. Straub, poster presentation for the VIII Symposium on Materials and Fluid Sciences in Microgravity, Brussels, Belgium (1992).
50. J. Straub, R. Lange, K. Nitsche, and K. Kemmerle, *Int. J. Thermophys.* 7, 343 (1986).
51. K. Nitsche, Dissertation, Technical University, Munich (1990).
52. J. Straub and K. Nitsche, paper presented at the 11th Symposium of Thermophysical Properties, Boulder, CO, USA (1991).
53. R.F. Berg and N.P. De Luca, *Rev. Sci Instrum.* 62, 527 (1991).
54. R.A. Wilkinson, R.F. Berg, R.W. Gammon, M.R. Moldover, and J. Straub, data acquired from the Thermal Equilibration Experiment in the Critical Point Experiment during the IML-1 Space Shuttle mission (January 1992). Preliminary analysis by W. Johnson.
55. R.F. Berg, preprint (1992).
56. R. Gammon, private communication.
57. A. Wilkinson, private communication.

## FIGURES

1.1 The decrement, as a function of reduced temperature, of our old high- $Q$  torsion oscillator filled with xenon. The  $1g$  curve is the best fit to the data, and the upper curve shows the decrement expected if the experiment were repeated in low gravity. To first order, the asymptotic slope is  $y/2$ . Because the asymptotic region is unavailable in  $1g$ , determination of the viscosity exponent  $y$  strongly depends on the theories of stratification and of crossover between the noncritical and critical regions.

2.1 (a) Typical phase diagram for a simple fluid. (b) Typical phase diagram for a partially miscible binary mixture.

2.2 Example of the viscosity increase seen near binary mixture and liquid-vapor critical points. The liquid-vapor experiments (carbon dioxide and xenon) show increases of only 20% due to gravitational stratification.

2.3 An exaggerated sketch of the critical viscosity divergence superposed on a temperature-dependent noncritical viscosity  $\eta_0(T)$ .

2.4 A sectioned view of the high- $Q$  torsion oscillator used to measure the viscosity of carbon dioxide near its critical point.

2.5 The viscosity exponent  $y$  for four binary mixtures (denoted by nonstandard abbreviations) and two pure fluids. The abscissa  $B$  is a dimensionless measure of the background viscosity's temperature dependence. The theoretical line has recently moved up to  $y=0.040$ .

3.1 The density distribution of xenon in a 2 cm high cell at the reduced temperatures of  $10^{-3}$ ,  $10^{-4}$ , and  $10^{-8}$ . At temperatures close to  $T_c$ , Earth's gravity causes significant sample inhomogeneity.

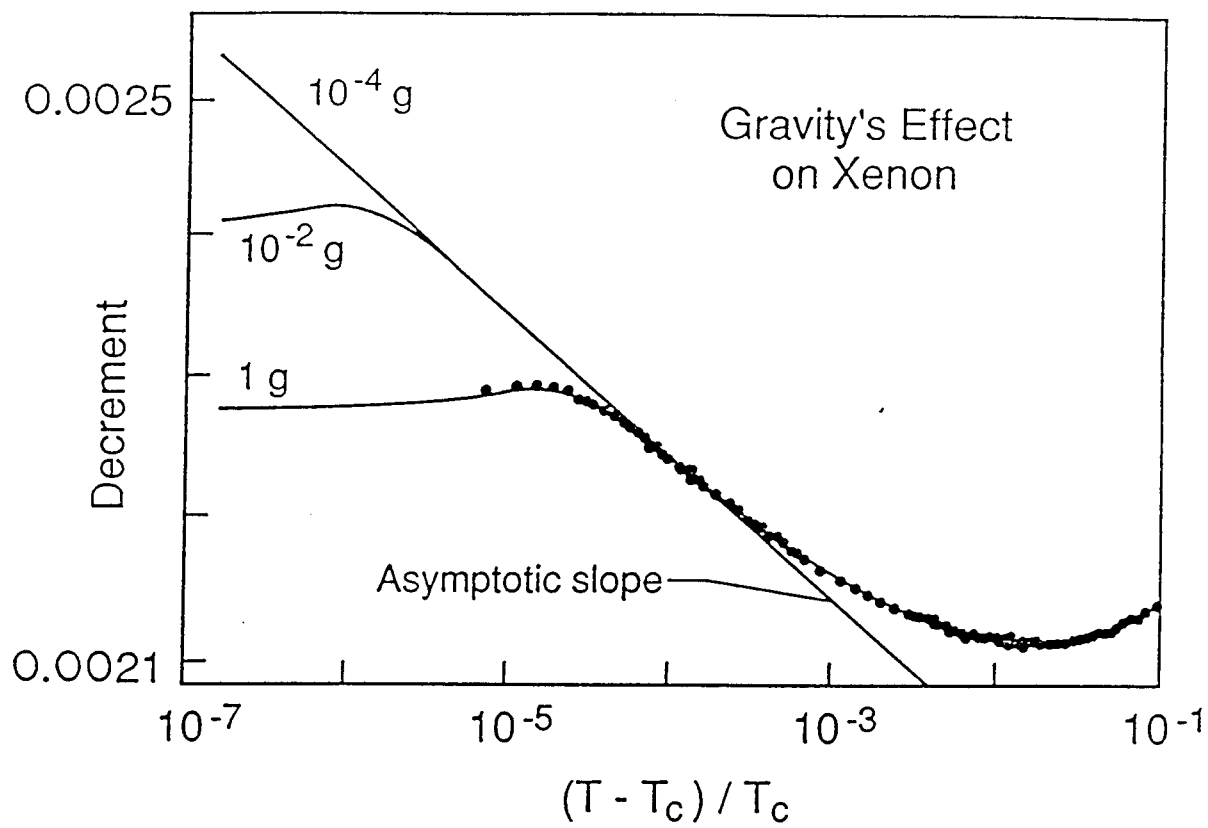
4.1 Conceptual summary of the new viscometer. The oscillator is driven by an electrostatic force, whose amplitude is recorded in channel 1 of the spectrum analyzer. Channel records the oscillator's amplitude, measured with a differential capacitance bridge and lock-in amplifier.

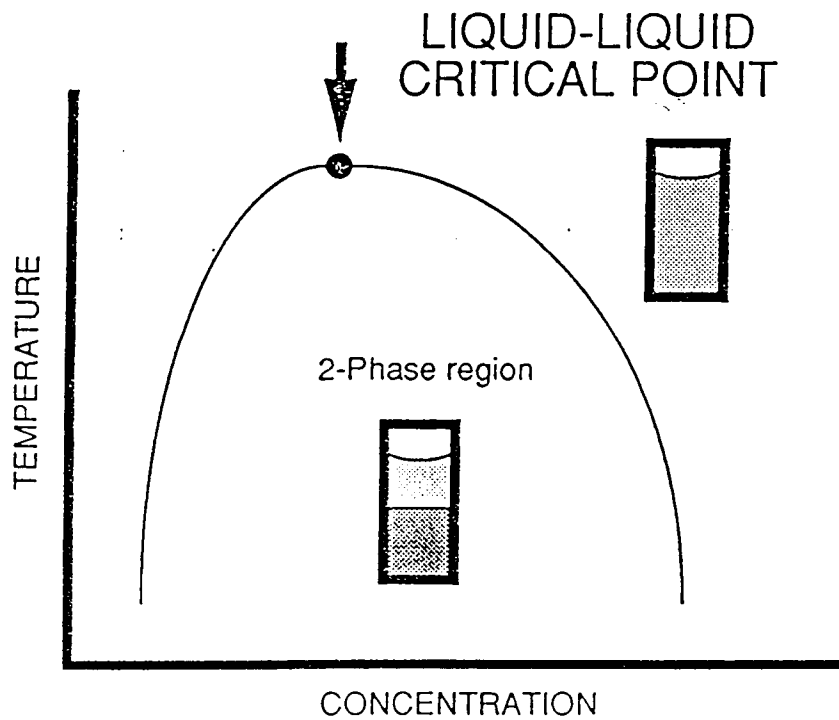
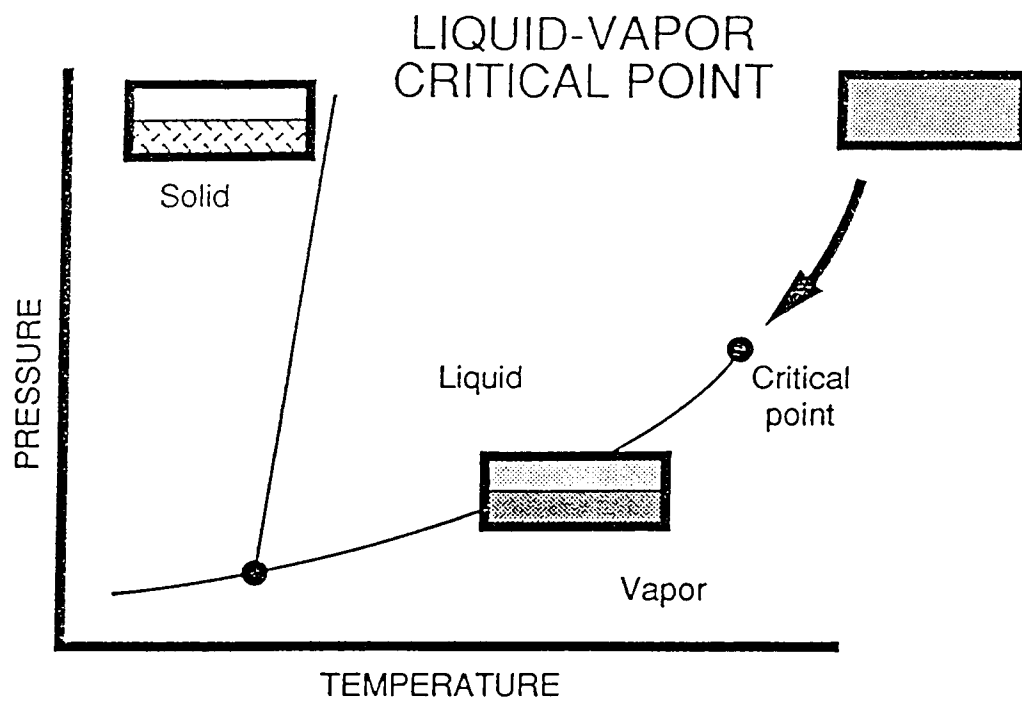
4.2 Approximate scaled drawing of the screen oscillator held in its copper wire bracket. Portions of grid wires form the torsion fiber. The square size is 847 micrometers and the wire width is about 27 micrometers.

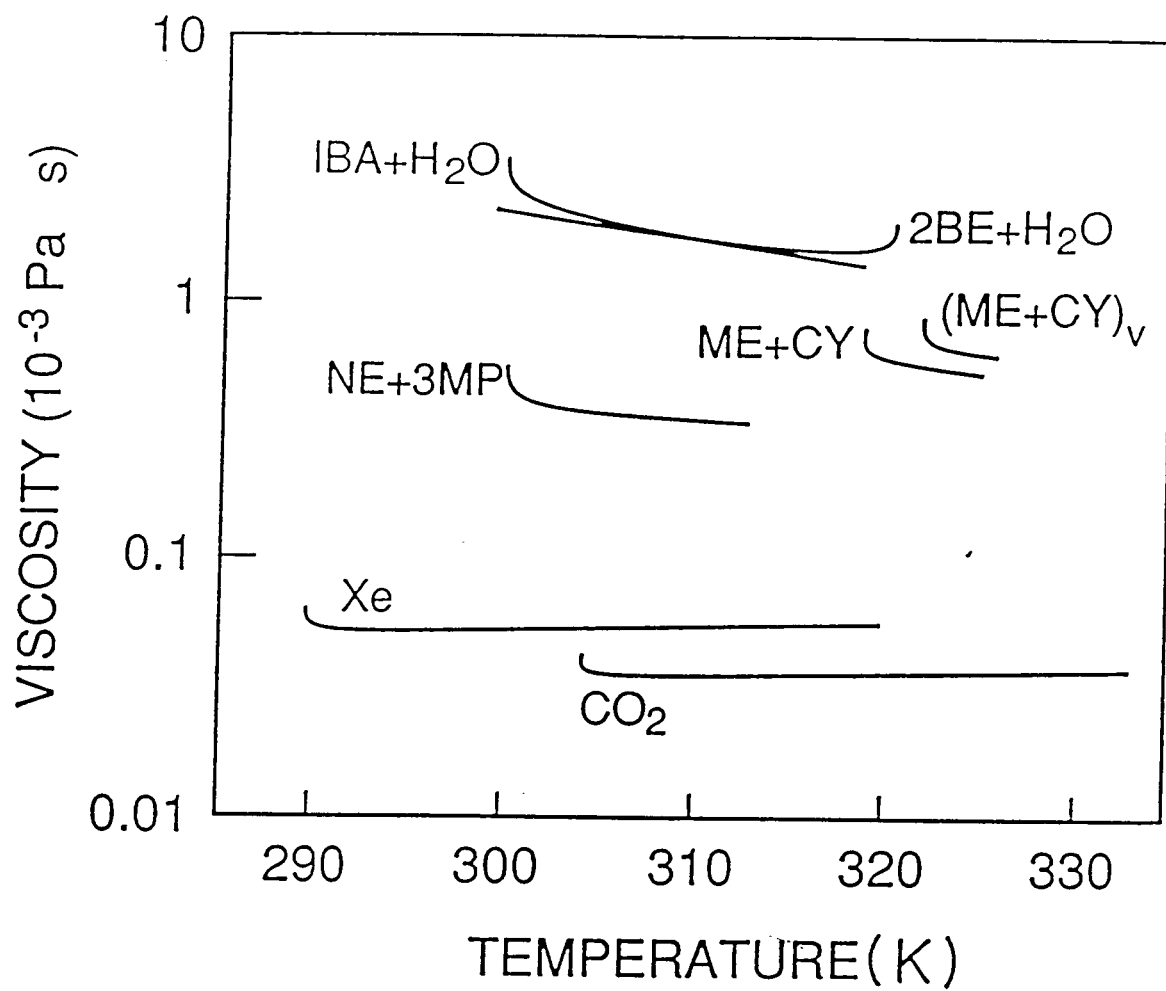
4.3 Approximate scaled drawing of the viscometer cell. The screen motion, shown exaggerated, is driven and detected by the four adjacent stationary electrodes.

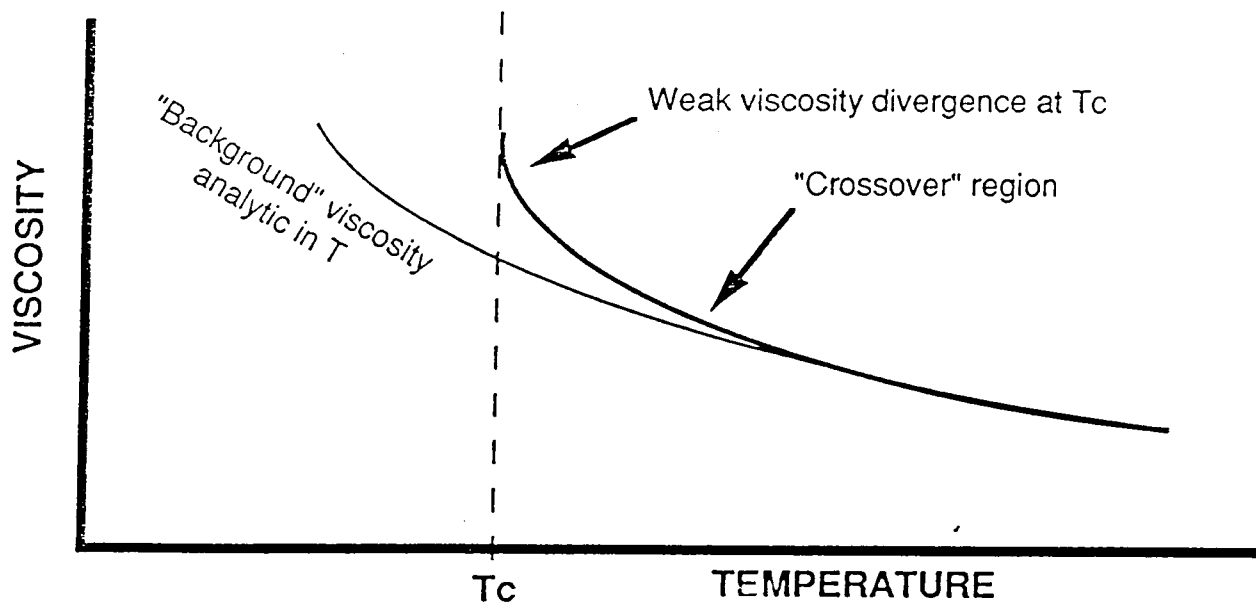
4.4 The screen oscillator's frequency response in vacuum. Application of 100  $V_{DC}$  on one of the electrode pairs lowered the resonance frequency from 11.03 to 10.35 Hz.

4.5 The electronic circuit used for drive and detection of the oscillating screen. The sinusoidal drive signal from the source of the spectrum analyzer is modified by the square root amplifier, then filtered against 10 kHz noise. Resulting motion of the screen is measured by the differential capacitance bridge, driven at 10 kHz and detected by a lock-in amplifier. The additional passive components allow simultaneous use of the four fixed electrodes by the drive and detection voltages.





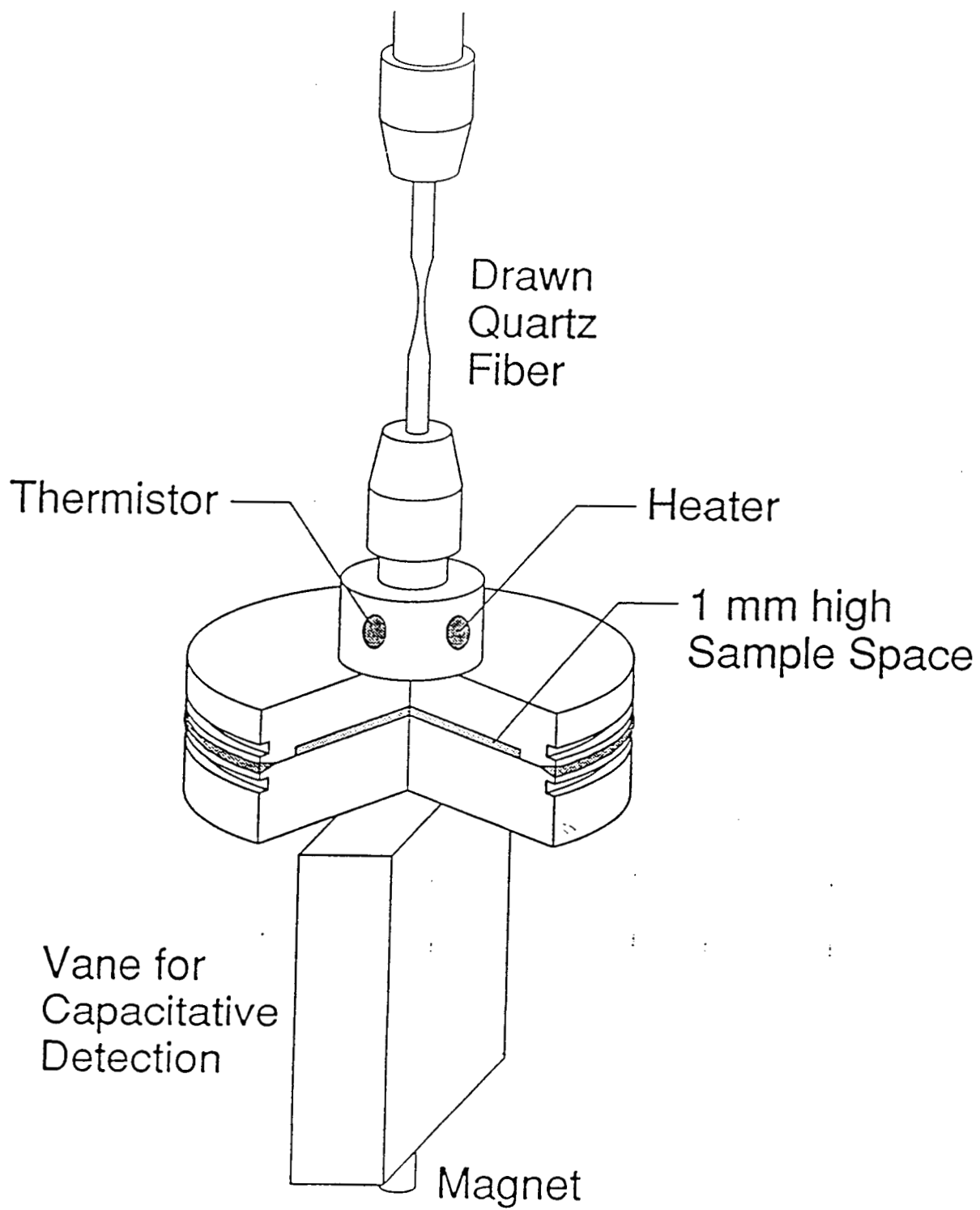


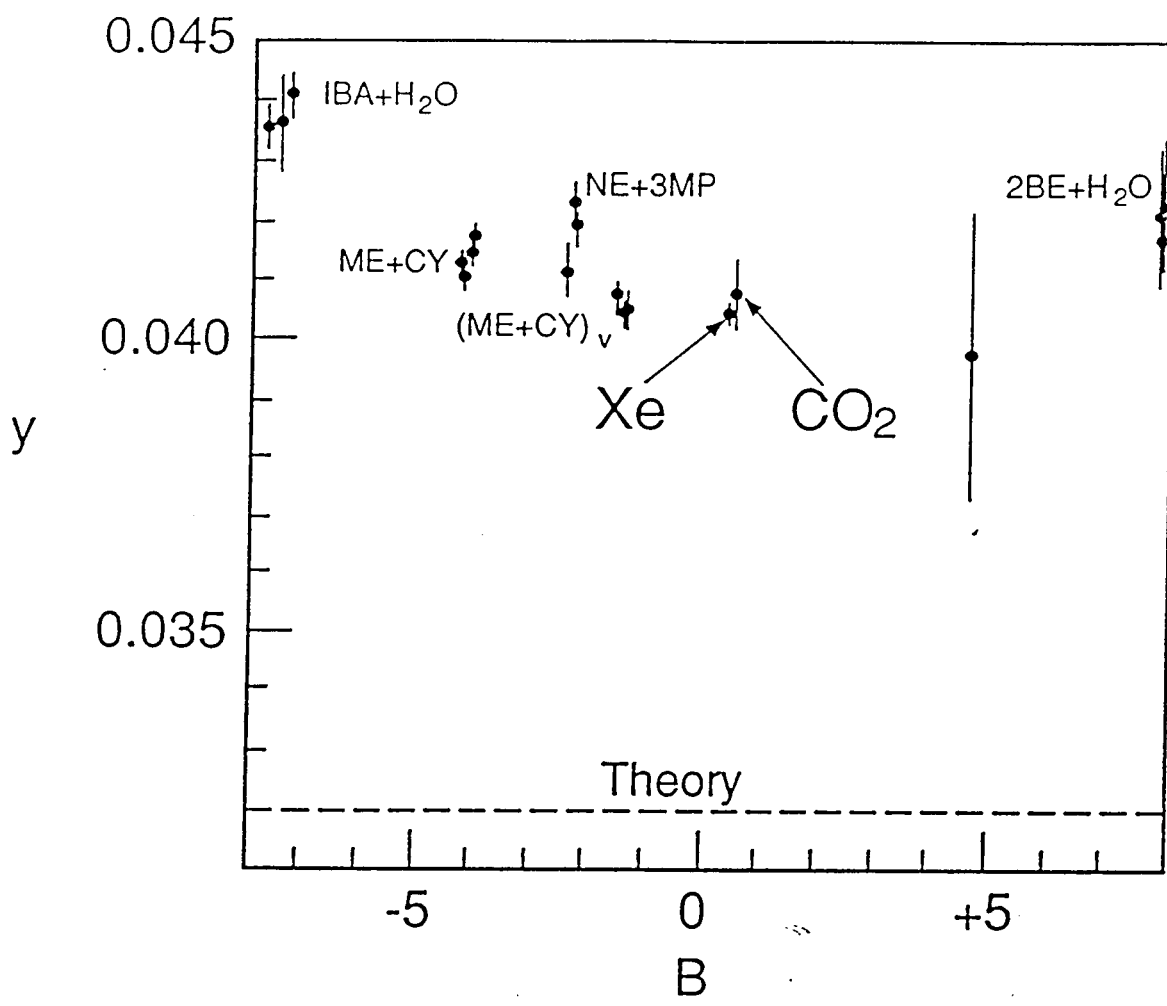


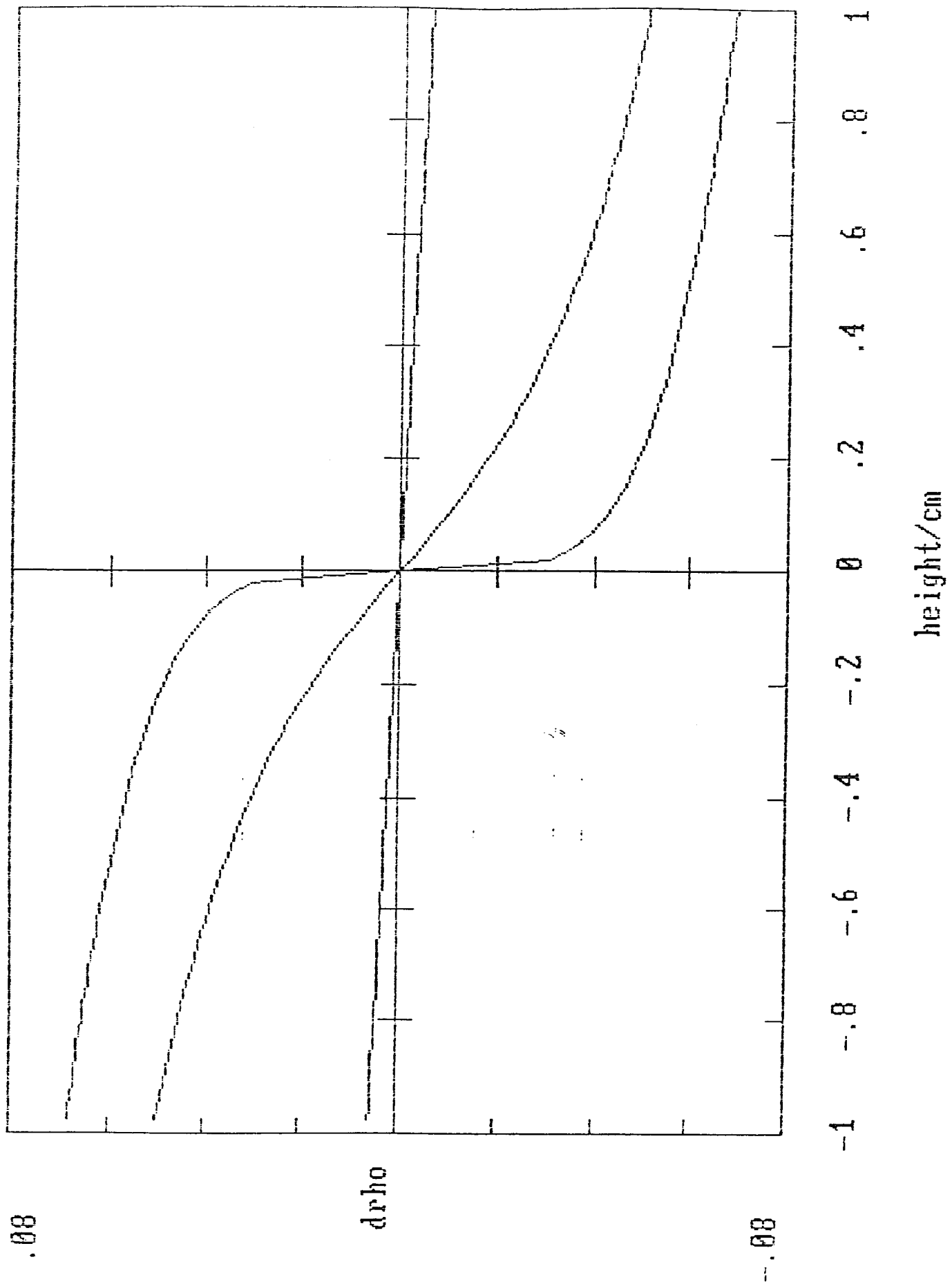
$$\eta = \eta_0(T) [(T - T_c)/T_c]^{-y}$$

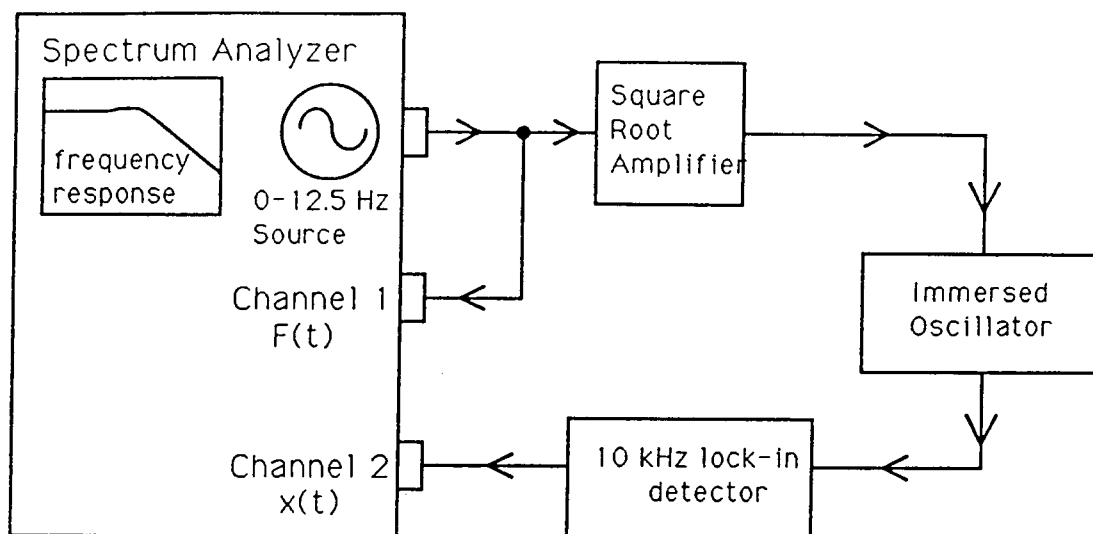
Viscosity exponent

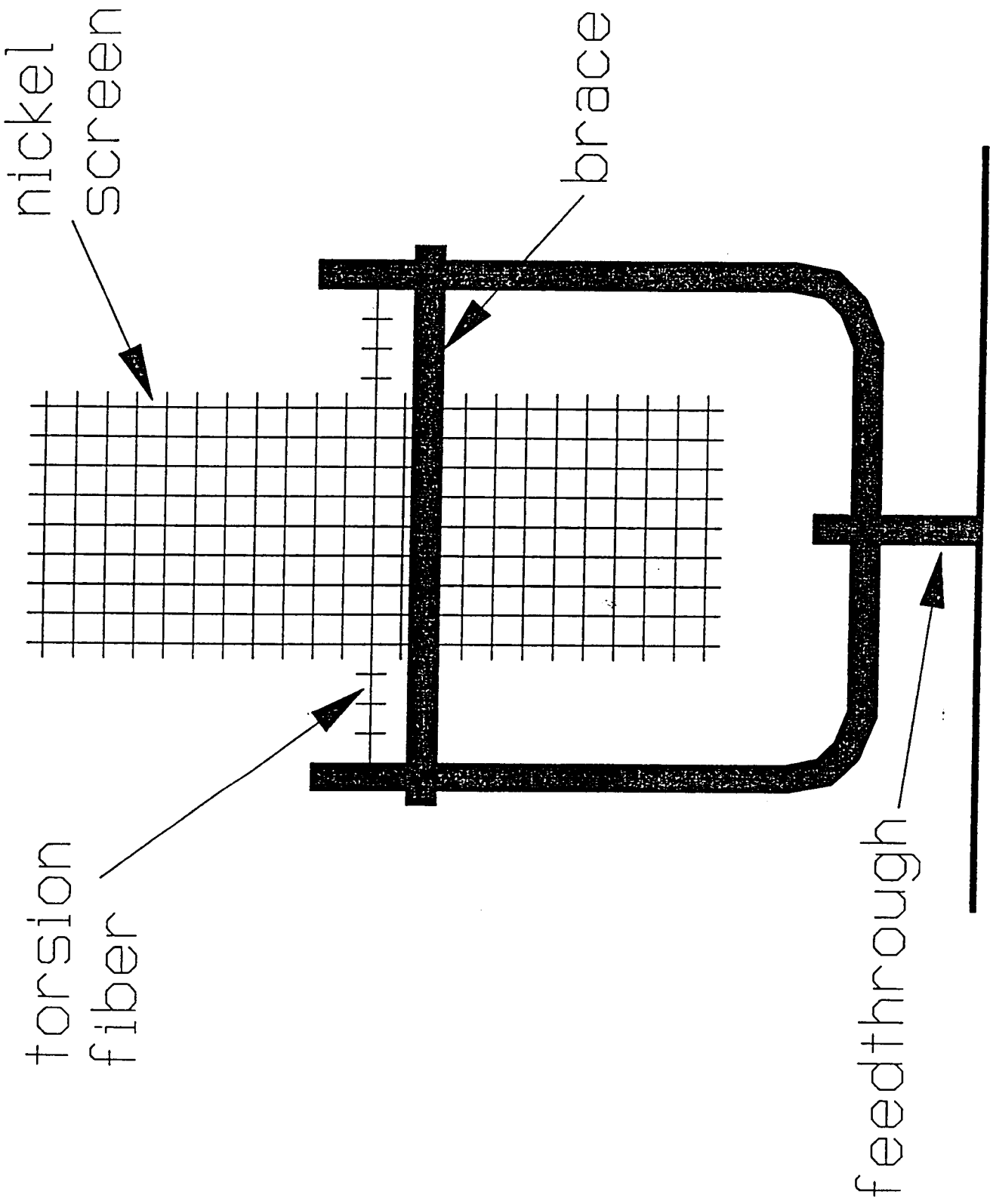
Multiplicative form of background viscosity



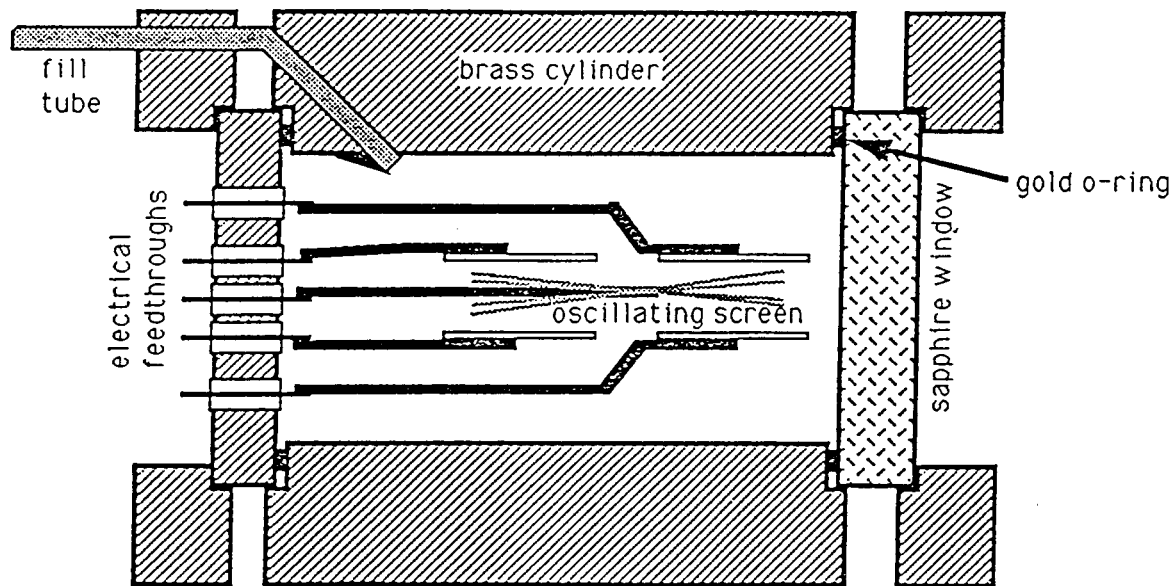








# PROTOTYPE CELL FOR XENON MICROVISCOMETER



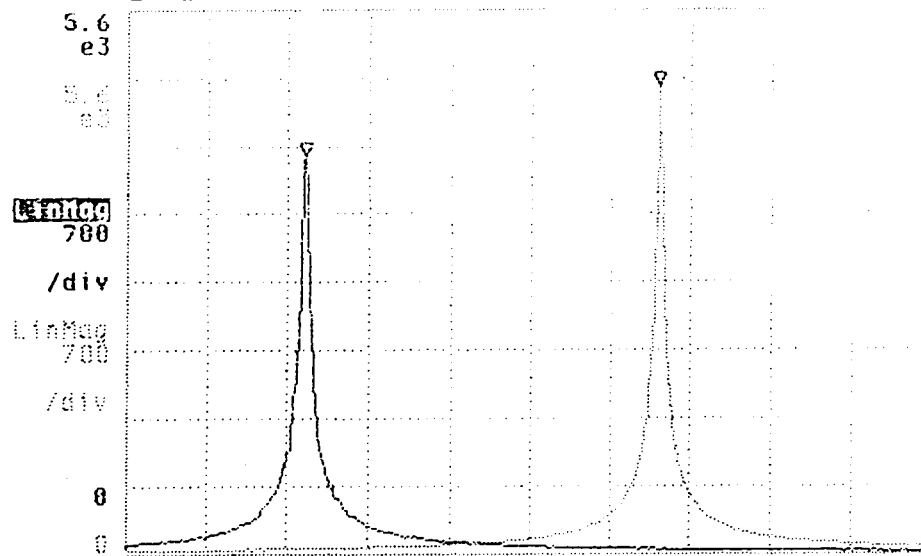
Status: ON  
Tune: RANDOM

Level: 50 mVrms  
SineFq: 500 mHz  
Src

Meas

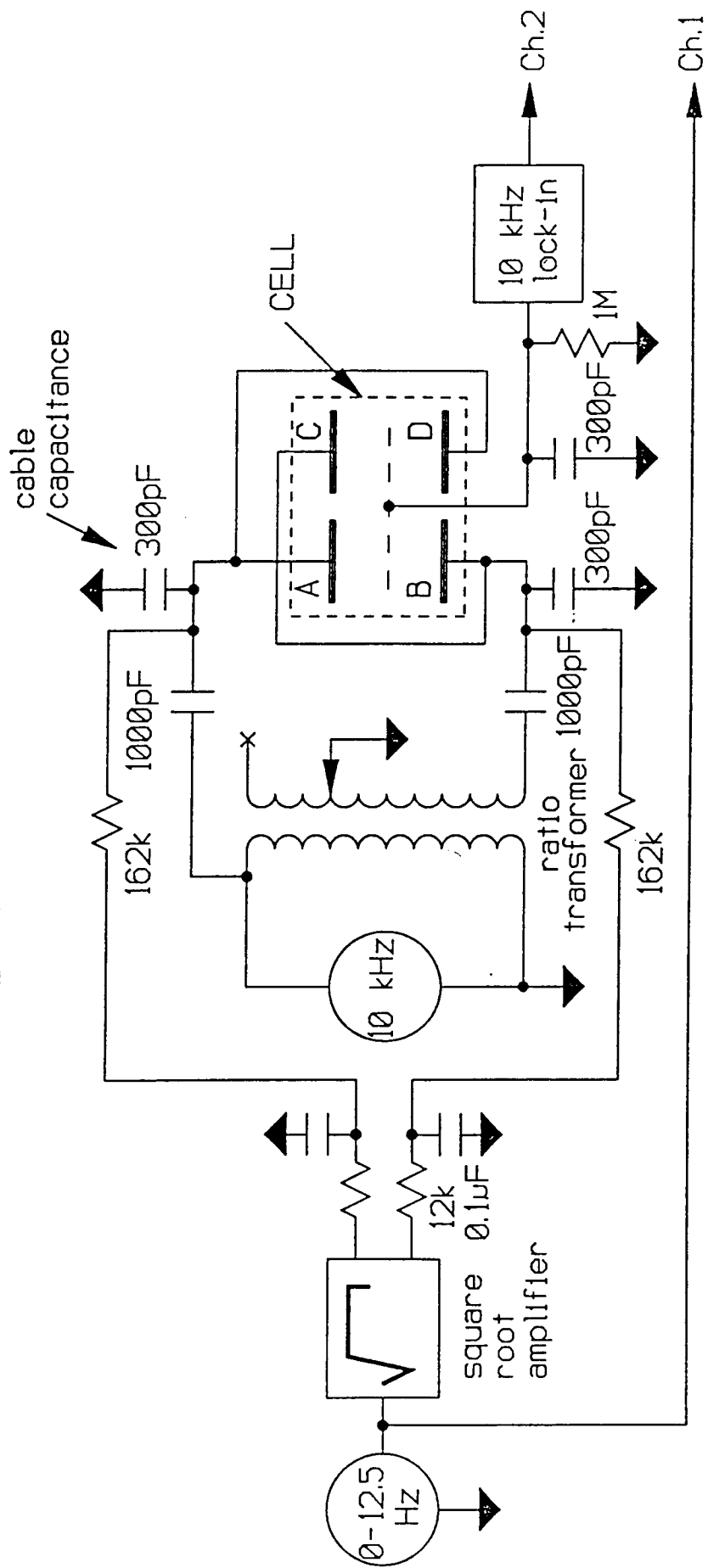
~~STATUS: MEASUREMENT IN PROGRESS~~

A Marker X: 10.3476562 Hz Y: 4.083 e3  
B Marker X: 11.04125 Hz Y: 3.707 e3

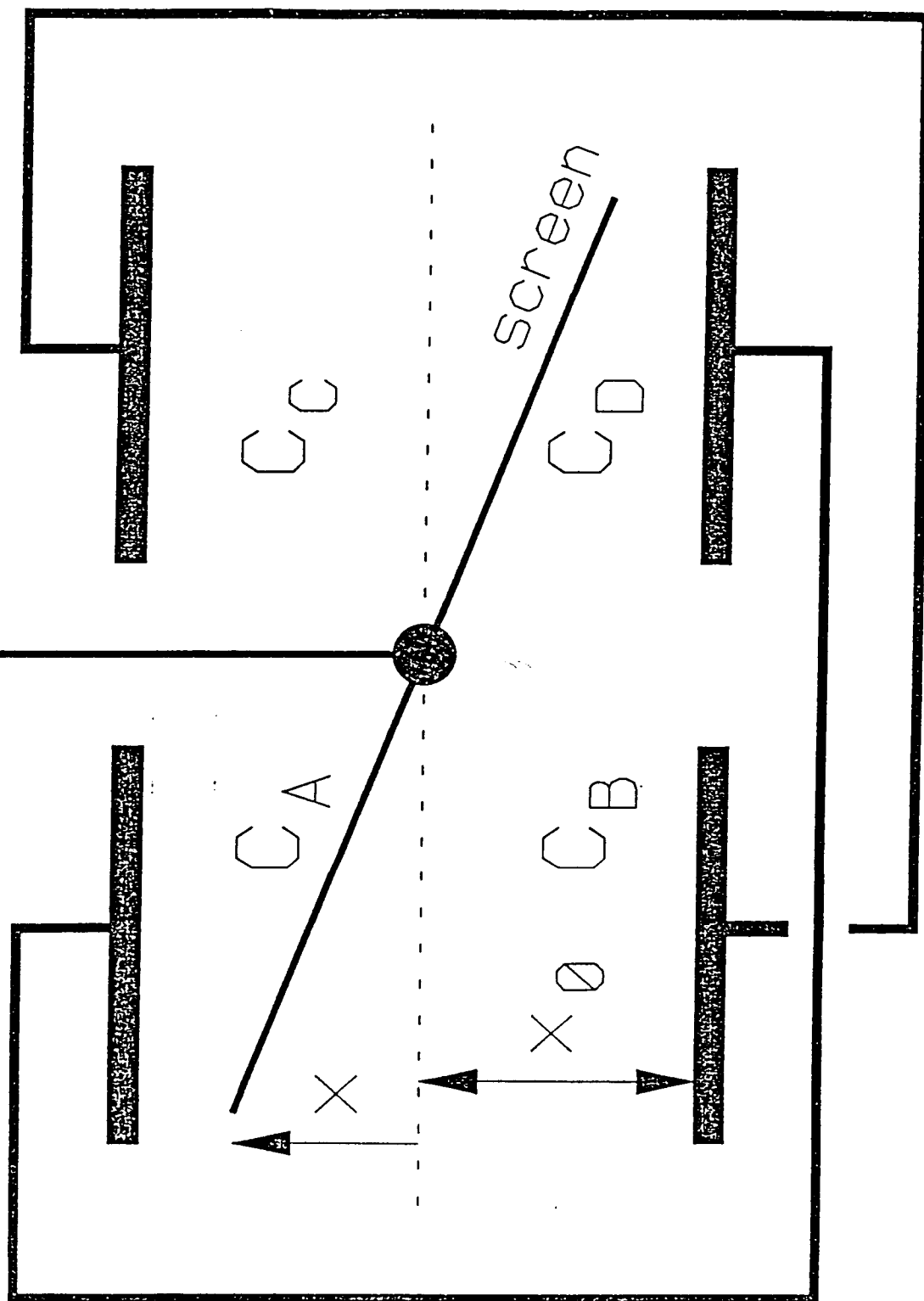


Start: 10 Hz  
Start: 10 Hz  
Frequency Response

Stop: 11.5625 Hz  
Stop: 11.5625 Hz  
RHS: 6



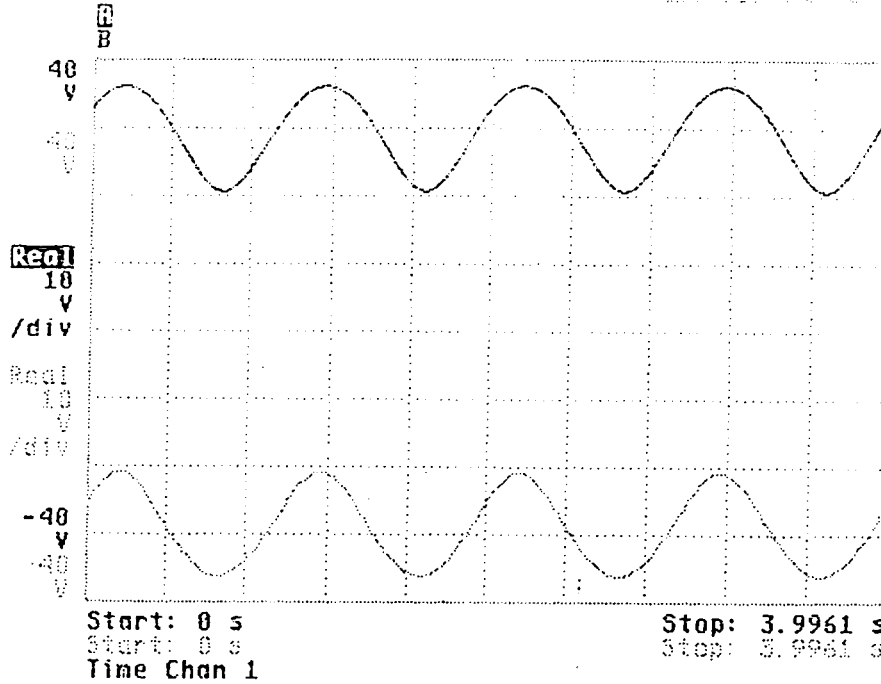
to lock-in



Status: ON  
 Type: FIXED SINE  
~~2-AVERAGE COMPLETE~~  
 PRIN:DUMP:SCR:\*WAI

Level: 800.8 mVrms  
 SinFq: 1 Hz

Src  
 Pmt Tlk Ltn Src

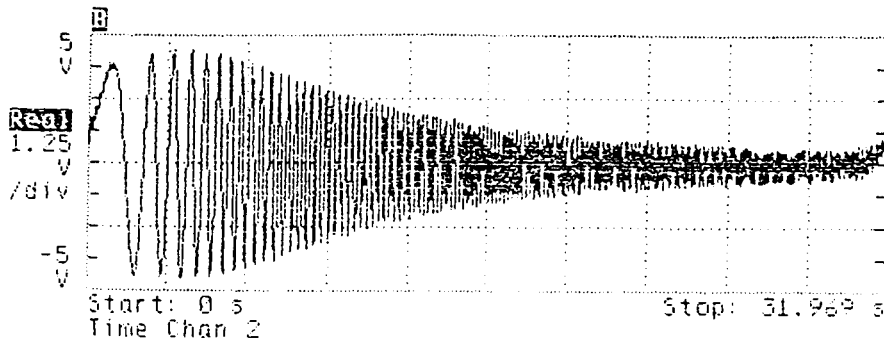
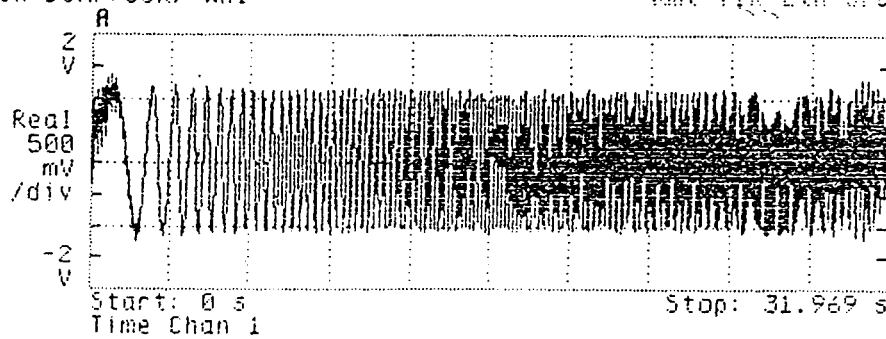


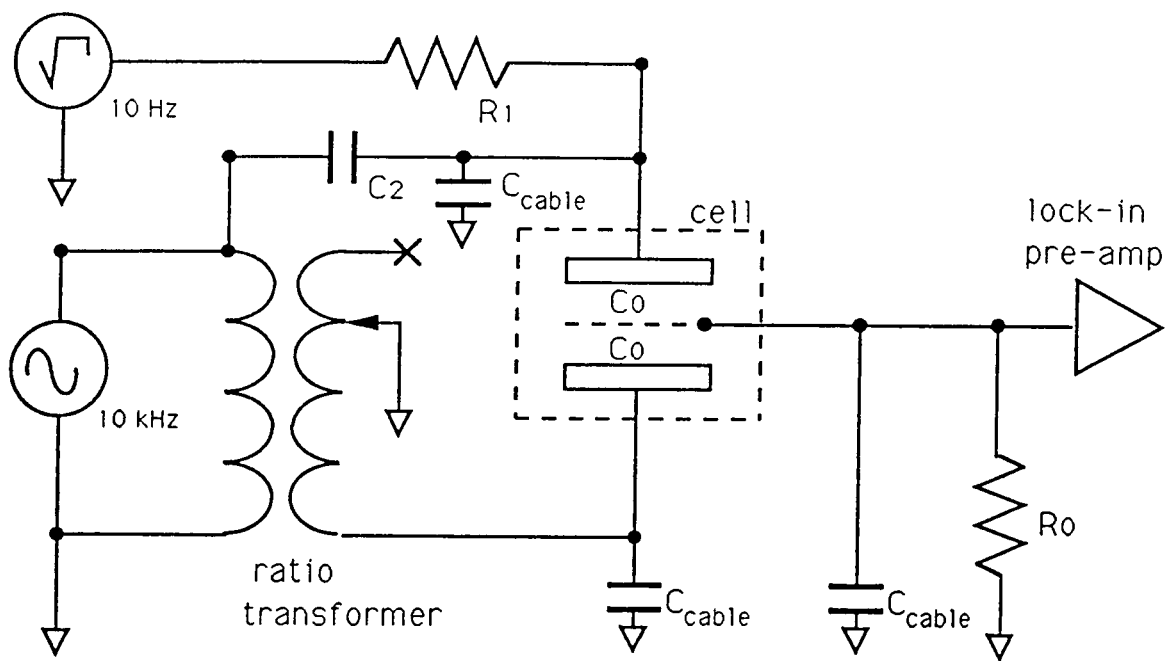
Ch1 Rng: 5 dBVrms  
 Ch2 Rng: 17 dBVrms  
~~2-AVERAGE COMPLETE~~  
 PRIN:DUMP:SCR:\*WAI

AC/DC: DC  
 AC/DC: DC

Flt/Gd: GROUND  
 Flt/Gd: GROUND

Src  
 Pmt Tlk Ltn Src



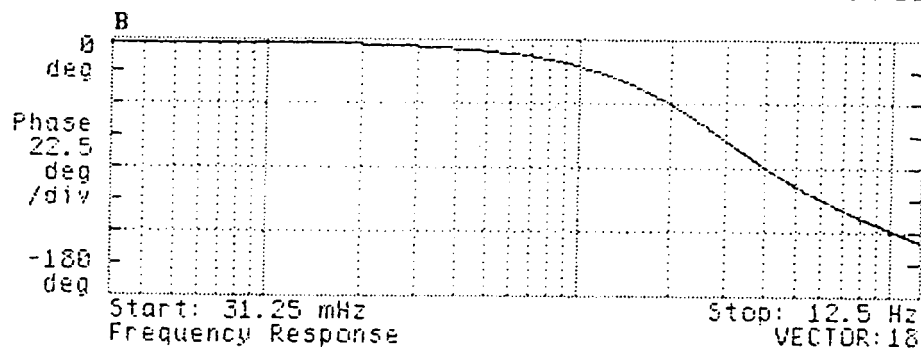
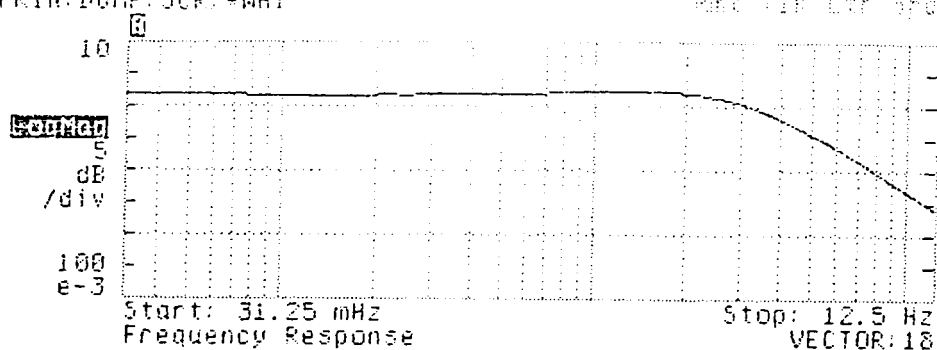


5

Status: ON  
 Type: PERIODIC CHIRP  
~~AVG: 10~~  
 PRIN: DUMP: SCR: \*WAI

Level: 1.6005 V  
 SinFro: 1 Hz

Src  
 Rmt Tlk Ltn Src

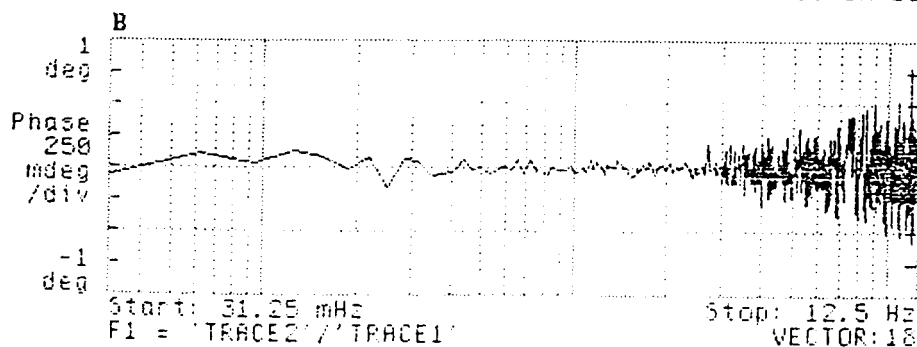
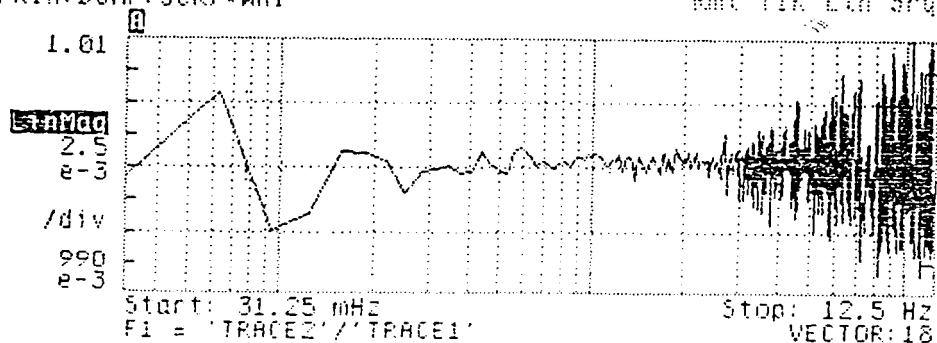


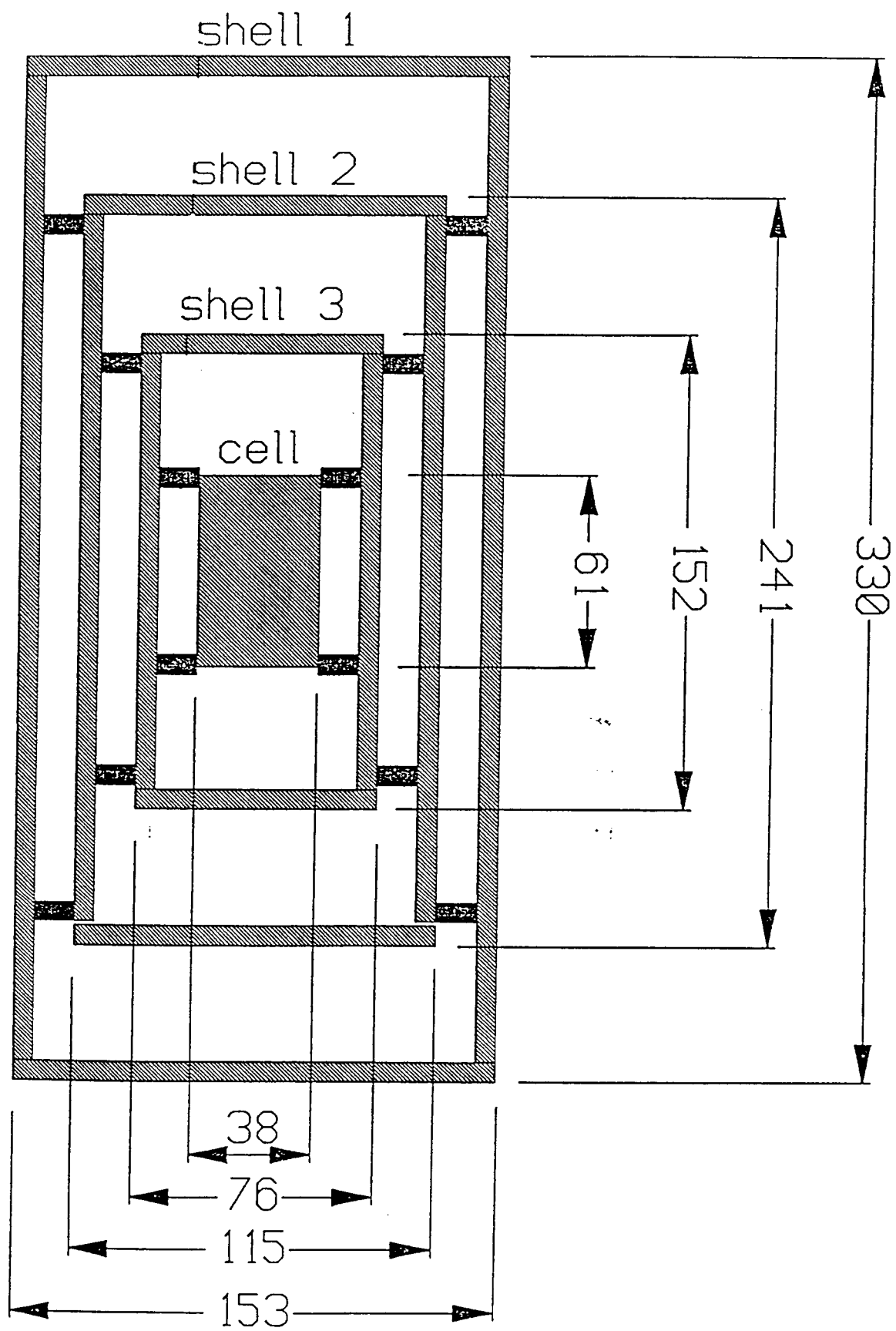
Ch1 Rng: 3 dBVrms  
 Ch2 Rng: 17 dBVrms  
~~AVG: 10~~  
 PRIN: DUMP: SCR: \*WAI

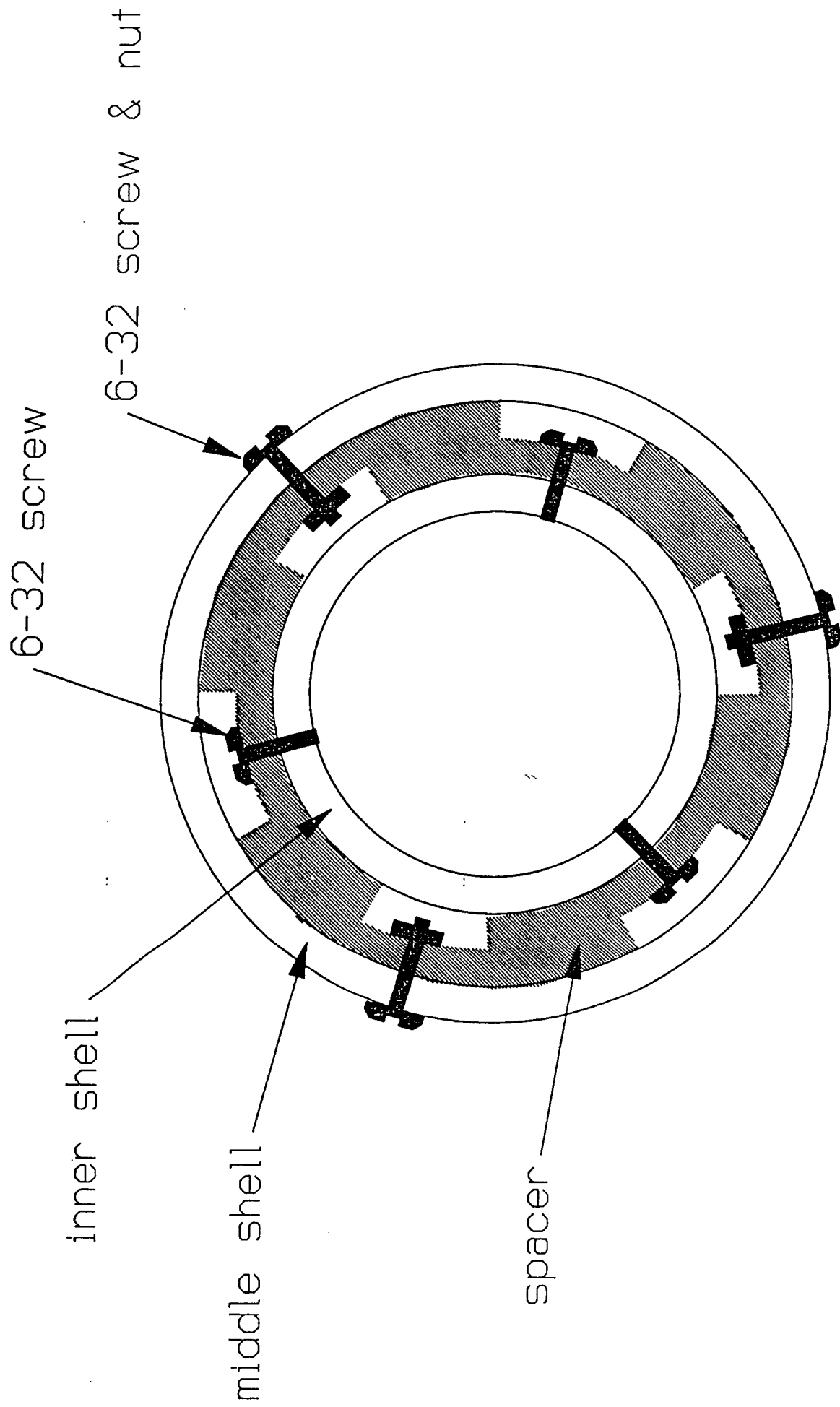
AC/DC: DC  
 AC/DC: DC

Flt/Gd: GROUND  
 Flt/Gd: GROUND

Src  
 Rmt Tlk Ltn Src

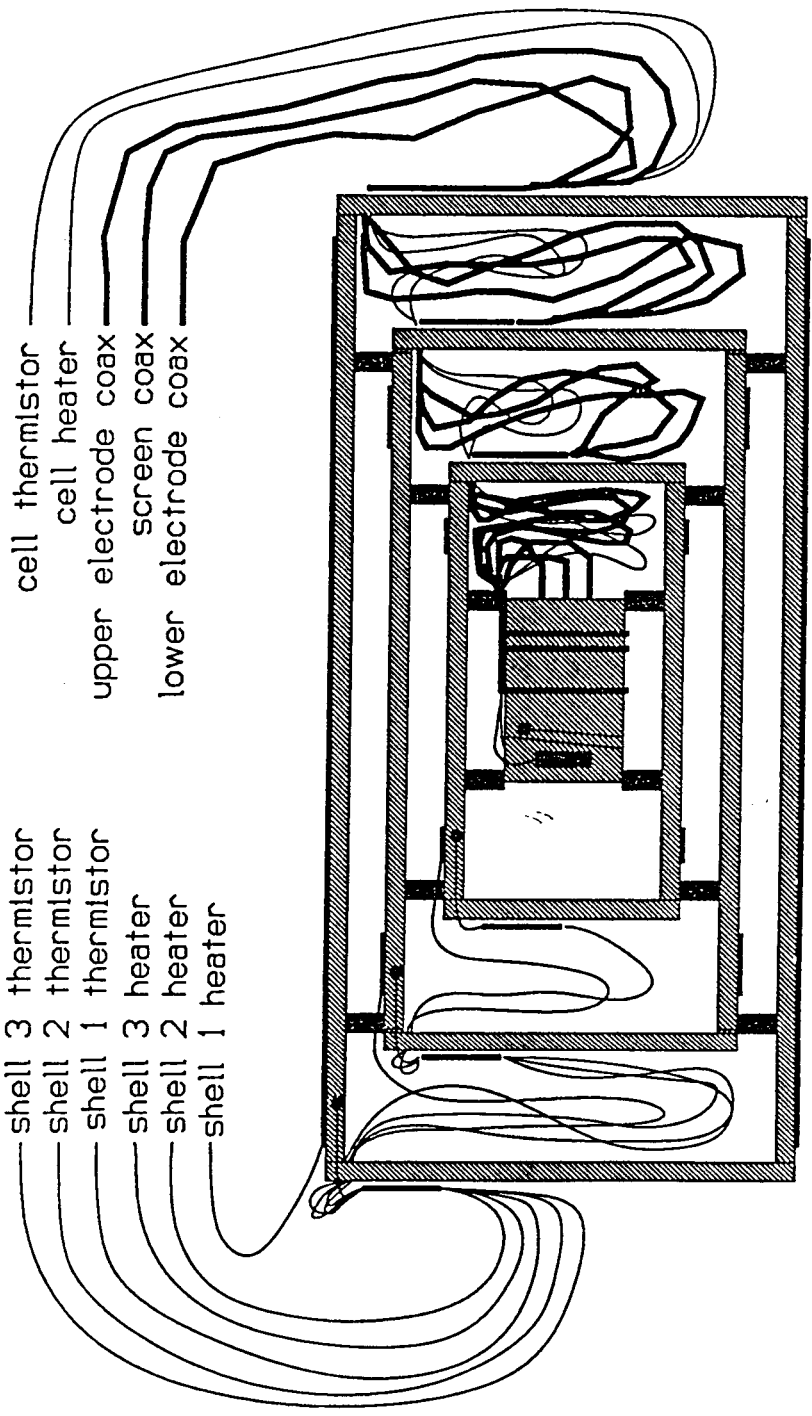


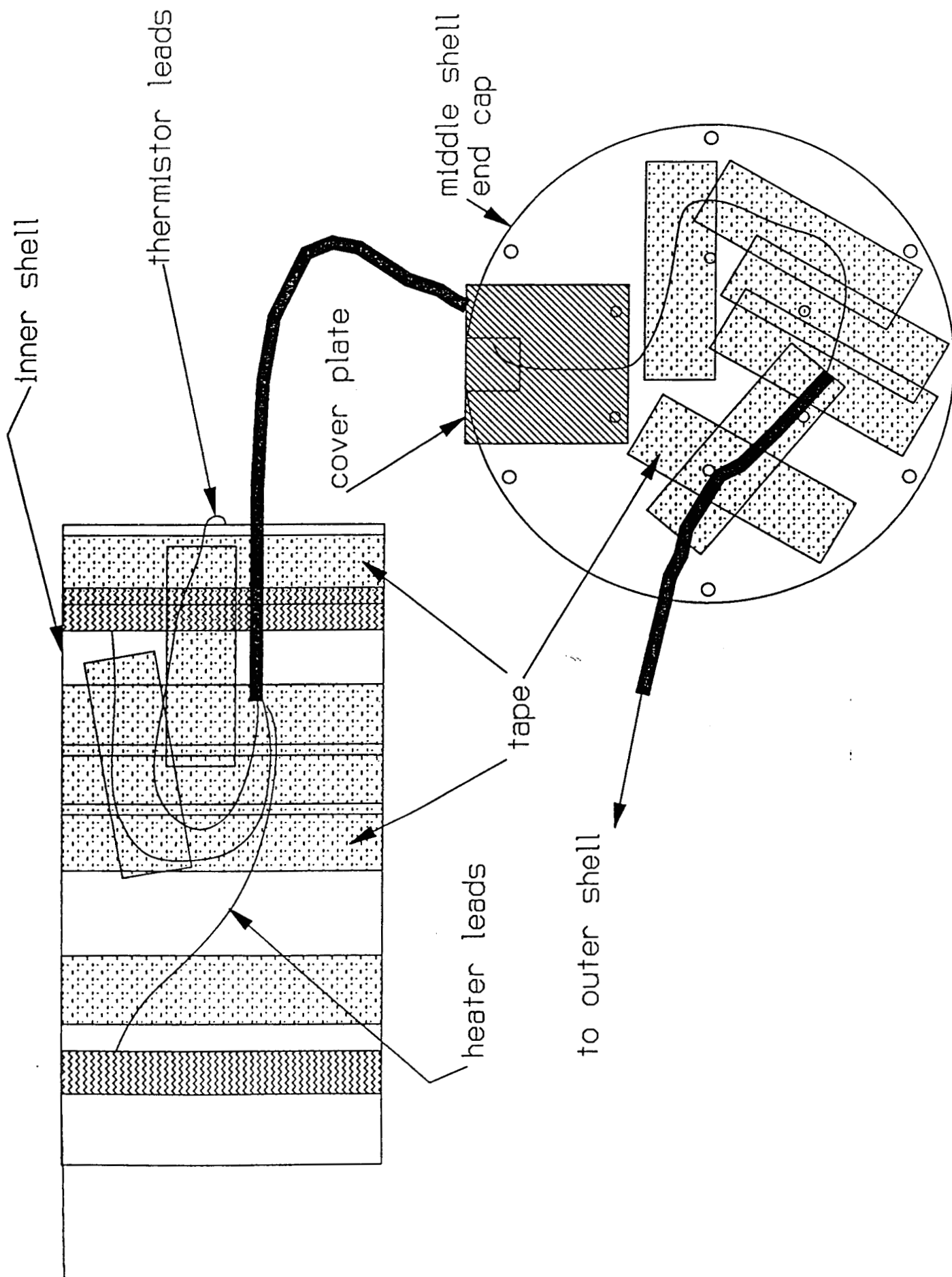




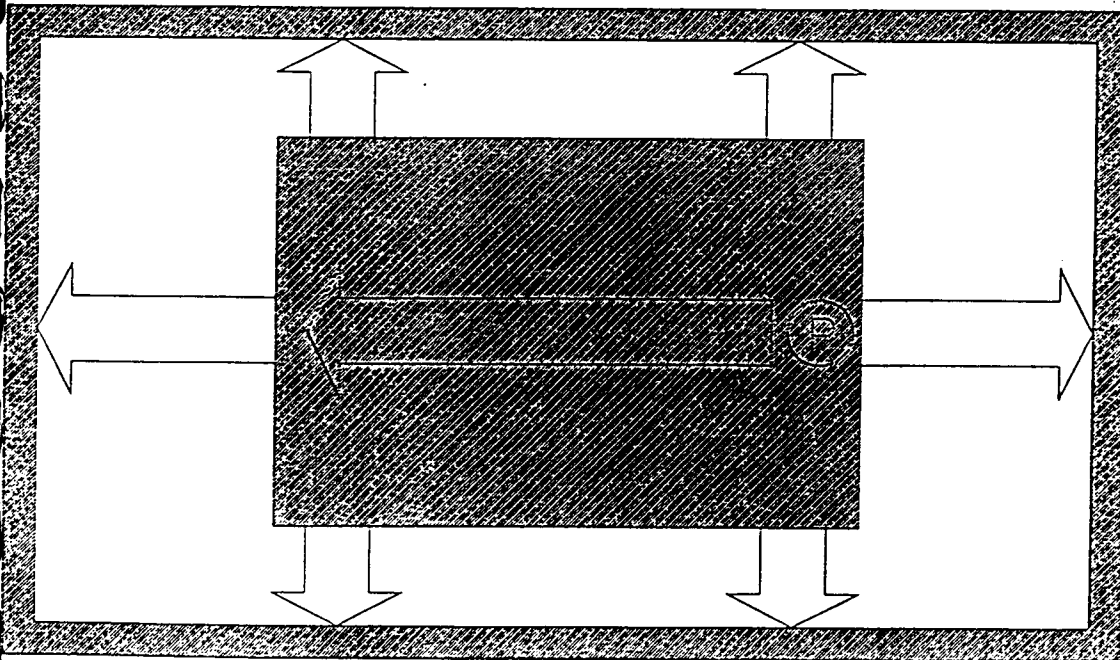
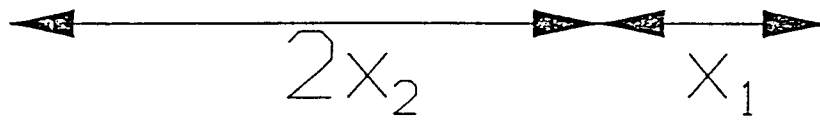
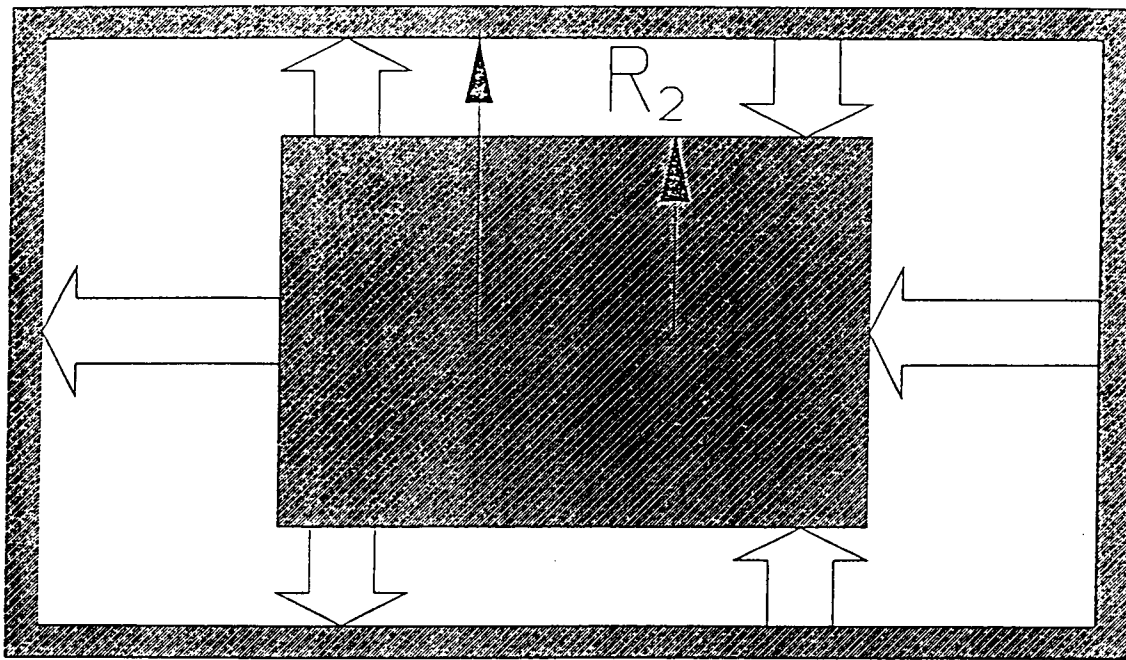
shell 3 thermistor  
 shell 2 thermistor  
 shell 1 thermistor  
 shell 3 heater  
 shell 2 heater  
 shell 1 heater

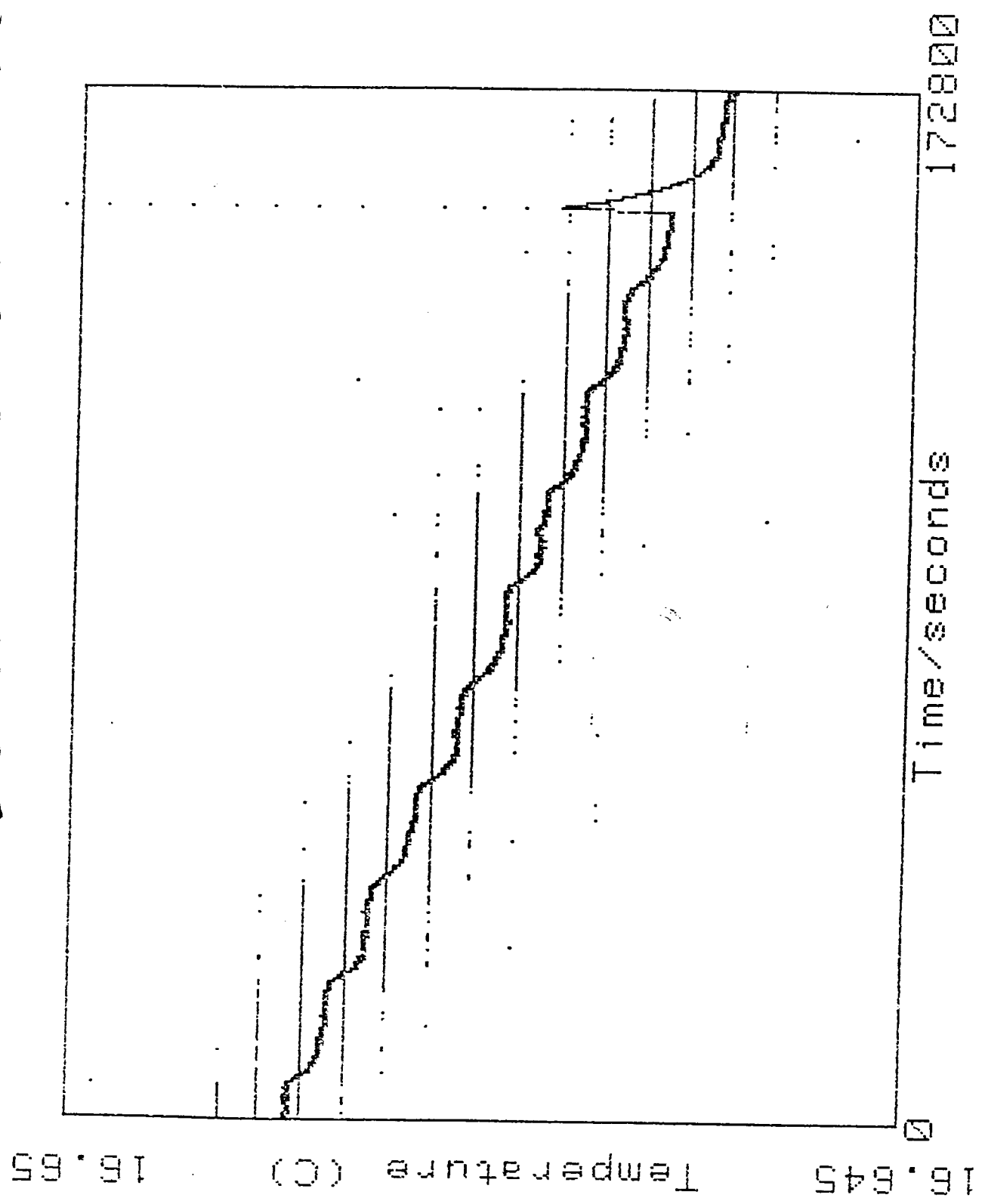
cell thermistor  
 cell heater  
 upper electrode coax  
 screen coax  
 lower electrode coax

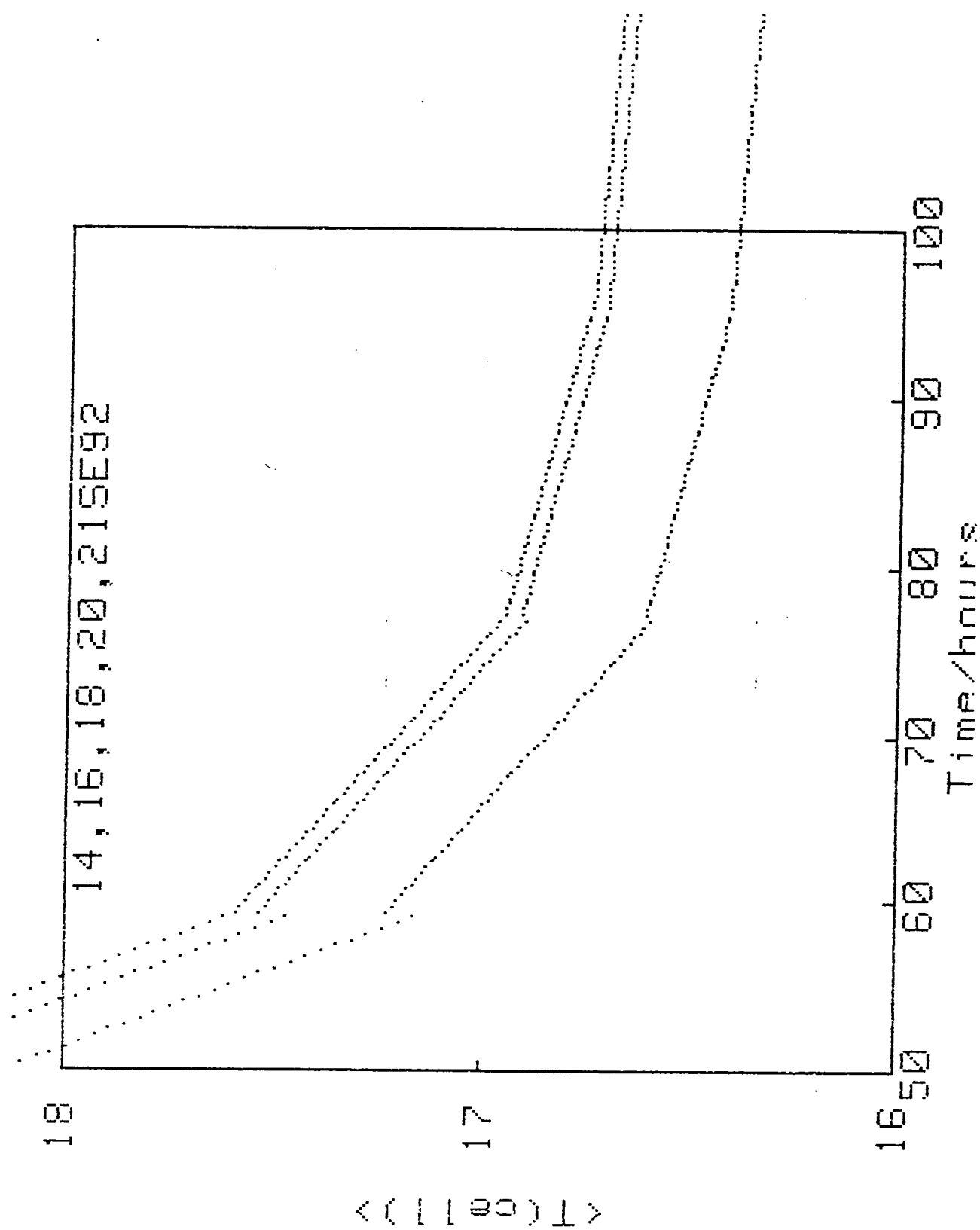




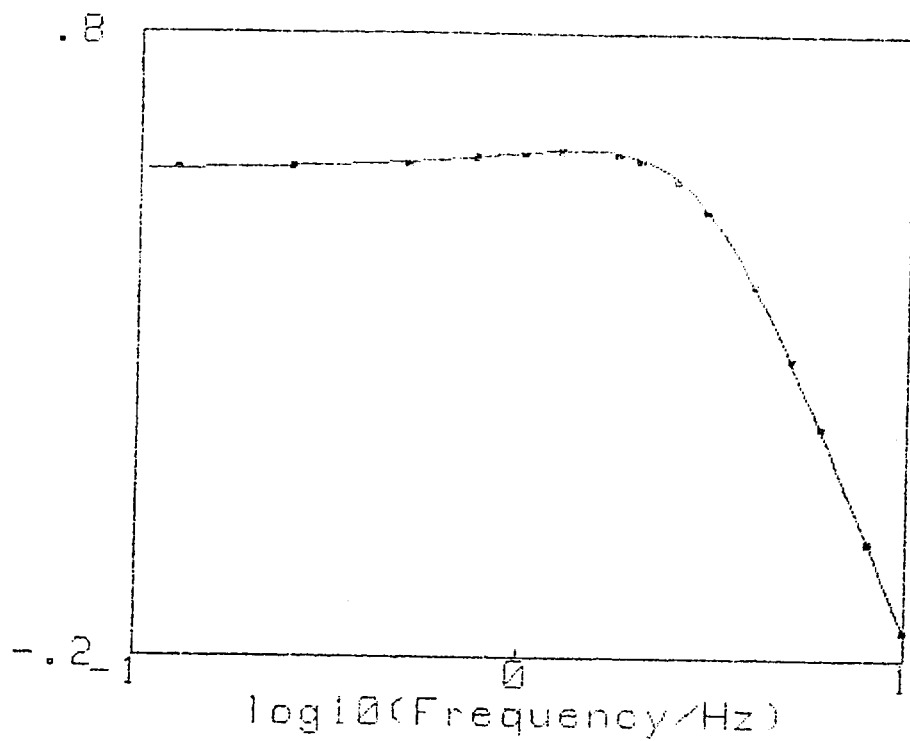
$R_1$



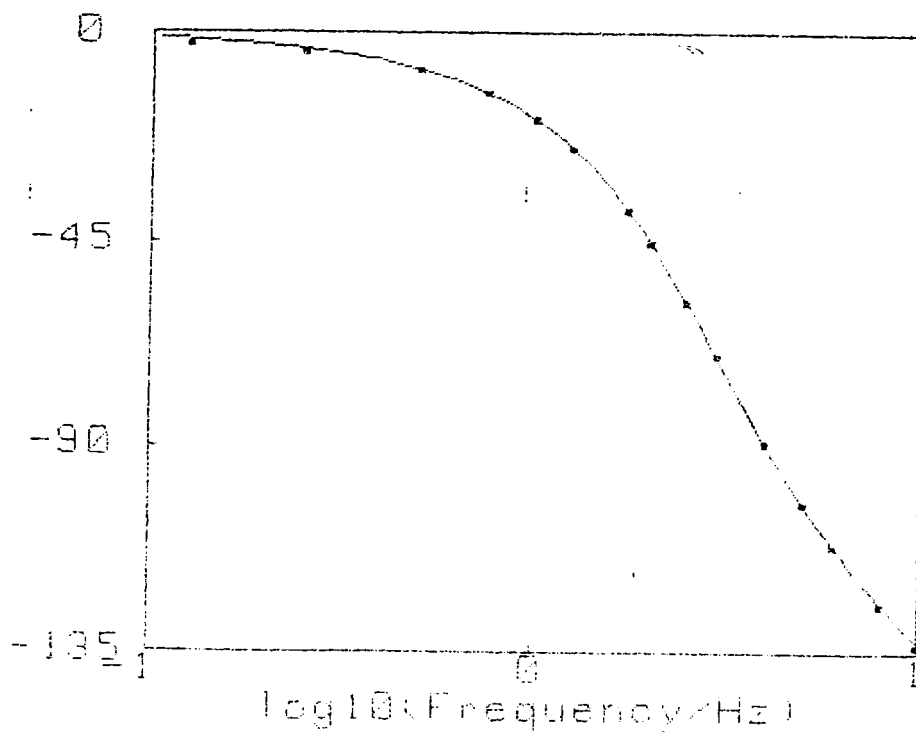




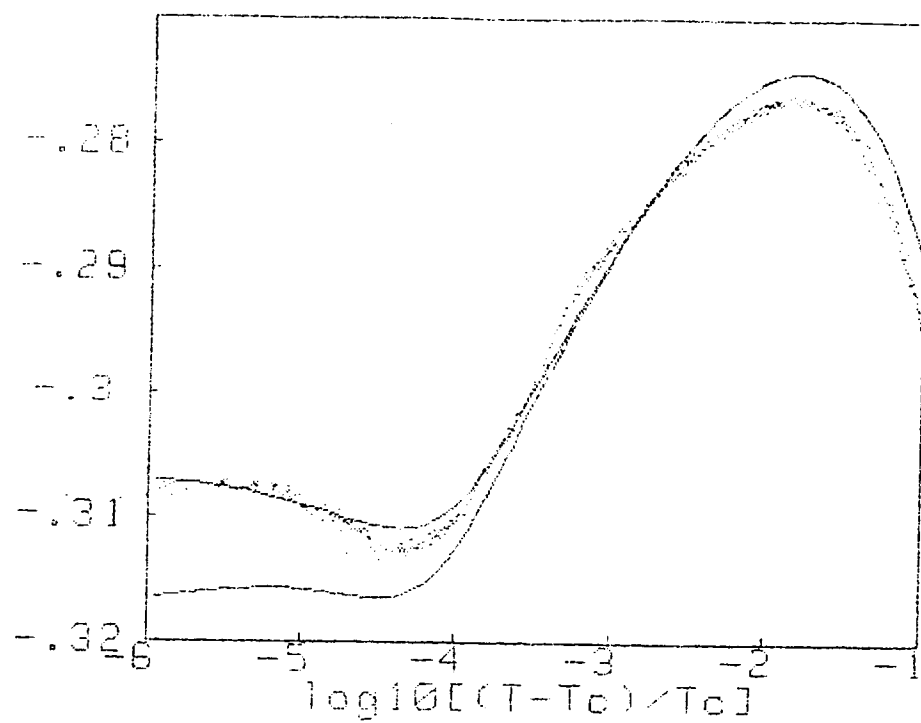
$\log_{10}[\text{ABS}(f.r.)]$



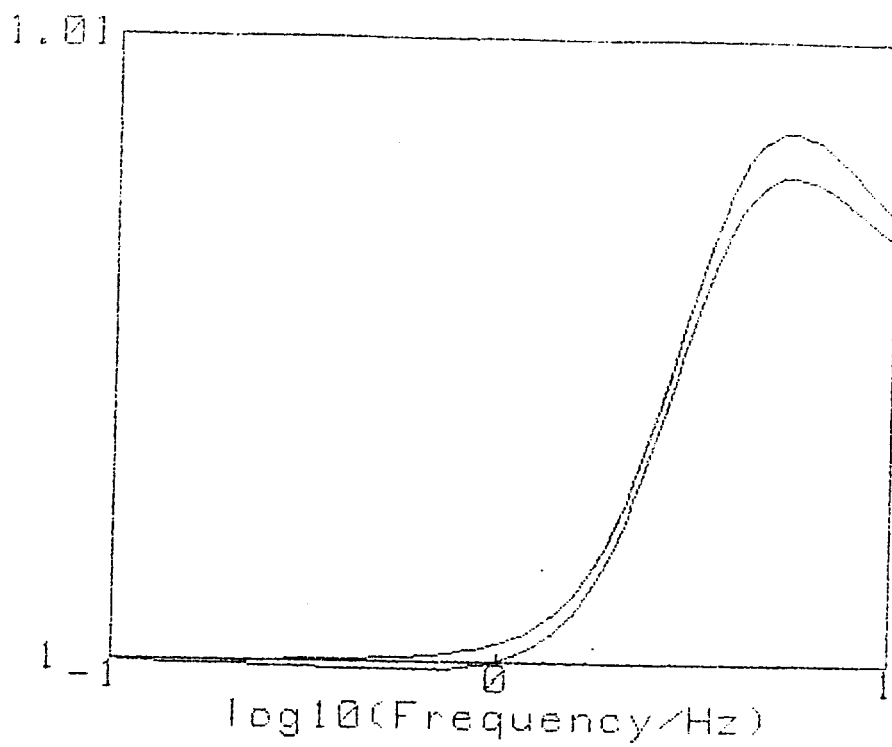
Phase / degrees

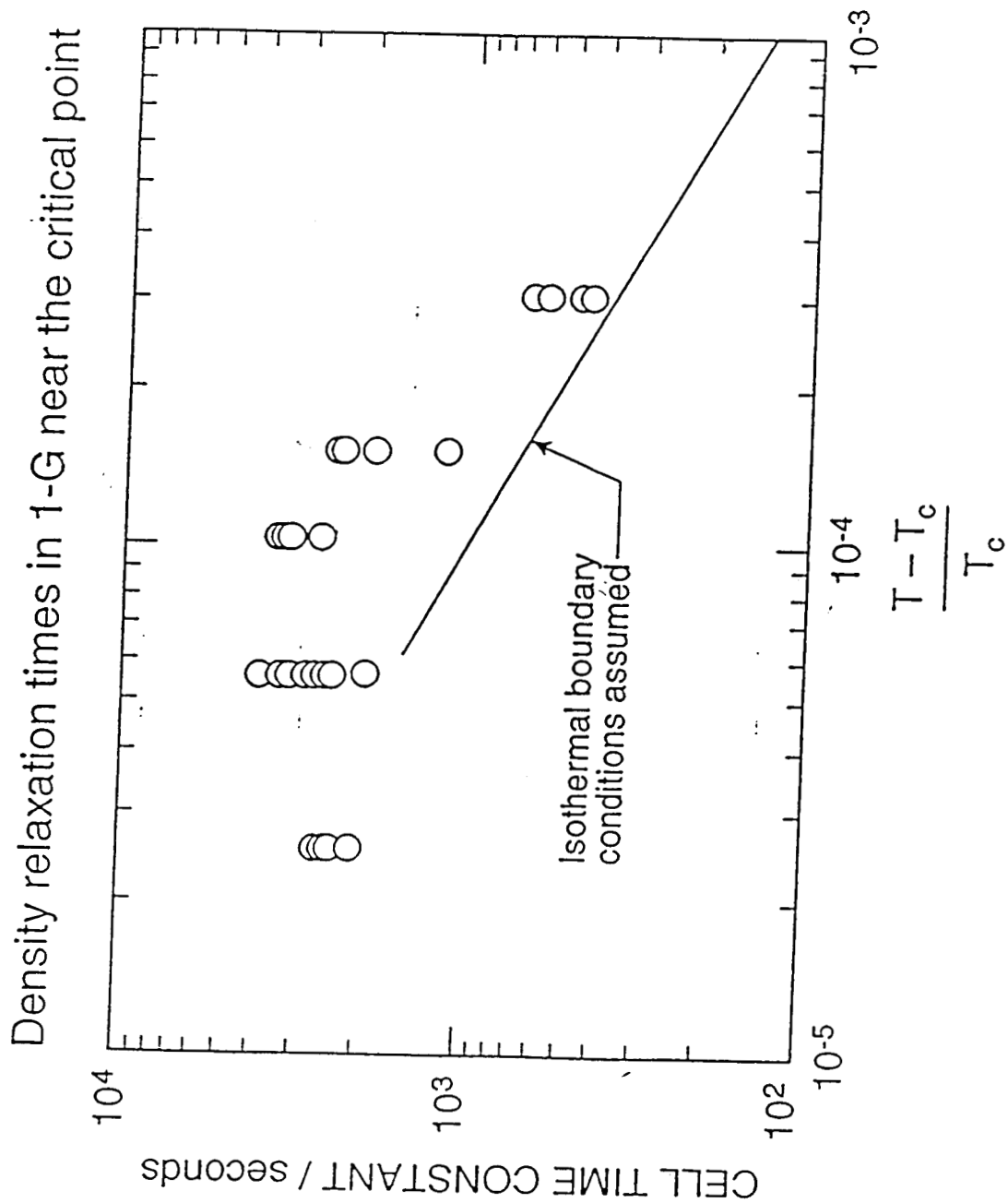


$\log_{10}[\text{ABS}(f.r.)]$



Change in f.r.





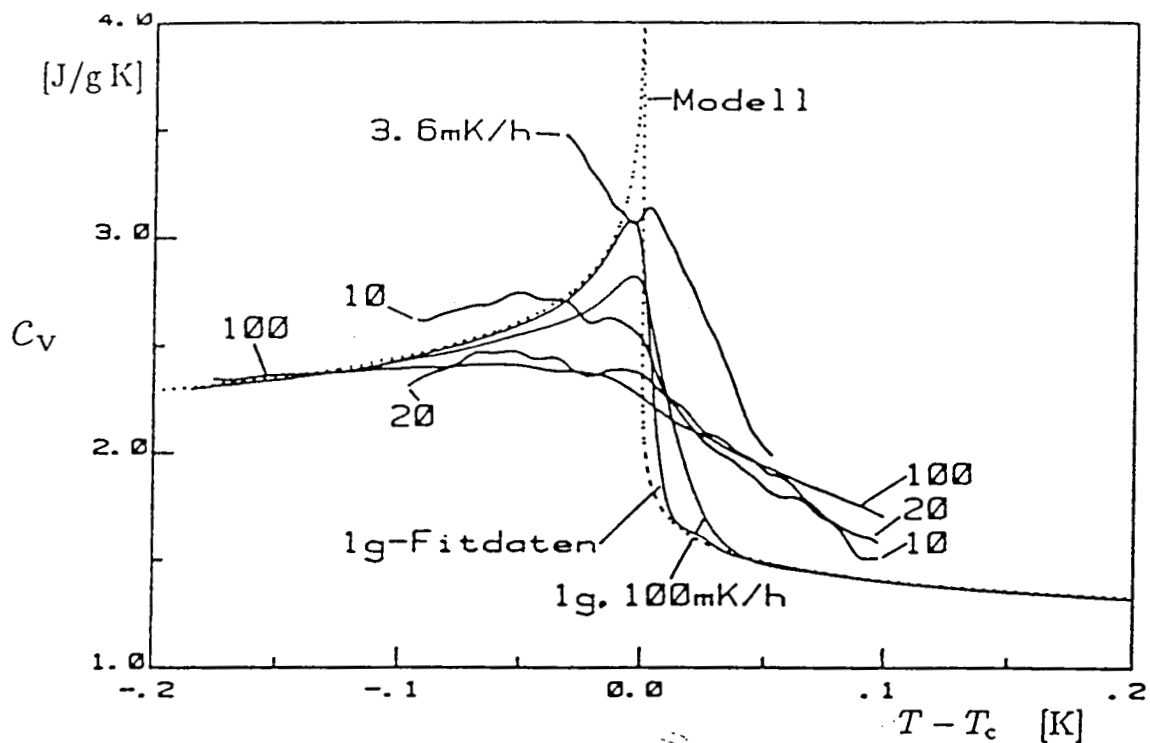
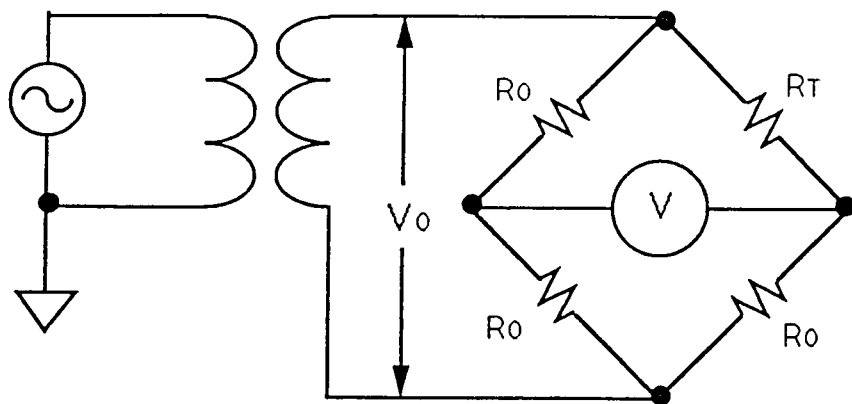
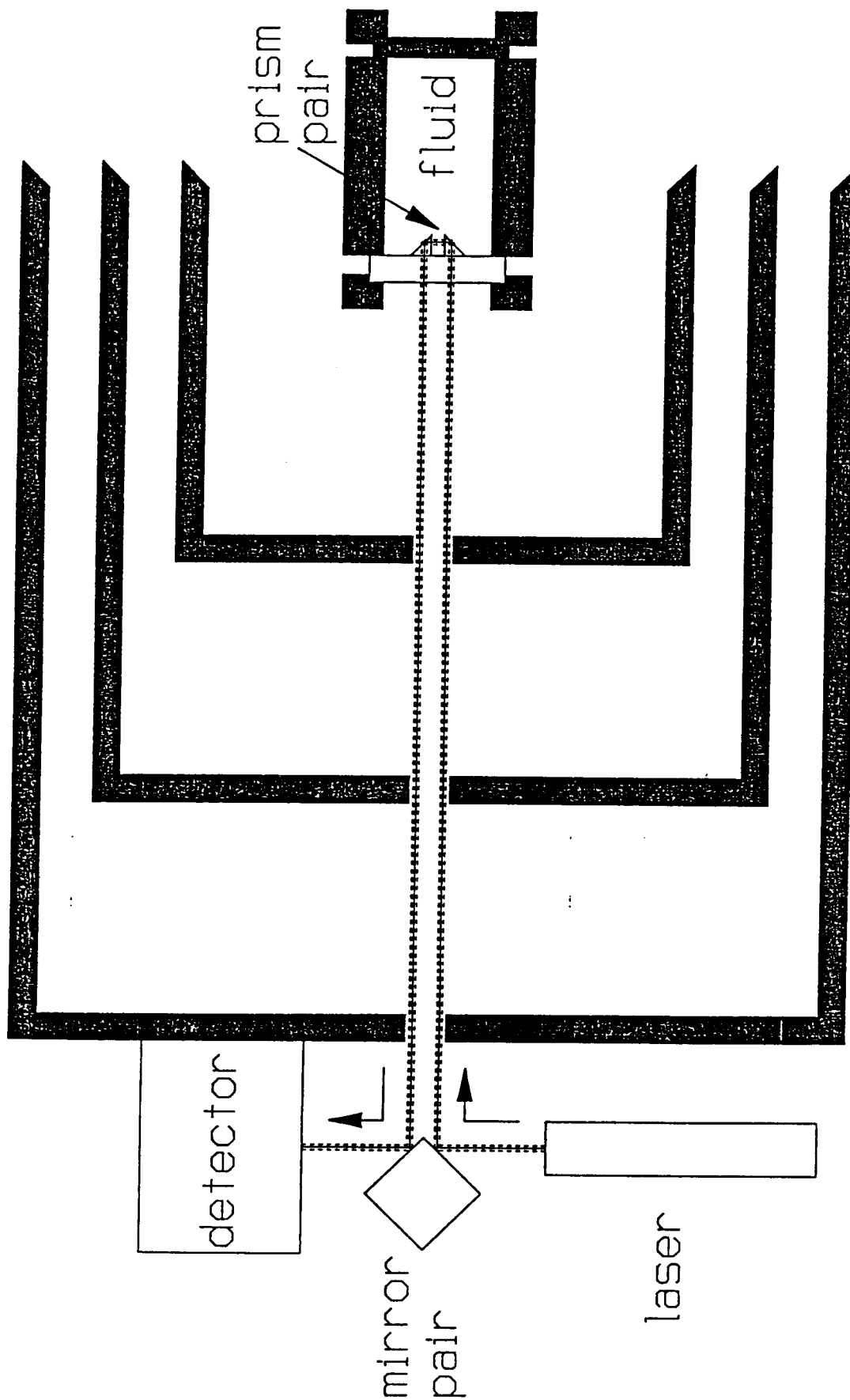


Bild 6.12: Die isochore Wärmekapazität  $c_v$  unter reduzierter Schwere für vier Temperaturgradienten und unter 1g Bedingungen.





## Scientific Objectives of the Critical Viscosity Experiment

R.F. Berg and M.R. Moldover

Thermophysics Division

National Institute of Standards and Technology

[14 December 1992]

### Summary

In microgravity, the Critical Viscosity Experiment will measure the viscosity of xenon 15 times closer to the critical point than is possible on earth. The results are expected to include the first direct observation of the predicted power-law divergence of viscosity in a pure fluid and they will test calculations of the value of the exponent associated with the divergence. The results, when combined with Zeno's decay-rate data, will strengthen the test of mode coupling theory. Without microgravity viscosity data, the Zeno test will require an extrapolation of existing 1-*g* viscosity data by as much as factor of 100 in reduced temperature. By necessity, the extrapolation would use an incompletely verified theory of viscosity crossover. With the microgravity viscosity data, the reliance on crossover models will be negligible allowing a more reliable extrapolation.

During the past year, new theoretical calculations for the viscosity exponent finally achieved consistency with the best experimental data for pure fluids. This report gives the justification for the proposed microgravity Critical Viscosity Experiment in this new context. This report also combines for the first time the best available light scattering data with our recent viscosity data to demonstrate the current status of tests of mode coupling theory.

### The Viscosity Divergence

This section outlines the theoretical context for the viscosity divergence near the critical point and explains the need, independent of any light scattering data, for its measurement in low gravity. During 1992, the theoretical estimate for the viscosity exponent  $y$  was raised from 0.032 to 0.041 [1], making it consistent with the best 1- $g$  viscosity measurements on pure fluids [2]. However, demonstrating this consistency requires the use of an interpolating "crossover" function, defined below, and an accounting for the complications due to density stratification of the test fluids in the Earth's gravitational field.

Near liquid-vapor and liquid-liquid critical points the most rigorous prediction, which comes from dynamic scaling theory, is that, in the asymptotic limit where critical fluctuations dominate the fluid's properties, the viscosity  $\eta$  will diverge as a power  $x_\eta$  of the correlation length  $\xi$ , namely

$$\eta \propto \xi^{-x_\eta} \propto (T - T_c)^{-y}. \quad (1)$$

Thus the temperature dependence of the viscosity is characterized by the exponent  $y \equiv \nu x_\eta$ . However, this asymptotic limit, in which the critical contribution to viscosity greatly exceeds the noncritical background contribution, occurs only within some tens of nanokelvin of the critical temperature  $T_c$ . Thus the asymptotic limit is experimentally unobservable.

The less rigorous mode coupling theory addresses the viscosity increase which is observable near  $T_c$  in terms of the noncritical viscosity  $\eta_0$  and a universal function  $H(\xi)$  [3] which describes the crossover between the purely noncritical and purely critical regions through the following ansatz:

$$\eta = \eta_0(\rho, T) \exp[x_\eta H(\xi)]. \quad (2)$$

There is no accurate theory for the noncritical viscosity  $\eta_0(\rho, T)$  for either pure fluids or binary liquid mixtures. However, for tests of theory, a simple pure fluid such as xenon has two advantages. First, the dependencies of  $\eta_0(\rho, T)$  on density  $\rho$  and temperature  $T$  are weak compared with the dependencies of  $\eta_0(x, T)$  on mole fraction  $x$  and temperature for binary liquids. For xenon, the temperature dependence is indistinguishable from the well-understood dilute gas behavior  $\eta_0(0, T)$ . The second advantage of pure fluids such as

xenon is the availability of the parameter  $q_C$  needed in the crossover function  $H(\xi)$ .  $H(\xi)$  depends on both density and temperature through the correlation length  $\xi$  and it incorporates two fluid-dependent wave vectors  $q_C$  and  $q_D$ . The wave vector  $q_C$  has not been determined for any binary liquids. The wave vector  $q_D$  represents the effective cutoff used in a mode coupling integral over momentum space. It is a free parameter related to the amplitude of the viscosity divergence, and it cannot be measured independently.

In effect,  $H(\xi)$  is an interpolation function chosen to have the correct limiting forms both near and far from the critical point. Although Sengers and co-workers have used  $H(\xi)$  in correlations of transport data [4],  $H(\xi)$  has not been tested for pure fluids in the region where  $\eta$  exhibits power-law behavior because that region is not accessible on earth.

As shown in Fig. 1, density stratification near the critical point of a 0.7 mm high sample of xenon limited the viscosity increase at reduced temperatures below  $\epsilon$  near  $3 \times 10^{-5}$ . Although the theory and parameters for the equilibrium stratification profile are well known, stratification complicates the hydrodynamics and obscures the critical enhancement. The power-law behavior in Eq. (1) that is expected at reduced temperatures less than  $1 \times 10^{-4}$  has never been observed in a pure fluid.

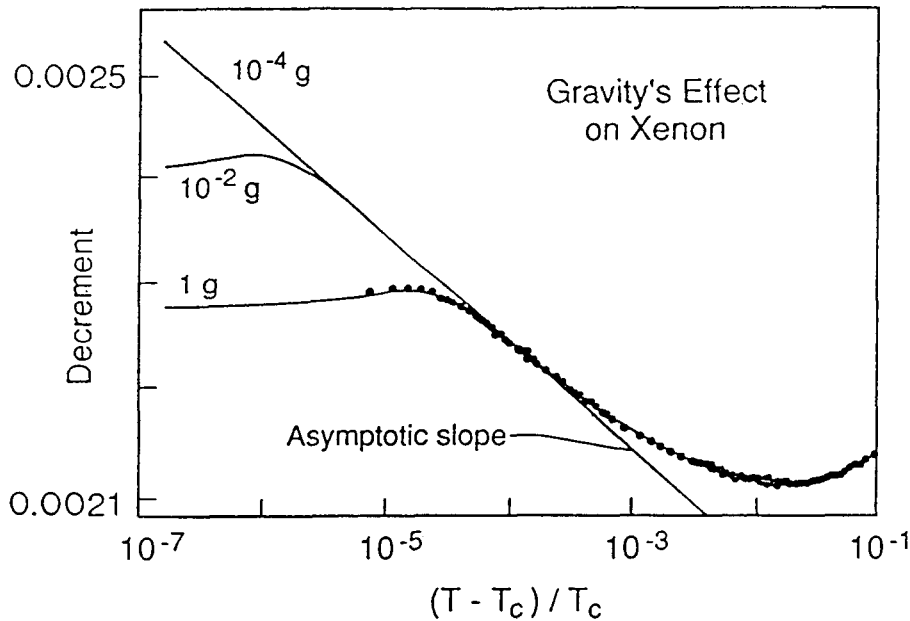


Fig. 1. Gravity's effect on viscosity measurements near the critical point of xenon. The curve labeled "1 g" is a fit to the decrement data obtained from a 0.7 mm high torsion oscillator [2]. (The decrement is approximately proportional to the square root of viscosity.) The two upper curves show the results expected if the measurement were repeated in reduced gravity. Because the asymptotic region is inaccessible in 1 g, the extrapolation of the viscosity towards  $T_c$  is sensitive to the theory of the crossover between the noncritical and critical regions.

The power-law behavior predicted by dynamic scaling and the theoretical value of the associated exponent  $x_\eta$  would be tested by an unambiguous observation of a divergence of the form of Eq. (1). However, as Fig. (1) shows, the crossover region appears to end at the same reduced temperature where significant gravity effects begin, at about  $\epsilon = 10^{-4}$ . Thus the best 1-g viscosity measurements can test only the combination of the theories for the exponent  $x_\eta$  and the crossover function  $H(\xi)$ .

Although our measurements on the pure fluids xenon and carbon dioxide are consistent with present crossover theory, for binary liquids, where the power-law divergence is directly observable, viscosity measurements are not consistent with crossover theory [5]. Should the additional xenon data from the flight experiment also prove inconsistent with crossover theory, the data would still be valid for the comparison with Zeno's light scattering data. Furthermore, there would then be a strong motivation to improve the theory for the viscosity divergence, perhaps at several levels. First, various approximations, though presently believed to be small, could be eliminated. These include neglect of the frequency dependence of viscosity, neglect of effects of the order of the inverse heat capacity ratio  $C_v/C_p$ , neglect of vertex corrections, assumption of Ornstein-Zernike correlations near  $T_c$ , and use of the same cutoff wave vector  $q_D$  for both viscosity and thermal conductivity. Second, although mode coupling theory predicts only a logarithmic divergence of viscosity, it has not been extended even enough to verify that the next term is consistent with an eventual power-law divergence. Such an extension would test the ansatz of Eq. (2).

To summarize, in microgravity the power-law divergence of viscosity could be directly observed in a pure fluid for the first time. Crossover theory, which agrees with 1-g pure fluid data, could also then be tested at a level presently available only for binary liquids, for which the current theory fails.

### Relationship Between Viscosity and Light Scattering

Mode coupling theory predicts a consistency relationship between viscosity data and dynamic light scattering data. Dynamic scaling and the main outline of mode coupling theory have been accepted as experimentally verified since the 1973 publication of Swinney and Henry [6], who found consistency to within 20 % for a variety of pure fluids, including xenon. Since then, the best improvement in precision was made by Burstyn et al. [7], who measured and compared against theory fluctuation decay rates in the binary liquid nitroethane + 3-methylpentane to within  $\pm 1$  %. A similar comparison using a pure fluid has not been achieved because of the inability to go close to  $T_c$  without encountering problems due to density stratification.

In what follows we use the best available light scattering and viscosity measurements for xenon to: (1) update testing of mode coupling in a pure fluid, (2) show present limits on light scattering measurements in 1-g, and (3) demonstrate the procedure that would be used for comparison of the improved data resulting from a flight experiment. These light scattering data were first obtained and used to test mode coupling by Güttinger and Cannell [8]. They used a xenon viscosity correlation based on the measurements of Strumpf et al. [9], which were limited by viscoelastic effects because the viscosity was measured at 39 kHz. We re-analyzed the Güttinger–Cannell decay rate data with the improved formalism of Burstyn et al. and our recent 1 Hz viscosity data. The present re-analysis demonstrates the consistency of mode coupling theory with the pure fluid and binary liquid mixture data (mentioned above) at large values of  $q\xi$ ; however, it does not remove the inconsistencies at small values of  $q\xi$ . Moreover, this test of mode coupling is not complete because of uncertainties in making background corrections far from  $T_c$  and the limitations imposed by gravitational stratification of the samples close to  $T_c$ .

The fundamental prediction of dynamic scaling is that a fluid's dynamic behavior is governed by the fluctuation decay rate  $\Gamma^c$ , which depends only on the wave vector  $q$  and the correlation length  $\xi$  according to

$$\Gamma^c = q^z f(x) , \quad (3)$$

where  $z$  is the dynamic scaling exponent and  $f(x)$  depends on  $\xi$  only through the dimensionless parameter  $x \equiv q\xi$ . Mode coupling gives explicit expressions for  $f(x)$ . For example, with various approximations, including neglect of the frequency and wave vector

dependence of viscosity, the critical contribution to the decay rate is

$$\Gamma^c = \frac{k_B T}{6\pi\eta\xi} \Omega_K(x), \quad (4)$$

where  $k_B$  is Boltzmann's constant and

$$\Omega_K(x) = \left[ \frac{3}{4x^2} \right] [1 + x^2 + (x^3 - x^{-1})\tan^{-1}(x)]. \quad (5)$$

In practice, the observed decay rate is assumed to be the sum

$$\Gamma = \Gamma^b + \Gamma^c \quad (6)$$

of a background contribution  $\Gamma^b$  and the critical contribution  $\Gamma^c$ . Although the ratio  $\Gamma^b/\Gamma^c$  is typically less than 10 % near  $T_c$ , it can be of order unity for pure fluids 3 K above  $T_c$ , thereby obscuring tests of mode coupling at small values of  $q\xi$ .

The most precise test of the mode coupling theory for the relationship between viscosity data and light scattering data was made by Burstyn, Sengers, Bhattacharjee, and Ferrell [7] in the binary liquid nitroethane + 3-methylpentane. Instead of numerically solving the coupled integral equations for viscosity and decay rate, they devised an analytic improvement to Eq. (4)

$$\Gamma^c = \frac{Rk_B T}{6\pi\eta\xi} \Omega_K(x) [1 + b^2 x^2]^{x\eta/2}, \quad (7)$$

with the additional universal parameters  $R$  and  $b$ . To compare their data to Eq. (7), they first subtracted the background  $\Gamma^b$ , which depends on the wave vector  $q_C$ . Although lack of an independent measurement forced them to estimate  $q_C$  heuristically, they excluded data where the background contributed more than 1 % to the total decay rate. Fig. (2a) shows their data, normalized according to

$$D^* \equiv \left[ \frac{6\pi\eta\xi}{k_B T} \right] \frac{\Gamma^c}{q^2} \quad (8)$$

Fig. (2b) shows that deviations from the universal function  $D^*$ , obtained with the free parameters

$$R = 1.01 \pm 0.04 \text{ and } b = 0.5 \pm 0.2 \text{ (binary liquid),} \quad (9)$$

are within  $\pm 1\%$ . The above error bars for  $R$  and  $b$  quoted by Burstyn et al. are very conservative, reflecting for example, the effects of a 20 % uncertainty in the viscosity exponent. The precision with which they determined  $R$  was approximately 0.1 %, although the scatter of the data that was averaged is on the order of  $\pm 1\%$ .

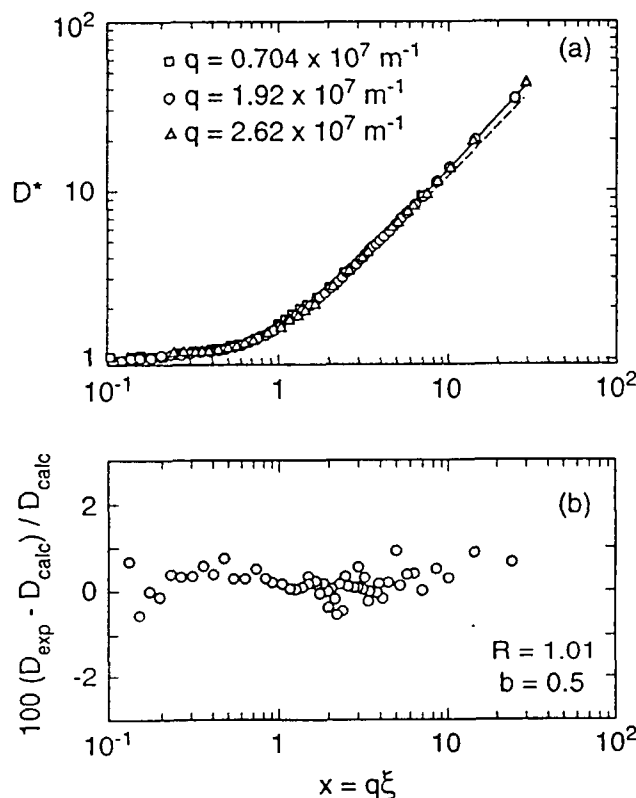


Fig. 2a. Fluctuation decay rate data obtained by Burstyn et al. [7] in the binary liquid nitroethane + 3-methylpentane. The data are plotted in the reduced form

$$D^* \equiv \frac{6\pi\eta\xi}{k_B T} \frac{(\Gamma - \Gamma^b)}{q^2}$$

to eliminate explicit dependence on the correlation length. The solid curve is Eq. (7) with  $R = 1.01$  and  $b = 0.5$ . The dashed curve results if  $b \equiv 0$ .

Fig. 2b. Deviations of the binary liquid data from Eq. (7) as a function of the dimensionless scaling parameter  $q\xi$ . The best fit values are  $R = 1.01$  and  $b = 0.5$ .

Pure fluids have not been tested to comparable accuracy. The best test so far published was made by Güttinger and Cannell [8] on xenon. In their publication,

Güttinger and Cannell used the same formalism and viscosity correlation used by Swinney and Henry [9]. Here we compare their data using both the improved scaling function devised by Burstyn et al., Eq. (7), and our recent viscosity data. Their data are shown in Fig. (3) and some details of our analysis are described in the Appendix.

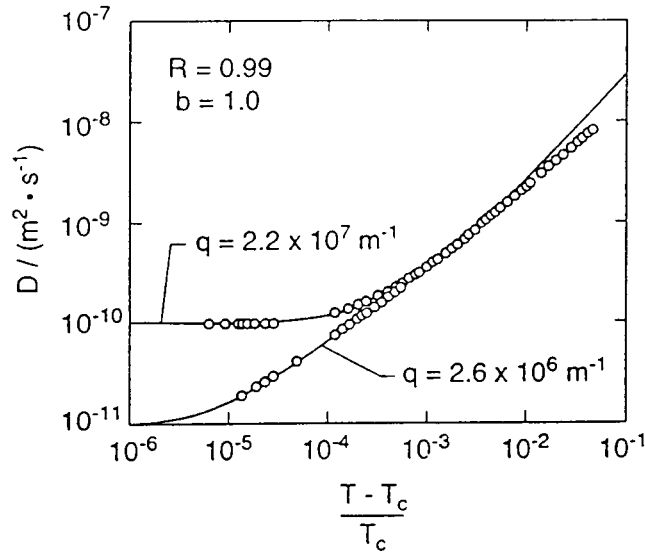


Fig. 3. Güttinger and Cannell's data for the diffusivity of xenon as a function of reduced temperature. The curves use both Eq. (7) with  $R = 0.99$  and  $b = 1.0$  and a background correction.

Fig. (4a) shows the normalized critical diffusion  $D^*$  for xenon. The large  $q$  data extend to  $q\xi = 7$  and the small  $q$  data extend only to  $q\xi = 0.6$ . In contrast, the binary liquid data of Fig. (2a) includes data from at least two values of  $q$  spanning the range  $0.2 < q\xi < 30$ . The data for xenon of Fig. (4b), calculated using the same binary liquid values  $R = 1.01$  and  $b = 0.5$ , deviate from Eq. (7) by 5–15 % at small values of  $q\xi$ . If the parameters  $R$  and  $b$  are assigned the values

$$R = 0.99 \quad \text{and} \quad b = 1.0 \quad (\text{pure fluid}), \quad (10)$$

the deviations at large  $q\xi$  are reduced to the experimental precision of  $\pm 2$  %, as shown in Fig. (4c). However, the inconsistencies for  $q\xi < 0.3$  become worse.

Although the parameter pairs Eqs. (9) and (10) differ, they lead to the same values of the asymptotic limit of Eq. (7). The limit is:

$$Rb^x \eta = (1.01)(0.5^{0.063}) \simeq (0.99)(1.0^{0.064}) \simeq 0.99. \quad (11)$$

Thus the limit is the same for the xenon data and the (nitroethane + 3-methylpentane) data. Consistency between these two data sets may approach 2 %, given the combined inaccuracies of the viscosities ( $\Delta\eta = 1.5$  % for nitroethane + 3-methylpentane [7] and  $\Delta\eta = 0.8$  % for xenon [2]). However, the inconsistencies are much larger at small values of  $q\xi$ . The apparent inconsistency between data obtained at different values of  $q$  may result from an inadequate theory for the background decay rate  $\Gamma^b$ .

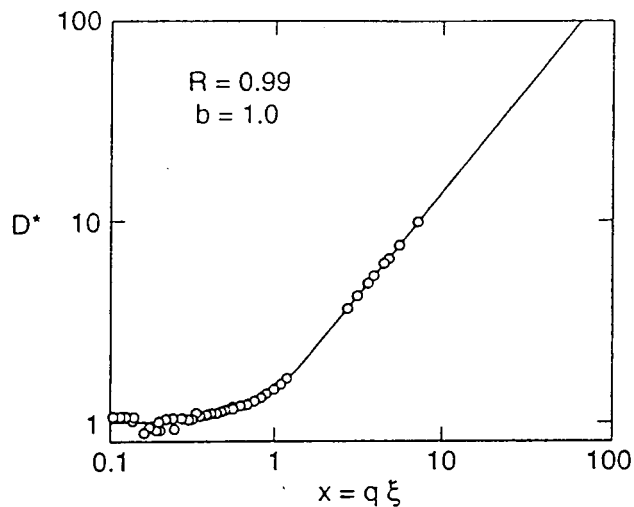


Fig. 4a. The xenon data of Fig. (3) scaled as in Fig. (2a) for the binary liquid. Density stratification limited the acquisition of small- $q$  data at large values of  $q\xi$ .

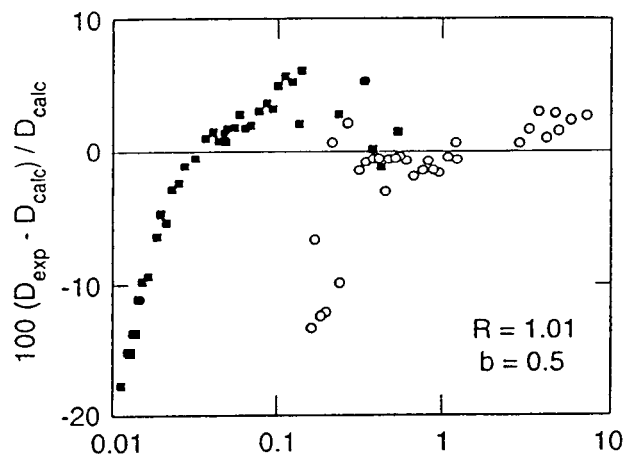


Fig. 4b. Deviations of the xenon data from Eq. (7) as a function of the dimensionless scaling parameter  $q\xi$ . The values of the parameters  $R$  and  $b$  are chosen to be the same as for the binary liquid nitroethane + 3-methylpentane.

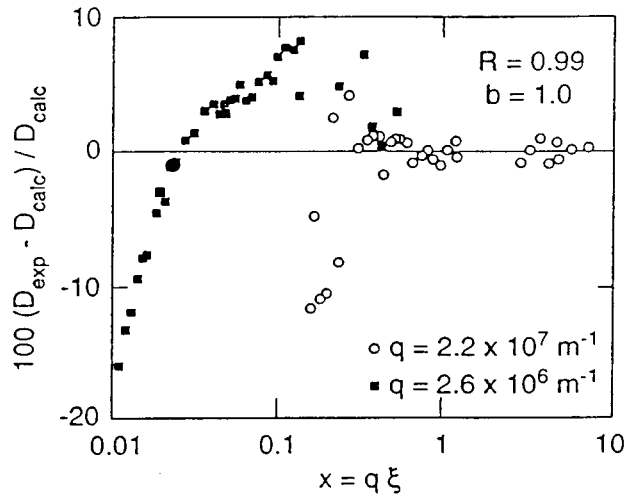


Fig. 4c. Deviations of the xenon data from Eq. (7) resulting from the values  $R = 0.99$  and  $b = 1.0$  chosen to minimize deviations at large  $q\xi$ . The inconsistencies seen in Fig. (4b) at small  $q\xi$  remain.

Improvements are needed in two places. First, for  $q\xi < 0.3$  (far from  $T_c$ ), the 5–15 % discrepancies in the xenon fluctuation decay rates, both between different values of  $q$  and between experiment and theory need to be resolved. The resolution will require either better theoretical characterization of the background decay rate  $\Gamma^b$ , or new data in this region (accessible in 1 *g*), or possibly both. New data at 1 *g* should be taken using Zeno techniques as soon as possible.

Second, new data at small  $q$  are needed at  $1 < q\xi < 30$ , where scaling theory predicts the  $q$ -dependence

$$\Gamma^c \sim q^z, \quad (12)$$

of the decay rate at large  $q\xi$ . Reduction of the uncertain background correction  $\Gamma^b$  requires measurements at small  $q$  (low angles). Achieving large  $q\xi$  then requires large  $\xi$ , which in turn requires temperatures close to  $T_c$ . Stratification problems prevented Güttinger and Cannell from approaching  $T_c$  closer than 3 mK to verify Eq. (12). Zeno will meet this need for the first time by obtaining data at  $12^\circ$  and  $168^\circ$  at  $\epsilon \geq 3 \times 10^{-7}$  (i.e. to within 0.1 mK of  $T_c$ ).

To summarize, mode coupling's predictions of fluctuation decay rates is incompletely tested in pure fluids. At small values of  $q\xi$  the discrepancies are 5–15 % and will require more ground-based work. At large values of  $q\xi$  verification of Eq. (12) must await the results of Zeno. In both regions, viscosity and light scattering data accurate to

about 1 % are needed to test mode coupling to an accuracy already achieved in the binary liquid nitroethane + 3-methylpentane. Although the available 1-*g* viscosity data can be extrapolated to  $\epsilon = 3 \times 10^{-7}$  with such precision, for the reasons stated in the previous section, the theoretical reliability of this extrapolation is unproven. New viscosity data obtained closer to  $T_c$  would eliminate this ambiguity and ensure the accuracy of comparisons of theory against Zeno's data.

#### Acknowledgements

We thank D.S. Cannell for useful comments and the data of Ref. 8. We thank R.W. Gammon, J. V. Sengers, and A. Wilkinson for providing helpful suggestions and for critically reading this report.

### Appendix

Testing of Eq. (7) requires three sets of data, each a function of reduced temperature. These are the correlation length, obtained from static light scattering measurements, the fluctuation decay rate, or inverse correlation time, obtained from dynamic light scattering measurements, and the viscosity. In the above comparison we relied on light scattering data provided by D.S. Cannell and on our own viscosity measurements.

For the correlation length measurements we used [8] the empirical formula:

$$\xi = (1.93 \times 10^{-10} \text{ m}) \epsilon^{-0.62} . \quad (13)$$

The exponent 0.62 differs slightly from the expected value  $\nu = 0.63$ . Presumably, the difference results from corrections to scaling. Equation (13) cannot be reliably extrapolated outside the measured range; however, our spot checks verified Eq. (13) accurately fits the data.

For the viscosity, we used the same crossover formalism and fit parameters used to describe our xenon viscosity data [2].

The fluctuation decay rate data, which have more scatter than the other two data sets, were used directly; they were not fitted by an empirical function.

We have already described the influence of the viscosity data on the interpretation of light scattering data close to  $T_c$  [2]. One consequence is that, in the limit of large  $q\xi$ , the critical diffusivity is

$$D_c = \left[ \frac{Rk_B T q}{16 \eta_0} \right] \left[ \frac{b q \xi_0}{Q_0 \xi_0} \right]^{y/\nu} , \quad (14)$$

The directly measured fluid-dependent parameters are the background viscosity  $\eta_0$ , the correlation length  $\xi_0$ , and the dimensionless product  $Q_0 \xi_0$ .

References

1. H. Hao, Dissertation, U. of Maryland (1992).
2. R.F. Berg and M.R. Moldover, J. Chem. Phys. 93, 1926 (1990).
3. J.K. Bhattacharjee, R.A. Ferrell, R.S. Basu, and J.V. Sengers, Phys. Rev. A 24, 1469 (1981).
4. V. Vesovic, W.A. Wakeham, G.A. Olchoway, J.V. Sengers, J.T.R. Watson, and J. Millat, J. Phys. Chem. Ref. Data, 19, 763 (1990).
5. J.V. Sengers, private communication (1992).
6. H.L. Swinney and D.L. Henry, Phys. Rev. A, 8, 2586 (1973).
7. H.C. Burstyn, J.V. Sengers, J.K. Bhattacharjee, and R.A. Ferrell, Phys. Rev. A 28, 1567 (1983).
8. H. Güttinger and D.S. Cannell, Phys. Rev. A 22, 285 (1980). D.S. Cannell, original data obtained by private communication.
9. H.J. Strumpf, A.F. Collings, and C.J. Pings, J. Chem. Phys. 60, 3109 (1974).

# TEMPERATURE GRADIENTS ON THE CELL WALL IN THE CRITICAL VISCOSITY EXPERIMENT

Robert F. Berg and Michael R. Moldover  
Thermophysics Division  
National Institute of Standards and Technology  
Gaithersburg, MD 20899

[1 February 1993]

Because of the diverging susceptibility  $\partial\rho/\partial T$  near the liquid-vapor critical point, temperature gradients must be kept small to maintain adequate sample homogeneity. In our Science Requirements Document we paid particular attention to radial density gradients caused by equilibration of the xenon sample. Axial density gradients were addressed through the requirement that the cell's copper wall have a gradient less than  $22\ \mu\text{K}/\text{m}$ . This report re-examines the cell wall's temperature distribution in more detail by estimating all known significant contributions to temperature differences on the cell's wall.

Although temperature homogeneity requirements have previously been given in terms of temperature gradients, this report will instead use temperature differences to generalize the discussion to include nonlinear temperature distributions. In equilibrium, a temperature difference  $\Delta T$  on the cell wall will induce a sample density difference  $\Delta\rho$  according to

$$\frac{\Delta\rho}{\rho_c} = \left[ \frac{T_c}{\rho_c} - \frac{\partial\rho}{\partial T} \right]_P \frac{\Delta T}{T_c} \quad (1)$$

$$= \left[ \frac{T_c}{P_c} - \frac{\partial P}{\partial T} \right]_{\rho_c} \Gamma \epsilon^{-\gamma} \frac{\Delta T}{T_c}. \quad (2)$$

Here  $\rho_c$ ,  $T_c$ , and  $P_c$  are the density, temperature, and pressure at the critical point and  $\Gamma$  and  $\gamma$  are the amplitude and exponent of the reduced susceptibility. The maximum temperature difference allowed at the planned closest reduced temperature of  $\epsilon = 2 \times 10^{-6}$  is thus

$$\Delta T = \frac{\Delta\rho}{\rho_c} \left[ \frac{T_c}{P_c} - \frac{\partial P}{\partial T} \right]_{\rho_c}^{-1} \frac{\epsilon^\gamma T_c}{\Gamma}, \quad (3)$$

or

$$\Delta T = (0.003)[6.0]^{-1} \frac{(2 \times 10^{-6})^{1.24} (290\ \text{K})}{(0.058)} = 0.21\ \mu\text{K}.$$

(This is equivalent to the specification of  $22\ \mu\text{K}/\text{m}$  along the oscillating screen's radius of  $0.010\ \text{m}$ . At larger reduced temperatures this requirement is less stringent. Therefore, in the following sections, where we estimate possible sources of temperature differences, we address only the case where the thermostat temperature is nearest  $T_c$  and is ramping at

the slowest planned rate.

### Thermistor dissipation

The gradient caused by the sample cell's thermistor power  $P$  is largest near the thermistor. The temperature field of the cell's wall can be estimated by imagining the cell to be slit along its length and unrolled into a plate of thickness  $d$ , length  $2x_2$ , and width  $2\pi R_2$ . Treating this plate as an infinite two-dimensional sheet gives the temperature at a distance  $r$  from the thermistor as approximately

$$\Delta T_{\text{therm}} = T(d) - T(r) \cong -\frac{P}{2\pi d \lambda_{\text{Cu}}} \ln(r/d), \quad (4)$$

where  $\lambda_{\text{Cu}}$  is the thermal conductivity of copper. Substituting the half length  $x_2$  of the cell for  $r$  yields the maximum temperature difference of

$$\Delta T_{\text{therm}} = \frac{(5 \times 10^{-7} \text{ W})}{(2\pi)(0.006 \text{ m})(400 \text{ W/(m} \cdot \text{K)})} \ln(0.03 \text{ m}/0.006 \text{ m}) = 0.05 \text{ } \mu\text{K}.$$

### Heat flow out of the copper body due to the cell's ramp rate

As the cell cools at the slowest ramp of  $\dot{T} = 3 \times 10^{-8} \text{ K/s}$ , the associated heat flow is about  $6 \text{ } \mu\text{W}$ , much more than the thermistor's power. If all of the heat is assumed to flow through two identical spacers located at the ends of the cell the temperature difference between the middle and the ends of the copper cell is

$$\Delta T_{\text{body}} = T(\text{middle}) - T(\text{end}) = -\frac{x_2^2 \dot{T}}{2 D_{T,\text{Cu}}} \quad (5)$$

where  $D_{T,\text{Cu}}$  is the thermal diffusivity of copper. The result is

$$\Delta T_{\text{body}} = \frac{(0.030 \text{ m})^2 (3 \times 10^{-8} \text{ K/s})}{(2)(1.16 \times 10^{-4} \text{ m}^2/\text{s})} = 0.12 \text{ } \mu\text{K}.$$

This estimate would be reduced by including the effects of air conduction and infrared radiation to the inner shell, and it would be increased by spacer asymmetry, considered below.

Symmetric conduction of the cell's two spacers, located at each end, can be encouraged but not guaranteed by identical construction. The relative contributions of the left and right spacers also depend on the details of the clamping of the spacers to the cell and to the inner shell. If we model this asymmetry as an air gap of length  $\Delta R_{\text{air}}$  in series with the spacer length  $\Delta R_{\text{spacer}}$ , then reasonable machining tolerances (0.005 inch) place an upper bound on the asymmetry  $\Delta \kappa$  of

$$\Delta \kappa = \left[ -\frac{\lambda_{\text{plastic}}}{\lambda_{\text{air}}} \right] \left[ -\frac{\Delta R_{\text{air}}}{\Delta R_{\text{spacer}}} \right]. \quad (6)$$

$$\Delta\kappa = \left[ \frac{0.2}{0.023} \frac{\text{W}/(\text{m}\cdot\text{K})}{\text{W}/(\text{m}\cdot\text{K})} \right] \left[ \frac{0.00013}{0.013} \frac{\text{m}}{\text{m}} \right] = 0.09$$

In practice, the air gaps will be significantly reduced by slight deformation of the spacer when the the plastic and metal surfaces are clamped together.

Including spacer asymmetry in the model leads to the following dependence of the cell temperature on axial position  $x$ .

$$T(x,t) = T\{[t + (2D_{T,Cu})^{-1}[(2x_2\Delta\kappa)x + x^2]]\} \quad (7)$$

The maximum temperature difference is then

$$\Delta T_{\text{body}} = \frac{T x_2^2}{2D_{T,Cu}} [1 + 2\Delta\kappa + \Delta\kappa^2], \quad (8)$$

leading to the estimate

$$\Delta T_{\text{body}} = \frac{(3 \times 10^{-8} \text{ K/s})(0.03 \text{ m})^2}{(2)(1.16 \times 10^{-4} \text{ m}^2/\text{s})} [1.19] = 0.14 \mu\text{K}.$$

In the 1992 Science Requirements Document, the cell's two spacers were estimated to contribute 0.031 W/K out of a total of 0.065 W/K conductivity between the cell and the inner shell. Thus the estimate above should be reduced by a factor of about two to

$$\Delta T_{\text{body}} = 0.07 \mu\text{K}.$$

#### Heat flow out the sapphire window due to the cell's ramp rate

The heat flow out of the sapphire window gives a radial temperature difference of

$$\Delta T_{\text{window}} = \frac{R_w^2}{4} \frac{T}{D_{T,\text{sapphire}}}, \quad (9)$$

where  $R_w$  is the window's radius and  $D_{T,\text{sapphire}}$  is the thermal diffusivity of sapphire, the window material. The result is

$$\Delta T_{\text{window}} = \frac{(0.013 \text{ m})^2 (3 \times 10^{-8} \text{ K/s})}{(4)(1.34 \times 10^{-5} \text{ m}^2/\text{s})} = 0.09 \mu\text{K},$$

Including the effects of radiation and air conduction would reduce this temperature difference.

#### Inner shell gradient

The temperature gradient on the inner shell is partially imposed on the cell. Here we estimate the gradient reduction ratio in two ways and combine the resulting values with an estimate of the inner shell's gradient to obtain the cell's gradient.

For the first estimate we assume that heat flows between the cell and the

surrounding inner shell through only the cell's spacers. The temperature difference on the cell is then approximately

$$\Delta T_{\text{gradient}} = T(\text{right}) - T(\text{left}) \cong \frac{dT_{\text{in}}}{dx} \frac{\kappa_{\text{sp}}}{\kappa_{\text{cell}}} 2x_2, \quad (10)$$

where  $2x_2$  is the cell's length,  $dT_{\text{in}}/dx$  is the inner shell's temperature gradient, and  $\kappa_{\text{sp}}$  and  $\kappa_{\text{cell}}$  are the radial conductance of the spacer and the axial conductance of the cell respectively. The conductivity of the cell along its length is

$$\kappa_{\text{cell}} = \frac{A_{\text{cell}} \lambda_{\text{Cu}}}{2x_2} = \frac{(3/4)(\pi)(0.019 \text{ m}^2)(400 \text{ W/K/m})}{(2)(0.030 \text{ m})} = 5.7 \text{ W/K},$$

where  $A_{\text{cell}}$  is the cell's metallic cross section area. The spacer conductivity was already estimated in the Science Requirements Document at 0.031 W/K.

For the second estimate we assume heat flows through only the radial air gap between the cell and the inner shell.

$$\Delta T_{\text{gradient}} = T(\text{right}) - T(\text{left}) \cong \frac{dT_{\text{in}}}{dx} \left[ \frac{x_2}{d_{\text{cell}}} \right]^2 x_2, \quad (11)$$

where  $d_{\text{cell}} = 0.74 \text{ m}$  is a length characterizing the cell's conductance to the surrounding inner shell (defined by Eq.(20), p.17 of the Science Requirements Document).

Now we estimate the inner shell's temperature gradient, due mainly to the heaters located at the ends. Assuming the right heater produces 10% more heat than the left heater, the inner shell's gradient is

$$\frac{dT_{\text{in}}}{dx} \cong (0.10) \frac{x_{2,\text{in}}}{d_{\text{in}}^2} (T_{\text{in}} - T_{\text{mid}}), \quad (12)$$

where  $x_{2,\text{in}}$  is the half-length of the inner shell,  $d_{\text{in}}$  is a length characterizing the inner shell's conductance to the surrounding middle shell, and  $(T_{\text{in}} - T_{\text{mid}})$  is the regulated temperature offset between the inner and middle shells. Eq.(12) yields

$$\frac{dT_{\text{in}}}{dx} = (0.10) \frac{(0.070 \text{ m})}{(0.82 \text{ m})^2} (0.030 \text{ K}) = 3.1 \times 10^{-4} \text{ K/m}.$$

Using the above results in Eq.(10) gives

$$\Delta T_{\text{gradient}} \cong (3 \times 10^{-4} \text{ K/m}) \frac{(0.031 \text{ W/m})}{(5.7 \text{ W/m})} (0.06 \text{ m}) = 0.01 \text{ } \mu\text{K},$$

and for Eq.(11) gives

$$\Delta T_{\text{gradient}} \cong (3 \times 10^{-4} \text{ K/m}) \left[ \frac{(0.030 \text{ m})}{(0.74 \text{ m})} \right]^2 (0.03 \text{ m}) = 0.01 \mu\text{K} ,$$

Both assumptions lead to small estimates of the temperature difference imposed on the cell by the inner shell.

#### Asymmetrical connections to the cell

Asymmetric thermal conduction of the plastic spacers between the cell and the inner shell was considered above in connection with gradients induced by the cell's ramp rate. Although spacer asymmetry does not play an important role in connection with the temperature difference imposed by the inner shell's gradient, it is important for heat flows originating on the cell.

There is an additional asymmetry due to the electrical connections to the cell. Each coaxial cable contains a central #30 wire and a #30 drain wire with aluminized plastic film. The total cross section from the three coaxial cables and the thermometer and heater connections is approximately equal to ten #30 copper wires, giving a thermal conductivity along the 0.03 m length of

$$\kappa_{\text{wires}} \cong 7 \times 10^{-4} \text{ W/K} ,$$

about 1% of the total conductivity to the cell. This is negligible in comparison with the spacer asymmetry already considered.

In the Science Requirements Document radiation was estimated to account for about one quarter of the total conductance between the inner shell and the cell. If we assume the unrealistic case where radiation is emitted from only one end then  $\Delta T_{\text{body}}$  will be roughly doubled. More realistically, the surface with the highest emissivity is the tape wrapped around the cell's middle to secure the electrical leads. The resulting effect of this emissivity asymmetry on the cell's temperature distribution will be small compared with the effects already considered. As was the case with spacer asymmetry, emissivity asymmetry is more important in connection with heat flows originating on the cell than with the temperature gradient of the surrounding inner shell.

#### Summary

The temperature differences calculated above are

Allowed maximum	$\Delta T$	0.21 $\mu\text{K}$
Thermistor power	$\Delta T_{\text{therm}}$	0.05 $\mu\text{K}$
Cooling of body	$\Delta T_{\text{body}}$	0.07 $\mu\text{K}$
Cooling of window	$T_{\text{window}}$	0.09 $\mu\text{K}$
Imposed by inner shell	$\Delta T_{\text{gradient}}$	0.01 $\mu\text{K}$

The cell has two "hot spots", one at the center of the window and one near the thermistor. The second spot, the sum of  $\Delta T_{\text{therm}}$  and  $\Delta T_{\text{body}}$ , is hotter. Therefore the maximum expected temperature difference is

$$\Delta T_{\text{total}} = \Delta T_{\text{therm}} + \Delta T_{\text{body}} + \Delta T_{\text{gradient}}$$

$$= 0.05 \mu K + 0.07 \mu K + 0.01 \mu K$$

$$= 0.12 \mu K .$$

Though acceptable, the estimated magnitude  $\Delta T_{\text{total}}$  is rather close to the allowed maximum of  $0.21 \mu K$ . The most important contributions are due to the thermistor power and the ramp rate  $\dot{T}$ . The first contribution could be approximately halved by dividing the thermistor power between two thermistors imbedded on opposite sides of the cell body. The second contribution could be halved by halving the ramp rate, although any such decrease must be weighed against the available mission time.

The cell design will be modified to include a metal cover plate for the sapphire window to prevent radiative heat transfer directly to the interior of the cell.

# THE SHUTTLE'S VIBRATION ENVIRONMENT IS COMPATIBLE WITH THE OSCILLATING SCREEN VISCOMETER

Robert F. Berg and Michael R. Moldover

[30 July 1993]

## Summary

The oscillating screen viscometer is designed for useful operation in the vibration environment of the Space Shuttle. The following analysis compares recently analyzed on-orbit vibration data against the viscometer's measured vibration sensitivity. During routine crew activities the effect of the resulting vibration on the precision of the viscosity measurement will be tolerable. However, there is a possible problem if the astronauts use unisolated exercise equipment for extended periods of time.

The required precision of a single viscosity measurement is approximately 0.18%, or a signal-to-noise ratio of about 600. The "signal" is the effect of viscosity on the oscillator's frequency response, measured from 0 to 12.5 Hz, and the "noise" is the random effect of vibration on the same frequency response. (Electronic noise is neglected in this analysis.) The viscometer's sensitivity to both viscosity and vibration is a slowly varying function of frequency. In contrast, the low-frequency on-orbit vibrations of the Shuttle typically occur within narrow peaks less than 0.3 Hz wide. These peaks apparently correspond to various Shuttle vibration modes. They are frequently excited by crew activity [1], although other sources include thruster firings, satellite launches, and use of the Shuttle's manipulating arm.

The amplitude of a Shuttle vibration mode can be large enough to significantly degrade the viscometer's signal-noise-ratio at nearby frequencies. However, because the viscometer is sensitive to viscosity over the range of 2 to 60 Hz, the overall signal-to-noise ratio can still be acceptable. For example, due to a vibration mode of the Shuttle, the oscillator's frequency response might be noisy between 4.7 and 5.0 Hz. However, by using the information between 2 and 4.7 Hz, the viscosity can still be determined to acceptable precision.

Our measurements of the viscometer's sensitivity to vibration were obtained with a spectrum analyzer operating from 0 to 12.5 Hz with 0.031 Hz wide frequency bins (a result of measurements lasting 32 s). In general the sensitivity to vibration depended both on frequency and on which of the viscometer cell's six rigid-body modes were driven. The worst case was summarized by the statement that, after coherently averaging 20 measurements, a vibration level of  $2 \times 10^{-5} \text{ G/Hz}^{1/2}$  would contribute 0.1% noise to the viscosity as determined from only a single frequency bin. (Here  $1 \text{ G} \equiv 9.8 \text{ m} \cdot \text{s}^{-2}$ .) In what follows, the total signal-to-noise ratio is related to the signal-to-noise ratio at each frequency bin.

The total signal-to-noise ratio  $\Gamma$  can be written in terms of the signal-to-noise ratio  $\Gamma_i$  associated with each of the  $N$  frequency bins.

$$\Gamma = \left[ \sum_{i=1}^N \Gamma_i^2 \right]^{1/2} \quad (1)$$

Each bin's  $\Gamma_i$  is inversely proportional to the vibration noise density at the bin's frequency. The value of  $\Gamma_i$  is also inversely proportional to the viscometer's sensitivity to vibration.

In order to directly use plots of the Shuttle's vibration spectra [1,2] and avoid the use of spectral integrals, we characterized the vibration dependence of the signal-to-noise ratio by the following worst-case simplification:

$$\begin{aligned} \Gamma_i &= \Gamma_0 & , \text{ for } a_i < a_0 \\ &= 0 & , \text{ for } a_i > a_0 . \end{aligned} \quad (2)$$

In other words, in frequency bins where the vibration noise density  $a_i$  exceeded the threshold  $a_0$ , all viscosity information was assumed to be lost, and the signal-to-noise ratio in other frequency bins was limited to the value corresponding to the threshold value  $a_0$ .

We made another conservative simplification by examining only the frequency range of 3 to 5 Hz, corresponding to 64 bins. The 3 Hz limit is safely within the range where the viscometer is sensitive to viscosity, and the 5 Hz limit corresponds to the upper cutoff of some of the SAMS data as well as the viscoelastic limit for xenon near the critical temperature. A threshold value of  $a_0 \equiv 5 \times 10^{-5} \text{ G} \cdot \text{Hz}^{-1/2}$  was selected for convenient use

with the spectral plots in Ref.[1]. The limiting signal-to-noise ratio was set at  $\Gamma_0 \approx 400$ , corresponding to  $\Gamma_i = 1000$  at  $a_i = 2 \times 10^{-5} \text{ G} \cdot \text{Hz}^{-1/2}$ . With these choices, Eq.(1) simplifies to

$$\Gamma = N^{1/2} \Gamma_0 f^{1/2} \quad (3)$$

$$\Gamma = 3200 f^{1/2}, \quad (4)$$

where  $f$  is the fraction of the frequency range where the acceleration noise threshold was not exceeded. For example, if vibration was excessive between 4.7 and 5.0 Hz, then the usable fraction of the frequency range was  $f=0.9$ .

Because an overall signal-to-noise ratio of  $\Gamma=600$  is required, Eq.(4) implies that the vibration level must not exceed the threshold value over at least the fraction  $f=0.03$  of the frequency range. Values of  $f$  derived from Shuttle vibration spectra are listed in Table 1. Most of the vibration spectra were taken from the summary plots of Ref.[1]. In this report, Baugher et al. noted that the spectra are roughly similar in shape, independent of the location of the accelerometer's location and independent of the presence of a Spacelab module. However, the amplitude varies by as much as a factor of 50 as a function of time, with the greatest disturbance occurring when the crew used exercise equipment.

The main conclusion to be drawn from Table 1 is that vibration caused by routine crew activity will not significantly degrade the viscometer's performance. However, crew exercise can lower the value of  $f$  to 0.1 and may thereby lower the viscometer's precision. This problem can be alleviated either by appropriate isolation of the exercise equipment or by limiting crew exercise to isolated periods of brief duration, say the length of a single viscosity point, which is 20 minutes.

TABLE 1: Usable fraction  $f$  of the 3–5 Hz frequency range, defined by the criterion that the acceleration noise density did not exceed  $5 \times 10^{-5} \text{ G} \cdot \text{Hz}^{-1/2}$ . The columns X,Y,Z refer to the vector components of the acceleration measurements. The value of  $f$  must be greater than 0.03 to achieve an acceptable signal-to-noise ratio from a 20 minute viscosity measurement. Two marginal cases are underlined.

<u>Mission</u>	<u>Activity</u>	<u>Time</u>	<u>f(X)</u>	<u>f(Y)</u>	<u>f(Z)</u>
STS-40 (SLS-1)	routine	3/01:03	1.0	0.9	0.8
	sleep	6/13:20	1.0	1.0	1.0
STS-43 (TDRSS)	routine	0/07:33	0.9	0.8	0.8
STS-47 (SL-J)	routine	0/22:16	1.0	0.9	0.9
STS-50 (USML-1)	routine	1/22:42	1.0	0.9	0.9
	ergometer	7/19:26	0.6	0.3	<u>0.1</u>
	erg. isolated	5/18:51	1.0	0.9	0.7
STS-52 (USMP-1)	routine	6/01:22	1.0	1.0	0.9
	noisiest [2]	0/04:30	0.8	<u>0.1</u>	0.6

#### References

1. "Low-frequency vibration environment for five Shuttle missions", C.R. Baugher, G.L. Martin, and R. DeLombard, NASA Technical Memorandum 106059 (1993).
2. R.A. Wilkinson, private communication (1993).

# CALIBRATION OF THE OSCILLATING SCREEN VISCOMETER

Robert F. Berg and Michael R. Moldover  
Thermophysics Division  
National Institute of Standards and Technology

[29 October 1993]

## Summary

We have devised a calibration procedure for the oscillating screen viscometer which can provide the accuracy needed for the flight measurement of viscosity near the liquid-vapor critical point of xenon. The procedure, which makes use of the viscometer's wide bandwidth and hydrodynamic similarity, allows the viscometer to be self-calibrating. To demonstrate the validity of this procedure we measured the oscillator's transfer function under a wide variety of conditions. We obtained data using CO<sub>2</sub> at temperatures spanning a temperature range of 35 K and densities varying by a factor of 165, thereby encountering viscosity variations as great as 50%. In contrast the flight experiment will be performed over a temperature range of 29 K and at only a single density, and the viscosity is expected to change by less than 40%.

The measurements show that, after excluding data above 10 Hz (where frequency-dependent corrections are poorly modeled) and making a plausible adjustment to the viscosity value used at high density, the viscometer's behavior is fully consistent with the use of hydrodynamic similarity for calibration. Achieving this agreement required understanding a 1% anelastic effect present in the oscillator's torsion fiber.

## 1. Introduction

Of the several goals of the Critical Viscosity Experiment, the most easily quantifiable is determination of the exponent for the divergence of viscosity near the liquid-vapor critical point. In order to meet the nominal goal of determining this exponent to within  $\pm 1\%$  without reliance on the details of an accurate crossover theory, the measured viscosity must be proportional to the true viscosity to within  $\pm 0.2\%$  [1]. Achieving this requires accurate knowledge of three aspects of the experiment. These are the viscometer's hydrodynamics, all nonviscous forces, and instrumental effects such as amplifier nonlinearity.

Because measurement of viscosity to an absolute accuracy of  $\pm 0.2\%$  is difficult, it is rarely achieved. Fortunately, in order to test the theory for the viscosity divergence, it is unimportant if the measured viscosity differs from the true viscosity by an arbitrary scale factor. To quantify the effects of other errors, suppose that the measured viscosity  $\eta_m$  is a quadratic function of the true viscosity  $\eta$ , namely

$$\eta_m = a_0 \eta_1 + a_1 \eta + (a_2/\eta_1) \eta^2, \quad (1)$$

where  $\eta_1$  is a reference viscosity far from  $T_c$ . The important error is the deviation from proportionality. For small errors, this quantity can be written as

$$\frac{\eta_{m2}/\eta_{m1}}{\eta_2/\eta_1} - 1 \cong - \left[ \frac{a_0}{a_1} \right] \left[ \frac{\eta_2 - \eta_1}{\eta_2} \right] + \left[ \frac{a_2}{a_1} \right] \left[ \frac{\eta_2 - \eta_1}{\eta_1} \right]. \quad (2)$$

The suffix 2 refers to the reduced temperature  $2 \times 10^{-6}$ . If the reference viscosity is at the reduced temperature  $2 \times 10^{-4}$ , then the change of viscosity anticipated in the flight experiment is approximately

$$\eta_2 - \eta_1 \cong 1.2 \eta_1. \quad (3)$$

In Eq.(2), the value of  $a_1$  need not be known; rather the sum of the first term, or "zero offset", and the second term, or "nonlinearity", must be less than 0.2%.

The hydrodynamic theory for most viscometers starts with an ideal geometry, for example a cylinder. Corrections for nonideal features such as edges or ellipticity are almost always required, and they are either calculated with an elaboration of the hydrodynamic model or measured in ancillary experiments. These corrections must be known throughout the ranges of frequency, density, and viscosity in which the viscometer operates. For the oscillating screen viscometer, the ideal geometry is the transversely oscillating cylinder. The most important correction to this model is the use of an effective cylinder radius chosen to best match the oscillator's behavior. To achieve the needed accuracy by this route, further corrections, determined by experiments with calibrating fluids and possibly of an ad hoc form, would be needed.

However, there is another, more powerful method to accurately characterize the hydrodynamics of the oscillating screen viscometer, made possible by the fact that the viscometer is sensitive to viscosity over a relatively wide frequency bandwidth. As explained in Section 2 on hydrodynamic similarity, this method does not rely on a specific hydrodynamic model, and it allows the viscometer to be self-calibrating.

The calibration tests described in Section 3 verified the applicability of hydrodynamic similarity for measuring changes in the viscosity with the oscillating screen. Our measurements of viscosity changes were consistent with the best viscosity measurements available in the literature ("±0.1%"). We note that, because we were comparing changes of the viscosity, the accuracy of this comparison was ±1% at best, worse than the required ±0.2%. However, the consistency achieved in a wide range of conditions described in Section 3 gives us confidence that the instrument has the necessary accuracy for use in the Critical Viscosity Experiment.

Section 4 outlines a calibration procedure based hydrodynamic similarity.

## 2. Hydrodynamic similarity

An torsion oscillator can be characterized by measurements of its transfer function  $H(\omega)$ , defined by

$$H(\omega) \equiv \frac{\theta(\omega)}{\tau(\omega)}, \quad (4)$$

where  $\theta(\omega)$  and  $\tau(\omega)$  are the measured angular displacement and  $\tau(\omega)$  is the applied torque. (At present we can measure only the product  $k_{tr}H$ , where  $k_{tr}$  is an inaccurately known transducer coefficient assumed to be independent of frequency.) By immersing it in a fluid, an oscillator can be used as a viscometer, but only over a finite frequency bandwidth. This bandwidth can be defined as the frequency range where the viscometer's sensitivity, defined by the dimensionless quantity

$$\frac{\eta}{H} \frac{\partial H}{\partial \eta}, \quad (5)$$

is comparable to unity. (Fig. 1 shows examples.) For high- $Q$  oscillators the sensitivity is significant only in a narrow frequency range near the vacuum resonance frequency  $\omega_0$ . In contrast, for a low- $Q$  oscillator such as the oscillating screen viscometer, viscosity can be measured over a broad frequency range. Equivalently, at a fixed density  $\rho$  and viscosity  $\eta$ , the viscometer is sensitive to viscosity over a broad range of viscous penetration lengths  $\delta$ , defined by

$$\delta \equiv \left[ \frac{2\eta}{\rho\omega} \right]^{1/2}. \quad (6)$$

Although hydrodynamic similarity most often refers to scaling of the Navier–Stokes equation with the Reynolds number, here we are interested in the similarity that exists for small amplitude oscillatory flow. The linear Navier–Stokes equation can then be written in terms of a dimensionless velocity, pressure, time, and spatial derivative,  $u'$ ,  $p'$ ,  $t'$ , and  $\nabla'$  by rescaling their dimensional equivalents with respect to a characteristic length  $R$ , a characteristic time  $\omega^{-1}$ , and a characteristic pressure  $\eta\omega$ . The result,

$$\frac{\partial u'}{\partial t'} = \frac{\eta}{\rho\omega R^2} \nabla p' + \frac{\eta}{\rho\omega R^2} \nabla'^2 u', \quad (7)$$

is an equation parameterized only by the ratio  $(\delta/R)^2$ .

This result can be combined with the harmonic oscillator equation to give the oscillator's response function  $H(\omega)$  in terms of the dimensionless frequency  $\Omega \equiv \omega/\omega_0$ :

$$H(\omega)^{-1} = k_\theta [(1-\Omega^2) + i\Omega^2(\rho/\rho_s)B(R/\delta)]. \quad (8)$$

Here,  $\rho$  and  $\rho_s$  are the densities of the fluid and the oscillator body respectively,  $k_\theta$  is the oscillator's spring constant, and  $B(R/\delta)$  is a function characteristic of the oscillator's geometry. (The convention  $e^{+i\omega t}$  is used.) The most important feature of Eq.(8) is that the oscillator's transfer function depends on the fluid's viscosity only through the viscous penetration length.

Eq.(8) requires that the oscillator be characterized by only the undamped resonance frequency  $\omega_0$ , the oscillator's density  $\rho_s$ , and the spring constant,  $k_\theta = I\omega_0^2$ , where  $I$  is the oscillator's moment of inertia. The frequency  $\omega_0$  can be accurately measured in vacuum. The value chosen for the oscillator's density  $\rho_s$  is unimportant because it divides the function  $B(R/\delta)$ . In effect the product  $(\rho/\rho_s)B$  is measured in the calibration. For the oscillating screen, we estimated  $\rho_s$  by weighing a representative piece of the screen and then modeling the screen as a single cylinder of radius  $R$ . The geometry of the oscillator's torsion fiber was too complex to calculate the spring constant  $k_\theta$  to the needed accuracy. However, the ratio  $k_{tr}/k_\theta$ , where  $k_{tr}$  is the transducer coefficient, could be obtained directly by measuring the response function  $H(\omega)$  in the limit of 0 Hz. This required an understanding of the torsion fiber's anelasticity, described in Appendix C.

The function  $B(R/\delta)$  is known exactly only for simple geometries. For an arbitrarily complicated geometry, it can be inferred from measurements of the oscillator's transfer function.

$$B(R/\delta) = \frac{[(k_\theta/k_{tr})H(\omega)]^{-1} - (1-\Omega^2)}{i\Omega^2(\rho/\rho_s)}. \quad (9)$$

For an imperfectly known geometry, the dependence of  $B$  on the viscous penetration length

$\delta$  can be obtained by either (1) the use of a single frequency with various calibrating fluids or by (2) the use of a single calibrating fluid measured at various frequencies. The first strategy is limited by the accuracy of the calibrating fluids' viscosities. (Density inaccuracy is assumed to be insignificant.) In contrast, because the second strategy makes use of only one fluid, it is potentially highly accurate for calibrating a viscometer intended to measure relative changes, as is the case for the planned Critical Viscosity Experiment. The second strategy can be implemented only in a wide-bandwidth viscometer, also true for the planned flight experiment. Appendices A and B explain in more detail the necessity of using a low- $Q$  oscillator to achieve a wide bandwidth in the viscosity measurement.

Calibration of the oscillating screen viscometer amounts to a measurement of the hydrodynamic geometry function  $B(R/\delta)$  over a range of viscous penetration lengths encompassing the intended operating conditions. This can be done with any fluid having a kinematic viscosity similar to xenon. Furthermore, for the measurement of relative viscosity changes, the viscometer is self-calibrating, namely no fluid other than xenon will be needed.

Self-calibration is possible because the anticipated variation of  $\delta$  caused by changing the temperature is less than the variation of  $\delta$  induced by changing the frequency at a single temperature. For example, for the flight experiment in xenon close to  $T_c$ ,  $\delta$  at 5 Hz is expected to be no more than 20% greater than the minimum far from  $T_c$ . The same penetration length can be obtained far from  $T_c$  at 3.5 Hz, which, as indicated by Fig. 1, is within the bandwidth of the viscometer.

### 3. Tests of the applicability of hydrodynamic similarity

#### A. Choice of fluid

Carbon dioxide was chosen as the calibrating fluid because accurate viscosity data for  $\text{CO}_2$  are available at kinematic viscosities comparable to that of xenon at its critical density. This criterion excluded liquids such as water and toluene. The additional requirement of operation between 0 and 60° C and at pressures less than 10 MPa excluded other well-measured gases such as argon and nitrogen. We excluded  $\text{SF}_6$  because its viscosity is known less accurately than that of  $\text{CO}_2$ .

We made use of previous viscosity measurements included in the recent correlation of Vesovic et al. [2]. We initially considered the use of four density ranges: low (where  $\partial\eta/\partial\rho$  is small), moderate but below the critical region, the critical region, and above the critical region. The most accurate measurements were made at low densities near room temperature. For these data we used the representation of Kestin, Ro, and Wakeham [3].

Within  $\pm 0.2\%$ , the data from Kestin's group agree with both the more recent measurements by Vogel and Barkow [4] and the correlation of Ref.[2] over the 25–61°C temperature range used in the present measurements.

At moderate densities we again used measurements from Kestin's group. Kestin, Korfali, and Sengers [5] reported viscosity measurements made at 31.6 °C and at densities up to  $307 \text{ kg} \cdot \text{m}^{-3}$ . At the higher densities, their values disagree by as much as 1% with the older measurements of Kestin, Whitelaw, and Zien [6]. This latter set we found useful because it reported the temperature dependence at moderate densities.

We used no measurements made at densities near the critical density of  $\text{CO}_2$ . Vesovic et al. state that for densities  $\rho$  outside the limits  $300 \text{ kg} \cdot \text{m}^{-3} < \rho < 600 \text{ kg} \cdot \text{m}^{-3}$ , the critical viscosity enhancement is less than 1%. Inside this region, experimental difficulties are greater, and Vesovic et al. could not correlate the data of Iwasaki and Takahashi [7] to better than 2%. Our own measurements [8] close to the critical point of  $\text{CO}_2$  were made only at the critical density.

We made no measurements above  $600 \text{ kg} \cdot \text{m}^{-3}$  because of the high pressures involved.

The kinematic viscosity of  $\text{CO}_2$  is always higher than that of xenon at critical density. (The minimum kinematic viscosity tends to occur near the critical density.) This is not surprising: with the usual exceptions of  $^3\text{He}$  and  $^4\text{He}$ , xenon's high molecular weight causes its minimum kinematic viscosity to be less than that of any other fluid. However, the necessary range of penetration depths could still be covered by our  $\text{CO}_2$  measurements. In the flight experiment, the expected range for the penetration length in xenon at 5 Hz is

$$55 \mu\text{m} < \delta < 66 \mu\text{m} \quad [10^{-2} < (T-T_c)/T_c < 10^{-7}]. \quad (10)$$

This range of penetration lengths was easily spanned by the present measurements. For example, this was done with  $\text{CO}_2$  at  $295 \text{ kg} \cdot \text{m}^{-3}$  by operating the viscometer between 5.6 and 8.1 Hz.

### B. Technique

In principle self-calibration need be done only after the viscometer is loaded with xenon; the present tests were made to demonstrate the applicability of hydrodynamic similarity for the oscillating viscometer. Potential causes of failure included all three aspects mentioned in the Introduction's first paragraph. For example, the flow could have been too large for the linearized Navier–Stokes equation to apply, there could have been an

unexpected coupling to a bending mode of the screen, or the transducers could have had an unexpected frequency dependence. To look for such effects, we covered a wide range of conditions. We spanned a factor of 165 in density and a 50% change in both the viscosity and the kinematic viscosity. Measurements were made up to 25 Hz in the temperature range from 25 to 61°C. In contrast, the flight experiment will take place in a narrow range of conditions. Only one density will be used, and the viscosity is expected to change by less than a 40%. Frequencies less than 12.5 Hz will be used in the narrower temperature range of 16 to 45°C.

Using the method previously described [1], we measured the oscillator's transfer function over the range 0–25 Hz at the five densities and temperatures listed in Table 2. The densities, determined by weighing the filled cell, were chosen to fall near those used Kestin, Whitelaw, and Zien [6]. We also made measurements at low frequencies to obtain the transducer coefficient  $k_{tr}$ . Preceding these tests, we made measurements of the oscillator's resonance frequency and  $Q$  in vacuum between 7 and 81°C. In many cases, we extended the measurement time to several hours to improve the signal-to-noise ratio. In most of the data plots, the trends of the data are clarified by averaging the data in groups of 10.

### C. Density dependence of $\eta$ near room temperature

Fig. 2 shows the frequency response measured at four of the five different densities. (The data at  $242.8 \text{ kg} \cdot \text{m}^{-3}$  are similar to those at  $295.1 \text{ kg} \cdot \text{m}^{-3}$  and are omitted for clarity.) The viscometer was sensitive to viscosity changes over most of the measured frequency range. This is indicated by Fig. 1, which shows the viscometer's sensitivity when modeled as an ideal cylinder oscillating in  $\text{CO}_2$  at a density of  $295.1 \text{ kg} \cdot \text{m}^{-3}$ . For example, at 8 Hz, a viscosity change of 10% would change the oscillator's response by about 8%.

Using Eq.(9), we derived values of the function  $B(R/\delta)$ . The results, which include corrections for the spring's anelastic character (Appendix C) and the effects of four low-pass electronic filters (Appendix D), are shown in Fig. 3. Also plotted is the value of  $B_c(R/\delta)$  calculated for the case of a transversely oscillating cylinder of radius  $R \approx 13.8 \text{ } \mu\text{m}$  [9]. (For clarity,  $(R/\delta)^2 |B|$ , not  $|B|$ , is plotted.)

The consistency of the data can be examined more closely in Fig. 4, which is a plot of the ratio  $|B/B_c|$ . To the extent that the data fall on a single, smooth curve, they are consistent with the expected hydrodynamic similarity. However, there are two types of

small discrepancies. The first kind occurs at higher frequencies, especially above 15 Hz.

An example is the upturn near  $R/\delta=0.04$  of the data taken at  $1.79 \text{ kg}\cdot\text{m}^{-3}$ . This discrepancy may be due to incorrect modeling of the corrections for anelasticity or of the electronic filters. For example, in modeling the effect of a low-pass filter on the output of the square root amplifier we ignored the frequencies of all but the fundamental Fourier component. Also, we made no attempt to characterize anelastic effects above the resonance frequency of  $\omega_0/2\pi = 11.5 \text{ Hz}$ .

The second kind of discrepancy, which occurs between the data at 295.1 and  $90.1 \text{ kg}\cdot\text{m}^{-3}$ , can be removed if the value of the viscosity used at the higher density is reduced by 1%. This adjustment can be partially justified in two ways. First, as shown in Fig. 5, it yields a curve with continuous slope as well as value. Second, the amplitude of the adjustment is consistent with both the scatter of the original data and with the disagreement between the values of Kestin, Korfali, and Sengers [5] and of Kestin, Whitelaw, and Zien [6]. The viscosity data of Ref. [6] are about 1% less than those of Ref. [5] near  $300 \text{ kg}\cdot\text{m}^{-3}$ .

Fig. 5 shows the experimentally derived function  $B(R/\delta)$  after addressing both discrepancies. Only data between 1 and 10 Hz were used, and the value of the viscosity used at  $295.1 \text{ kg}\cdot\text{m}^{-3}$  from Kestin, Korfali, and Sengers [5] was lowered by 1%. The result is a smoothly varying function of penetration length that is independent of density and is fully consistent with hydrodynamic similarity. The strongest deviations from the cylinder model occur at large viscous penetration lengths, or low values of  $R/\delta$ . This is to be expected for  $R/\delta < 0.033$ , where  $\delta$  is half the distance between screen wires. We emphasize that the cylinder model was used only as a convenience to examine the data. No explicit hydrodynamic model is needed to obtain the hydrodynamic geometry function  $B(R/\delta)$ . Also, the value chosen for the characteristic length  $R$  is unimportant for the calibration as long as the same length is used for both calibration and measurement.

#### D. Temperature dependence of $\eta$ at moderate density

Fig. 6 shows plots of  $|B/B_c|$  as a function of  $R/\delta$  obtained at 31.6, 34.6, and  $40.6^\circ\text{C}$  for a constant density of  $242.8 \text{ kg}\cdot\text{m}^{-3}$ . For consistency in this comparison we used only data from one investigation, that of Kestin, Whitelaw, and Zien [6]. Over the range  $0.2 < R/\delta < 0.3$  the data for  $|B/B_c|$  obtained at 31.6 and  $40.6^\circ\text{C}$  are consistent to within  $\pm 0.1\%$  of the viscosity. The viscosity changes by 2.9% between these two temperatures.

Although noisier, the data at 34.6°C are significantly higher over the same range in  $R/\delta$ , corresponding to a viscosity disagreement of as much as -0.2%. We do not know the source of this small disagreement.

#### E. Temperature dependence of $\eta$ at low density

We measured the oscillator's transfer function in  $\text{CO}_2$  at 25.6, 40.6, and 60.6°C for a constant density of  $1.79 \text{ kg} \cdot \text{m}^{-3}$ . Fig. 7 shows the transfer function measured at the three temperatures. (The temperature accuracy is  $\pm 0.1 \text{ K}$ .)

Although, the resulting variation in the viscosity (11%) was less than that resulting from varying the density, these tests were important for two reasons. First, the most accurate data for the viscosity are at low density. Second, the flight experiment will measure viscosity variation vs. temperature and thus is susceptible to systematic errors caused by temperature changes. To avoid exceeding the cell's pressure tolerance, the temperature range required to look for such errors is best explored at low density.

The consistency of the values derived for the hydrodynamic geometry function  $B(R/\delta)$  can be seen in Fig. 8. As previously noted, there are small unexplained discrepancies at higher frequencies. However, the agreement is excellent up to about  $R/\delta=0.028$  or about 12 Hz. In this frequency range, the corresponding discrepancies in viscosity fall within  $\pm 0.1\%$ . This error  $\Delta\eta$  is consistent with the data of Kestin, Ro, and Wakeham [3] within their stated accuracy. Although, this comparison does not test the viscometer's ability to measure absolute viscosity, it does test the viscometer's ability to measure the variation of viscosity with temperature. The agreement in the latter quantity is

$$\frac{\Delta\eta}{\eta(60.6^\circ\text{C}) - \eta(25.6^\circ\text{C})} = \frac{\pm 0.1\%}{\pm 11\%} = \pm 1\% . \quad (11)$$

Thus, the oscillating's screen performance is consistent with the most accurate viscosity data available.

#### 4. Calibration procedure

The following procedure will be used for the flight experiment.

- (1) With the viscometer cell evacuated, measure the oscillator's transfer function between 0.001 Hz and the resonance frequency (about 11.5 Hz) at temperatures between 10 and 60°C. This will determine the anelastic corrections to the torsion

fiber's spring constant.

- (2) With the viscometer cell evacuated, measure the transfer function near the resonance frequency at temperatures between 10 and 60° C. This will determine the temperature dependence of the oscillator's resonance frequency  $\omega_0$  and quality factor  $Q$ .
- (3) After the loading the viscometer cell with xenon at its critical density, measure the transfer function between 1 and 12.5 Hz at a temperature  $T_{cal}$  sufficiently far from  $T_c$  to eliminate significant effects due to stratification in Earth's gravity (say  $T_{cal} = T_c + 3$  K). This will determine the hydrodynamic geometry function  $B_{cal}(\delta)$  over the range of  $\delta$  expected at 5 Hz in the flight experiment. This measurement will also be done during the flight experiment, in effect calibrating the viscometer in orbit.
- (4) Viscosity values at  $T$  close to  $T_c$  will be obtained by
  - (a) Measuring  $H(\omega)$  at the temperature  $T$ .
  - (b) Using Eq.(9) to obtain  $B(T)$ .
  - (c) Using  $B_{cal}(\delta)$  to invert  $B(T)$  and thereby obtain  $\delta$ .
  - (d) Calculating  $\eta = (1/2)\rho\omega\delta^2$ .

The resulting viscosity values will be relative to the viscosity at the calibrating temperature  $T_{cal}$ . This has already been measured to an accuracy of 0.8% [8].

#### Appendix A: Bandwidth of an oscillator viscometer

The oscillating screen viscometer's calibration relies on viscosity measurements made over a substantial range of frequencies. This section explains why, for fixed spring constant, an overdamped, or "low- $Q$ " oscillator is necessary for such measurements.

Low- $Q$  oscillators are superior for measuring viscosity over a wide range of frequencies because the transfer function of a high- $Q$  oscillator is sensitive to dissipation only near its resonance frequency  $\omega_0$ . This can be illustrated by considering a torsion oscillator with moment of inertia  $I$ , spring constant  $k_\theta$  and frequency-independent dissipation coefficient  $\nu$ . For a sinusoidal torque  $\tau(\omega)$  of fixed amplitude, the angular displacement  $\theta$  is given by

$$\theta = \frac{\tau(\omega)}{[-I\omega^2 + i\omega\nu + k_\theta]}. \quad (\text{A1})$$

Changes in  $\nu$  can be detected through changes in  $\theta$ . The oscillator's sensitivity to dissipation is measured by the normalized derivative

$$\frac{\nu}{\theta} \frac{\partial \theta}{\partial \nu} = \frac{-i\omega\nu}{[-I\omega^2 + i\omega\nu + k_\theta]}. \quad (\text{A2})$$

Making the substitutions

$$k_\theta = I\omega_0^2 \quad (\text{A3})$$

and

$$Q \equiv \frac{I\omega_0}{\nu} \quad (\text{A4})$$

allows the oscillator's sensitivity to dissipation to be rewritten as

$$\frac{\nu}{\theta} \frac{\partial \theta}{\partial \nu} = \frac{-i\Omega}{[1-\Omega^2]Q + i\Omega}, \quad (\text{A5})$$

where  $\Omega \equiv \omega/\omega_0$  is the reduced frequency. (The definition of  $Q$  in Eq.(A4) is the usual quality factor generalized to include overdamped oscillators.)

Eq.(A5) shows that an oscillator's amplitude is most sensitive to changes of the dissipation coefficient at resonance. Far below resonance the elastic restoring force is much greater than the dissipative force, and far above resonance inertia is dominant. The oscillator's  $Q$  determines what is "near" and what is "far". Table 3 illustrates this point by using Eq.(A5) to compare the magnitudes of the dissipation sensitivities of two hypothetical oscillators whose  $Q$ 's differ by a factor of 100. For example, if the oscillator with  $Q=10$  is driven with constant torque at half its resonance frequency, a 100% increase in the dissipation will cause only a 6.7% decrease in the oscillator's amplitude.

The bandwidth in which the oscillator is sensitive to dissipation can be defined by the lower and upper frequencies  $\omega_-$  and  $\omega_+$  where the magnitude of the sensitivity falls to 1/2. The relation of this bandwidth to the  $Q$  is given by

$$\frac{\omega_+ - \omega_-}{\omega_0} = \frac{\sqrt{3}}{Q}. \quad (\text{A6})$$

For a highly damped oscillator ( $Q \ll 1$ ) the bandwidth is more appropriately characterized by the ratio

$$\frac{\omega_+}{\omega_-} \approx \frac{3}{Q^2}. \quad (\text{A7})$$

In contrast to the preceding illustration, the dissipation coefficient  $\nu$  of an oscillator viscometer is a complex function of frequency. Although this complicates the analysis, numerical calculations with specific hydrodynamic models [10] show that the above result

still holds qualitatively, namely a low- $Q$  oscillator is sensitive to changes in the viscosity over a wider range of frequencies than a high- $Q$  oscillator.

The signal-to-noise ratio of a viscometer is determined both by its sensitivity to dissipation and by noise in the measurement. Thus, if a viscometer is operated outside its bandwidth, its insensitivity to the viscosity can be at least partially compensated by reducing the accompanying noise. This issue is quantified in Appendix B.

#### Appendix B: Signal-to-noise ratio of an oscillator viscometer

The oscillating screen viscometer was developed because the Space Shuttle's typical vibration environment was predicted to degrade the precision of our earlier, high- $Q$  oscillator technique to an unacceptable level. The advantage of a low- $Q$  oscillator can be understood qualitatively by recalling that the rms noise magnitude of a high- $Q$  oscillator at resonance is proportional to the oscillator's  $Q$ . In contrast, as shown by Eq.(A5), its sensitivity to changes in the dissipation is independent of  $Q$ . Thus, high- $Q$  viscometers suffer more from random vibration. In the following, this argument is refined through a derivation of the signal-to-noise ratio for a measurement of an oscillator's dissipation.

First, we will consider the detrimental effect of mechanical vibrations on the signal-to-noise ratio. Our model is an oscillator whose spring is attached to a randomly vibrating wall. When the oscillator is driven by changes of the wall's angular position  $\theta_w$ , the equation of motion is

$$I \frac{d^2 \theta}{dt^2} + \nu \frac{d\theta}{dt} + k_\theta (\theta - \theta_w) = 0 \quad (B1)$$

Because the position-sensing electrodes are fixed to the wall, we are interested in the root-mean-square difference of the oscillator's position with respect to the wall's position, namely

$$\delta\theta \equiv [ \langle (\theta - \theta_w)^2 \rangle ]^{1/2}. \quad (B2)$$

The transfer function derived from Eq.(B1) then gives the rms magnitude of the oscillator's position  $\delta\theta$  as a function of the rms magnitude of the wall's position  $\delta\theta_w$  as

$$\delta\theta = \frac{[1 + (Q\Omega)^2]^{1/2}}{[(1-\Omega^2)^2 Q^2 + \Omega^2]^{1/2}} \Omega \delta\theta_w. \quad (B3)$$

Eq.(B3) gives the "noise" in the oscillator's signal-to-noise ratio. The "signal" is defined as the change  $\Delta\theta_0$  in the oscillator's amplitude  $\theta_0$  caused by a change  $\Delta\nu$  in the oscillator's dissipation, namely

$$\Delta\theta_0 = \left| \frac{\nu}{\theta} \frac{\partial \theta}{\partial \nu} \right| \frac{\Delta\nu}{\nu} \theta_0. \quad (B4)$$

Using Eq.(A5) this is

$$\Delta\theta_0 = \frac{\Omega}{[(1-\Omega^2)^2 Q^2 + \Omega^2]^{1/2}} \frac{\Delta\nu}{\nu} \theta_0. \quad (\text{B5})$$

(Information contained in changes of the oscillator's phase are ignored here. This does not change the overall conclusions.) The ratio of Eqs.(B3) and (B5) gives the signal-to-noise ratio as

$$\frac{\Delta\theta}{\delta\theta_0} = [1 + (Q\Omega)^2]^{-1/2} \frac{\theta_0}{\delta\theta_w} - \frac{\Delta\nu}{\nu}. \quad (\text{B6})$$

Eq.(B6) says that the signal-to-noise ratio of a dissipation measurement degrades significantly when the oscillator is operated at a reduced frequency  $\Omega > Q^{-1}$ .

Eq.(B6) also says that the signal-to-noise ratio is independent of  $Q$  in the limit of low reduced frequency. This unrealistic result occurred because sources of noise besides vibration were ignored. For example, usually there is also an electronic noise source of magnitude  $\delta\theta_e$  which, unlike  $\delta\theta$ , depends only weakly on frequency. Including such noise in the signal-to-noise ratio gives

$$\frac{\Delta\theta}{[\delta\theta^2 + \delta\theta_e^2]^{1/2}} = \frac{\theta_0}{\{[1+Q^2\Omega^2]\delta\theta_w^2 + [1+Q^2(\Omega-1/\Omega)^2]\delta\theta_e^2\}^{1/2}} \frac{\Delta\nu}{\nu}. \quad (\text{B7})$$

Examination of Eq.(B7) reveals several ways to improve the signal-to-noise ratio. Perhaps the most obvious is to increase the amplitude  $\theta_0$ . There are two limits on this strategy. First, the fluid itself has a limiting nonlinearity near the critical point. The oscillating screen viscometer is normally operated near the shear rate  $S$  characteristic of xenon at a reduced temperature of  $\epsilon=2\times 10^{-6}$ . The associated amplitude is

$$\theta_0 = \frac{S\delta}{L\omega} \approx 10^{-3} \text{ radian}, \quad (\text{B8})$$

where  $\delta$  is the viscous penetration length and  $L \approx 0.01$  m is the radius of the screen. Due to the scaling of the oscillator's resonance frequency with size, the operating frequency  $\omega$  cannot be reduced much from its nominal value of 5 Hz. Second, due to the finite dynamic range of any electronic system, the ratio  $\delta\theta_e/\theta_0$  cannot be reduced indefinitely by increasing  $\theta_0$ .

As expected from the earlier qualitative argument, Eq.(B7) says that the signal-to-noise ratio can be improved by decreasing the oscillator's  $Q$ . An exception occurs for operation at resonance with dominant electronic noise, namely  $\delta\theta_e/\delta\theta_w \gg Q$ . The signal-to-noise ratio is then

$$\frac{\Delta\theta}{[\delta\theta^2 + \delta\theta_e^2]^{1/2}} \approx \frac{\theta_0}{\delta\theta_e} - \frac{\Delta\nu}{\nu}, \quad (\text{B9})$$

which is independent of  $Q$ . Eq.(B9) is more likely to apply at higher frequencies due to

suppression of the vibration noise magnitude  $\delta\theta_w$ .

A further improvement is to operate at the frequency where the denominator of Eq.(B7) is smallest. Assuming the noise drivers  $\delta\theta_w$  and  $\delta\theta_e$  are frequency-independent, this optimum frequency is

$$\Omega = \left[ \frac{\delta\theta_e^2}{\delta\theta_w^2 + \delta\theta_e^2} \right]^{1/4}. \quad (\text{B10})$$

Because Eq.(B10) is independent of  $Q$ , the optimum frequency can fall below even the oscillator's bandwidth of sensitivity to dissipation.

Finally, the signal-to-noise ratio can be improved by using vibration isolation to reduce  $\delta\theta_w$ , by using low-noise electronics to reduce  $\delta\theta_e$ , and by increasing the measuring time.

In addition to bandwidth and vibration insensitivity, there are two additional considerations for comparing low- $Q$  and high- $Q$  viscometers. The first consideration is that a higher-frequency mode of the oscillator can contribute to the transfer function and thereby complicate its analysis. This problem is more likely if the extra mode is nearby in frequency and, like the primary mode, has a low  $Q$ . Presumably, an analysis based on hydrodynamic similarity and additional calibration measurements could still be applied in this situation. Instead we used a simpler approach. First, we designed the oscillator so that the frequency of the next lowest mode was 5 times higher than  $\omega_0$ . Second, we verified the consistency of results obtained at the same penetration length but with differing combinations of viscosity, density, and frequency. The extra effort needed to eliminate problems caused by higher modes is a disadvantage of low- $Q$  oscillators.

The second consideration is accounting for the oscillator's nonviscous dissipation. This dissipation is usually a slowly varying function of frequency. Thus, because a high- $Q$  oscillator can be used as a viscometer only in a narrow range of frequencies, the nonviscous dissipation can usually be adequately characterized by a single constant. A more elaborate characterization, e.g. the anelastic correction described in Appendix C, may be needed for a low- $Q$  viscometer. The accuracy required of this characterization depends on the ratio of the nonviscous to viscous dissipations. Because this ratio is approximately proportional to the  $Q$ , it is crucial for a high- $Q$  viscometer. The lower sensitivity to nonviscous dissipation is an advantage of low- $Q$  viscometers.

#### Appendix C: Corrections for anelasticity of the torsion fiber

The assumption of an ideal torsion spring in Eqs.(8) and (9) is known to fail for real

materials. (Although not applicable here, one such failure is nonlinearity, for example, exceeding the yield stress.) In low-amplitude oscillators, the best known manifestation of nonideal behavior is internal friction. The general phenomenon is known as anelasticity, and a material's compliance  $J(\omega)$  can be written as a complex function of frequency [11]

$$J(\omega) = J_1(\omega) - iJ_2(\omega) . \quad (C1)$$

This representation is commonly used in polymer rheology [12], and it has also been applied to "harder" materials such as metals, where there have been only limited studies of  $J(\omega)$ . Several recent studies found no significant frequency dependence of the loss compliance  $J_2(\omega)$  in Be-Cu torsion fibers [13,14] and in a steel flexure pivot [15]. In contrast, there are studies [16,17] of pure metals where  $J_2(\omega)$  was found to be frequency-dependent, generally decreasing with frequency.

We found three indications for anelasticity in the oscillating screen's torsion fiber. The first, seen at low frequencies, was a phase lag approximately independent of frequency ( $\sim 0.2^\circ$  at room temperature). The second, seen in the same frequency range, was a frequency dependence of the magnitude of the spring constant ( $\sim 1\%$  decrease upon going from 0.1 to 0.001 Hz at room temperature). The third indication was a slow relaxation of the oscillator's position following a step change in the applied force. The amplitude of this "elastic after-effect" was about 1% of the rapid initial change of the position, and its relaxation could be approximately described by an exponential with a time constant of about 400 s.

We initially considered other mechanisms for these effects. However, the elastic after-effect was observed with an applied magnetic as well as an electrostatic force, indicating behavior intrinsic to the oscillator. Also, a search at low frequencies for a subtle frequency-dependent error in the electronic instrumentation found nothing significant. We thus incorporated anelasticity into the description of the oscillator because it had a significant though small effect on the data. The final consistency achieved, both in a dispersion analysis of the anelasticity as well as in the viscosity data, justified this incorporation.

Anelasticity was added to the model of the oscillating screen by generalizing Eq.(8) for the transfer function to

$$H(\omega)^{-1} = k_0[(1-\Omega^2) + i\Omega^2(\rho/\rho_s)B(R/\delta) + k^*] , \quad (C2)$$

where the spring constant  $k_0$  was generalized to a complex function of frequency. This was done, consistent with Eq.(C1), by modifying the spring constant  $k_0$  with a complex

perturbation  $k^*$  according to

$$k_{\theta}(\omega) \equiv k_0[1 + k^*], \quad (C3)$$

$$\equiv k_0[1 + k_1(\omega) + ik_2(\omega)]. \quad (C4)$$

At the vacuum resonance frequency, the real part of the spring constant was defined to be

$$k_0 \equiv \text{Re}[k_{\theta}(\omega_0)]. \quad (C5)$$

This definition and the measurement of the oscillator's  $Q$  in vacuum fix the value of the anelastic correction at  $\omega_0$ :

$$k^*(\omega_0) \equiv 0 + iQ^{-1}. \quad (C6)$$

In the absence of viscous damping the frequency-dependent part of the spring constant  $k^*$  was obtained from the measured transfer function according to

$$k^*(\omega) = [H(\omega)/k_{tr}]^{-1} - (1 - \Omega^2). \quad (C7)$$

Fig. 9b shows a plot of the loss factor  $k_2(\omega)$ . We described its frequency dependence by a function linear in  $\log(\omega)$ , namely

$$k_2(\omega) \equiv A_2 + B_2 \log_{10}(\omega/\omega_0). \quad (C8)$$

By making use of a Kramers-Kronig relation, the function  $k_1(\omega)$  can be approximately described with no additional parameters according to:

$$k_1(\omega) = \frac{-2\ln(10)}{\pi} \left[ A_2 \log_{10}(\omega/\omega_0) + \frac{B_2}{2} [\log_{10}(\omega/\omega_0)]^2 \right]. \quad (C9)$$

Fig. 9a compares Eq.(C9) with the values of  $k_1(\omega)$  derived from the transfer function by Eq.(C7). The agreement was sensitive to the value chosen for the transducer coefficient  $k_{tr}$  and therefore determined the value of  $k_{tr}$ . In practice we used an initial value of  $k_{tr}$  determined from  $H(\omega)$  at 0.1 Hz and then adjusted it slightly to force agreement with Eq.(C6), namely,  $k_2(\omega_0) \equiv 0$ . The values of  $k_2(\omega)$  were insensitive to this adjustment of  $k_{tr}$ .

In general we required the values of the anelastic parameters  $A_2$  and  $B_2$  at all temperatures used in the viscosity measurements. For  $A_2(T)$ , we used measurements of the oscillator's  $Q$  in vacuum. For  $B_2(T)$ , we relied on low-frequency measurements made in vacuum at 23°C and in low-density  $\text{CO}_2$  at higher temperatures. (The vacuum measurements were made before the anelastic effect was understood, and thus low-frequency measurements in vacuum were made only near room temperature. Future oscillators will be characterized in vacuum at low frequencies at other temperatures.)

Fig. 10 summarizes the results for  $A_2(T)$  and  $B_2(T)$ .

We incorporated the anelastic correction into our viscosity measurements in two ways. First, we used Eq.(C2) with  $k^*(\omega)$  given by Eqs.(C8) and (C9). Second, we made a

small correction to the nominal transducer coefficient  $k'_{tr}$ , which was defined by  $H(\omega)$  at 0.1 Hz. This value was then adjusted for consistency with Eq.(C9) according to

$$k_{tr} = \frac{k'_{tr}}{[1 - k_1(0.1 \text{ Hz})]} \quad (C10)$$

We emphasize that the parameters  $A_2$  and  $B_2$  used in the anelastic corrections were determined entirely by measurements made at low frequency. The importance of the anelastic correction was greatest in the measurements of  $\text{CO}_2$  at low density, precisely where the existing viscosity data are the most accurate. Fig. 11 is the equivalent of Fig. 8 but without incorporating the anelastic correction. As expected the correction is ~1% in size.

#### Appendix D: Sensitivity to $k_{tr}$ and electronic filter corrections

We estimated the importance of errors in the determination of the transducer factor  $k_{tr}$  by varying  $k_{tr}$  from its measured value. To achieve  $\pm 0.1\%$  accuracy in the viscosity,  $k_{tr}$  must be determined to within about  $\pm 0.1\%$ .

We also estimated the importance of errors in the determination of the time constants used to correct for the effects of four low-pass electronic filters. The effect of these corrections is indicated by Fig. 12, which is the same as Fig. 3 but without filter corrections. The three most important filters all had time constants of about 1.2 ms. To achieve  $\pm 0.1\%$  accuracy in the viscosity, each of these time constants must be known to within about  $\pm 3\%$ .

# References

1. R.F. Berg and M.R. Moldover, Science Requirements Document, report to NASA Lewis Research Center (1992).
2. V. Vesovic, W.A. Wakeham, G.A. Olchow, J.V. Sengers, J.T.R. Watson, and J. Millat, J. Phys. Chem. Ref. Data 19 763 (1990).
3. J. Kestin, S.T. Ro, and W.A. Wakeham, J. Chem. Phys. 56, 4114 (1972).
4. E. Vogel and L. Barkow, Z. Phys. Chemie, Leipzig 267, 1038 (1986).
5. J. Kestin, Ö. Korfali, and J.V. Sengers, Physica 100A, 335 (1980).
6. J. Kestin, W.H. Whitelaw, and T.F. Zien, Physica 30, 161 (1964).
7. H. Iwasaki and M. Takahashi, J. Chem. Phys. 74, 1930 (1981).
8. R.F. Berg and M.R. Moldover, J. Chem. Phys. 93, 1926 (1990).
9. G.G. Stokes, Mathematics and Physical Papers, Vol. III, p.11 (Cambridge University, London, 1922); R.G. Hussey and P. Vujacic, Phys. Fluids 10, 96 (1967); R.E. Williams and R.G. Hussey, Phys. Fluids 15, 2083 (1972).
10. R.F. Berg, unpublished.
11. A.S. Nowick and B.S. Berry, Anelastic Relaxation in Crystalline Solids (Academic Press, New York, 1972).
12. J.D. Ferry, Viscoelastic Properties of Polymers, 3rd ed. (Wiley, New York, 1980).
13. T.J. Quinn, C.C. Speake, and L.M. Brown, Phil. Mag. A 65, 261 (1992).
14. W.L. Tew, T.J. Quinn, R.S. Davis, and C.C. Speake, Bull. Am. Phys. Soc. 38, 946 (1993).
15. P.R. Saulson, R.T. Stebbins, F.D. Dumont, and S.E. Mock, preprint (1992).
16. J.L. Routbort and H.S. Sack, J. App. Phys. 37, 4803 (1966).
17. J. Woigard, M. Gerland, and A. Riviere, p. 293 in Internal Friction and Ultrasonic Attenuation in Solids, C.C. Smith ed. (Pergamon, New York, 1979).

Table 1: Approximate kinematic viscosity in  $\text{m}^2 \cdot \text{s}^{-1}$  for representative densities of  $\text{CO}_2$  near room temperature. The number in parentheses is the density in  $\text{kg} \cdot \text{m}^{-3}$ . Also shown is the minimum value for xenon.

Fluid:	<u><math>\text{CO}_2(3)</math></u>	<u><math>\text{CO}_2(30)</math></u>	<u><math>\text{CO}_2(300)</math></u>	<u><math>\text{Xe}(\rho_c)</math></u>
$\eta/\rho$ :	$5.1 \times 10^{-6}$	$5.1 \times 10^{-7}$	$7.6 \times 10^{-8}$	$4.7 \times 10^{-8}$

Table 2: Viscosity values, in units of  $10^{-5} \text{ Pa} \cdot \text{s}$ , used in the calibration tests. The data sources are indicated by letters as follows: (a)=[3], (b)=[5], (c)=[6]. Although our densities and temperatures were chosen to be close to those used in the referenced studies, small interpolations in density and temperature were necessary.

$\rho/\text{kg} \cdot \text{m}^{-3}$ :	<u>1.79</u>	<u>18.9</u>	<u>90.1</u>	<u>242.8</u>	<u>295.1</u>
<u>T(<math>^{\circ}\text{C}</math>)</u>					
25.6	1.495(a)				
31.6		1.530(b)	1.616(b)	2.054(b)	2.270(b)
31.6				2.028(c)	
34.6				2.046(c)	
40.6	1.568(a)			2.086(c)	
60.6	1.663(a)				

Table 3: Examples of the sensitivity to dissipation of two oscillators, defined as the magnitude of Eq.(A5).

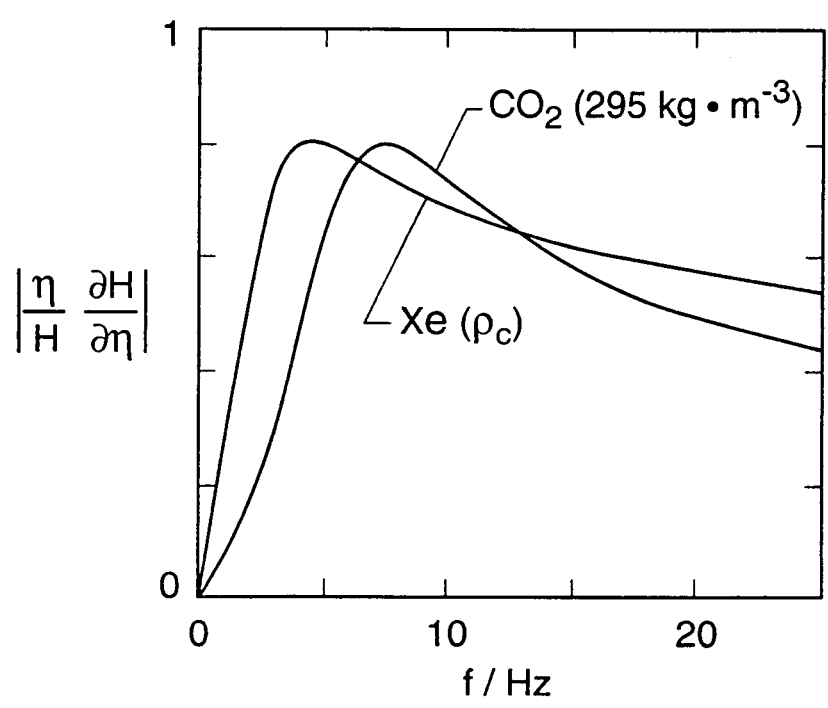
<u>frequency</u>		<u><math>Q = 0.1</math></u>	<u><math>Q = 10</math></u>
"low"	$(\omega/\omega_0 = 1/2)$	0.99	0.067
resonance	$(\omega/\omega_0 = 1)$	1	1
"high"	$(\omega/\omega_0 = 2)$	0.99	0.067

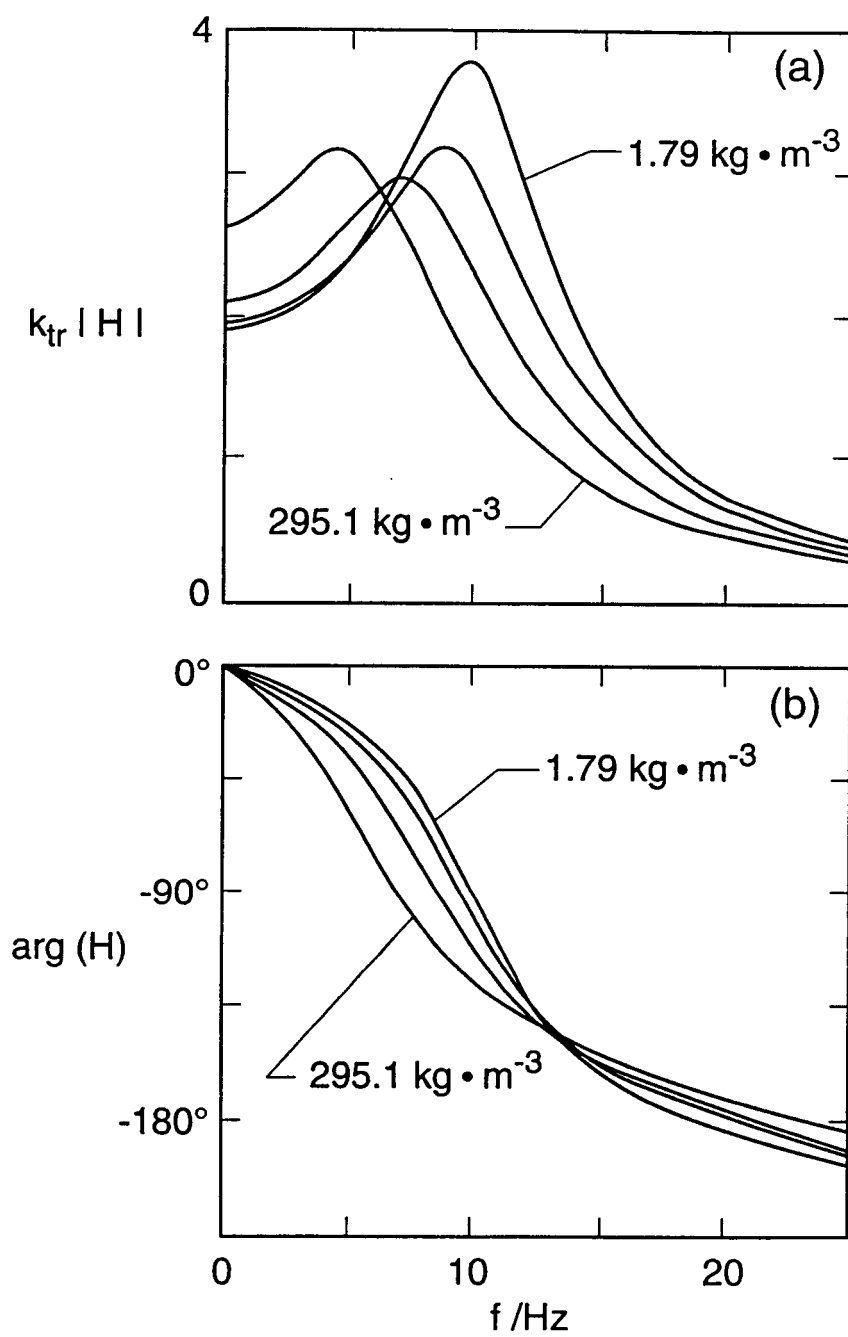
## Figures

1. The viscometer's sensitivity estimated from the model of a transversely oscillating cylinder with  $R \approx 13.8 \mu\text{m}$ . The two curves are for xenon at its critical density ( $1110 \text{ kg} \cdot \text{m}^{-3}$ ) and for  $\text{CO}_2$  at  $295.1 \text{ kg} \cdot \text{m}^{-3}$ .
2. The transfer function  $H(\omega)$  measured in  $\text{CO}_2$  at 1.79, 18.9, 90.1, and  $295.1 \text{ kg} \cdot \text{m}^{-3}$ . The lowest density data were obtained at  $25.6^\circ\text{C}$ , and the remainder were acquired at  $31.6^\circ\text{C}$ . (a) The magnitude of  $H$ . (b) The phase of  $H$ .
3. The hydrodynamic geometry function  $B(R/\delta)$  calculated using Eq.(13) from the transfer function data shown in Fig. 2. The reference length is  $R \approx 13.8 \mu\text{m}$ , the viscosity values are from Kestin, Korfali, and Sengers [5], and the points are averaged in groups of 10. The curves are calculated from the cylinder model.  
(a) The function  $(R/\delta)^2 |B|$  is plotted to reduce the strong dependence on  $R/\delta$ .  
(b) The phase of  $B$ .
4. The ratio  $|B/B_c|$  is plotted to ease examination of the results of Fig. 3. Small differences exist between data sets at high frequencies, especially above 15 Hz. There is also a frequency-independent offset between the data at 90.1 and at  $295.1 \text{ kg} \cdot \text{m}^{-3}$ . This offset is comparable to differences between viscosity values reported from different investigations at this density.
5. The function  $B/B_c$  obtained from the results of Fig. 3 after reducing the viscosity value from the data at  $295.1 \text{ kg} \cdot \text{m}^{-3}$  by 1.0%. Only data in the frequency range 1–10 Hz are plotted. Because the points fall on a single smooth curve, they are consistent with the use of hydrodynamic similarity. The pronounced deviations from the ideal cylinder calculation  $B_c$  at low frequency are to be expected: the penetration depth is half the distance between screen wires at  $R/\delta = 0.033$ . (a) The magnitude of  $B/B_c$ . (b) The phase of  $B/B_c$ .
6. The function  $B/B_c$  obtained by varying the temperature at  $242.8 \text{ kg} \cdot \text{m}^{-3}$ . For consistency in this comparison we used only data from Kestin, Whitelaw, and Zien [6]. Over the range  $0.2 < R/\delta < 0.3$  the traces of  $|B/B_c|$  obtained from the  $31.6$  and  $40.6^\circ\text{C}$  data are consistent to within a viscosity error of  $\pm 0.1\%$ . The viscosity changes by 2.9% between these two temperatures. The trace from the  $34.6^\circ\text{C}$  data is significantly higher over the same range in  $R/\delta$ , corresponding to a viscosity disagreement of as much as  $-0.2\%$ .
7. The oscillator's transfer function  $H(\omega)$  measured in  $\text{CO}_2$  at  $1.79 \text{ kg} \cdot \text{m}^{-3}$  at  $25.6$ ,  $40.6$ , and  $60.6^\circ\text{C}$ . Although, the resulting variation in the viscosity (11%) was less than that resulting from varying the density, the most accurate data sets available are for viscosity vs. temperature at low density. (a) The magnitude of  $H$ . (b) The phase of  $H$ .
8. The hydrodynamic geometry function  $B(R/\delta)$ . The agreement is excellent up to

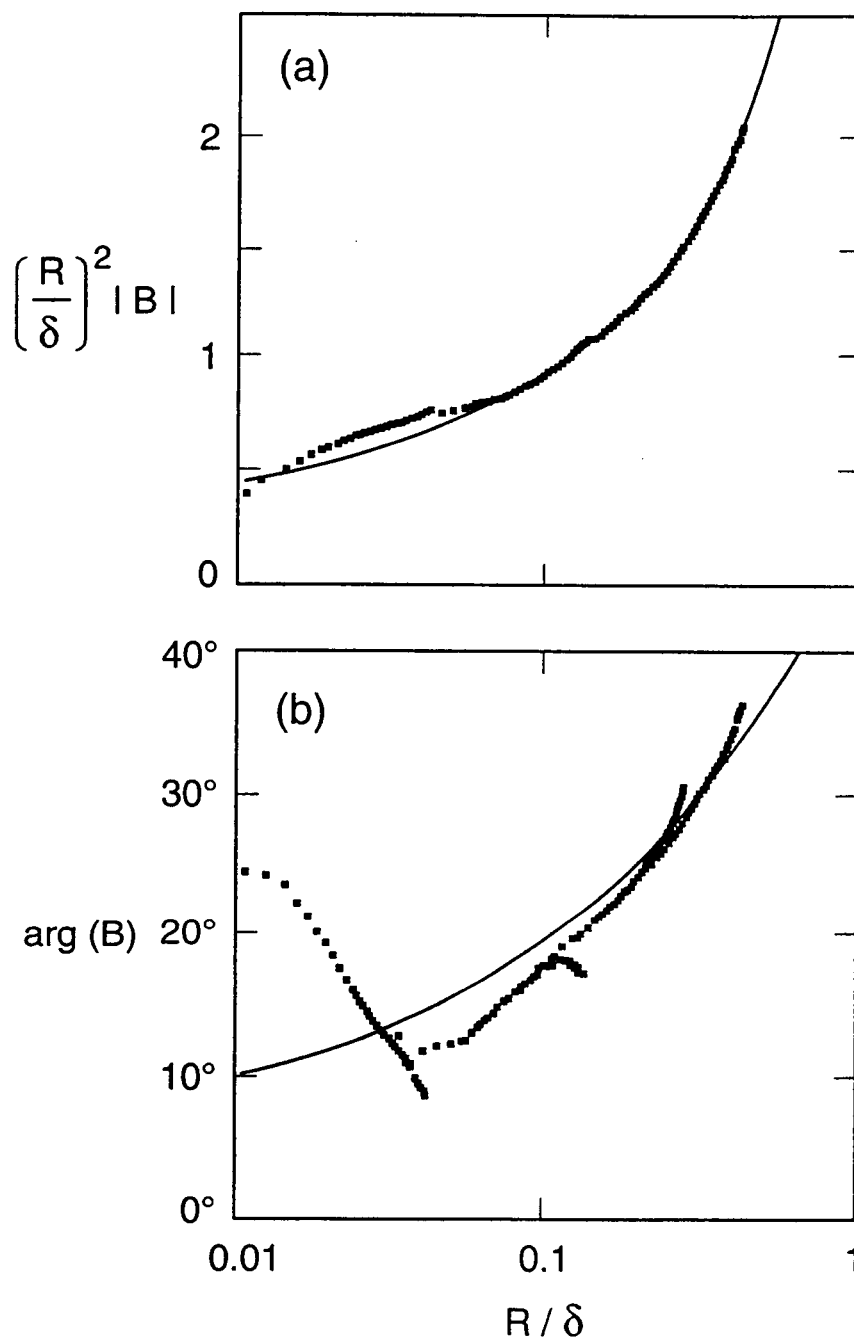
about  $R/\delta=0.028$  or about 12 Hz. At  $\pm 0.1\%$ , the corresponding error in viscosity is consistent with the data of Kestin, Ro, and Wakeham [3] to within their stated accuracy. Thus, the oscillating's screen performance is consistent with the most accurate viscosity data available. (a) The magnitude of  $B/B_c$ . (b) The phase of  $B/B_c$ .

9. The anelastic contribution to the spring constant as defined by Eqs.(13–15), measured at 23° C. (a) The real part  $k_1(\omega)$ . The curve is calculated from Eq.(20) using parameters derived from the linear description of  $k_2(\omega)$ . (b) The imaginary part  $k_2(\omega)$ . The linear description of the data, Eq.(19), was forced to go through the vacuum measurement of  $Q^{-1}$ , indicated by the lower circle. Because the low-frequency measurements were made in a degraded vacuum, viscous drag increased the apparent value of  $k_2$  at frequencies above 1 Hz. The associated increased value of  $Q^{-1}$  is indicated by the upper circle.
10. The measured temperature-dependent values of the anelastic parameters  $A_2$  and  $B_2$ , used in Eqs.(19) and (20). (a) The values of  $A_2$  were defined by the values of  $Q^1$  measured in vacuum. The curve is an empirical description of the data. (b) The values of  $B_2$  derived from plots such as Fig. 9b. The straight line is an empirical description of the data.
11. The influence of the anelastic corrections can be seen by omitting them from the analysis used to draw Fig. 8a.
12. The importance of the corrections for the four low-pass electronic filters can be seen by omitting them from the analysis used to draw Fig. 3.

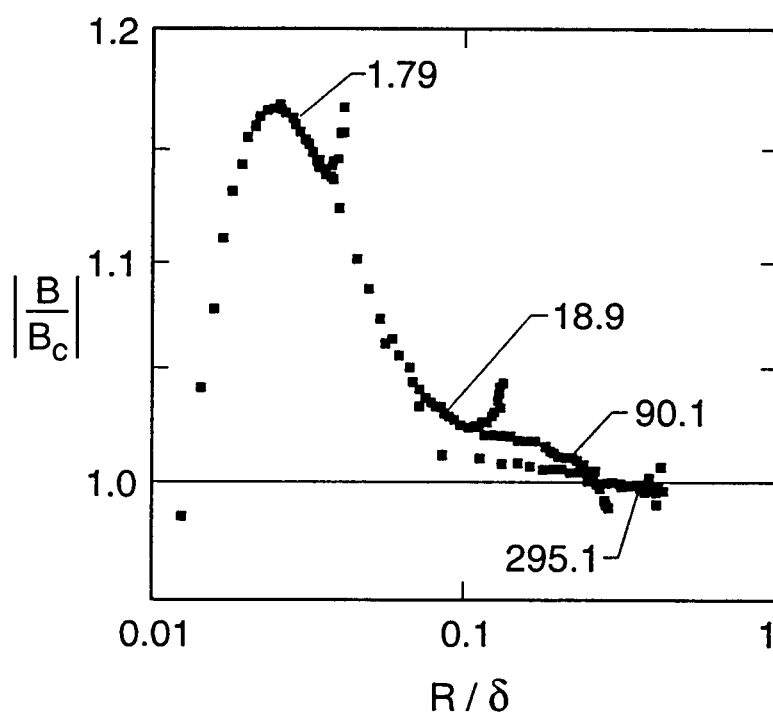


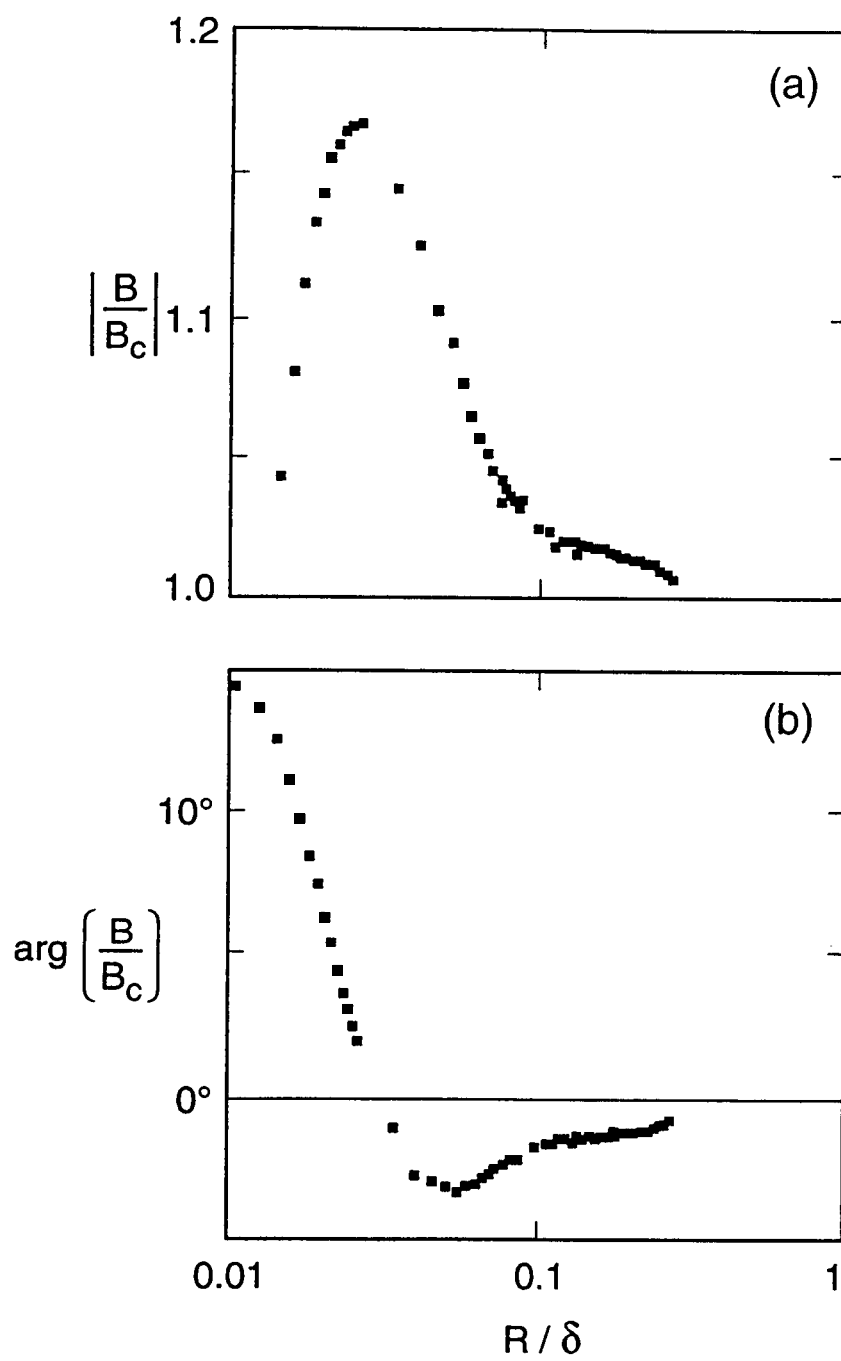


3

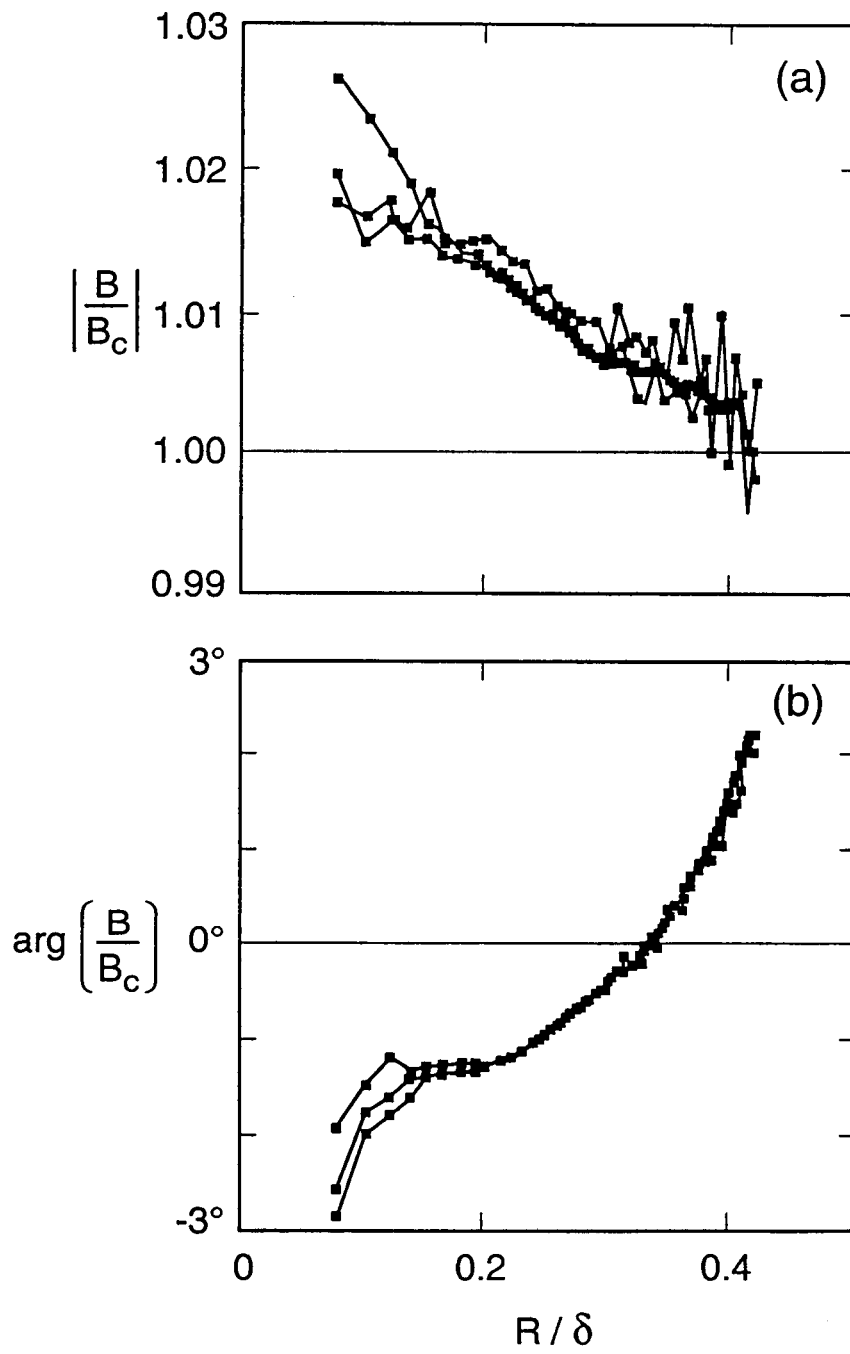


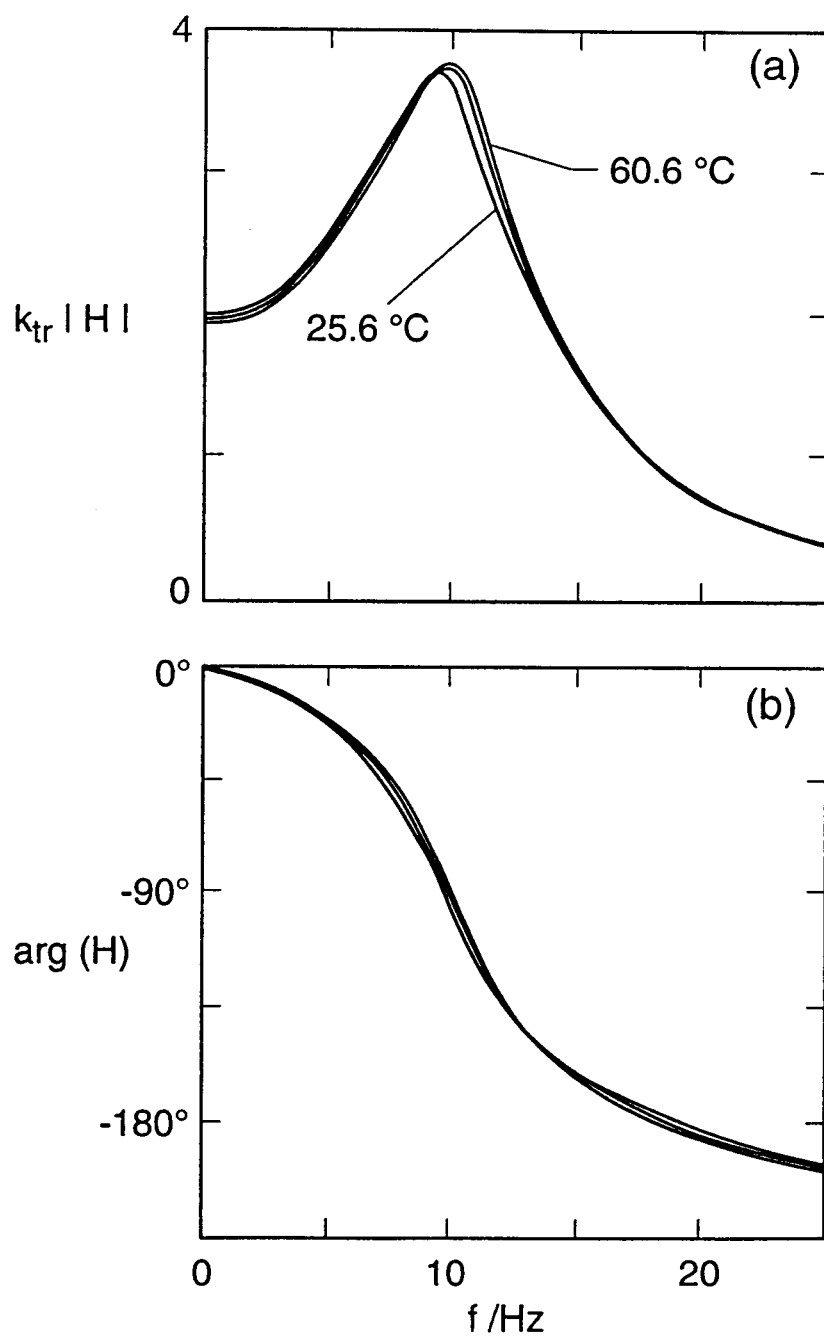
4



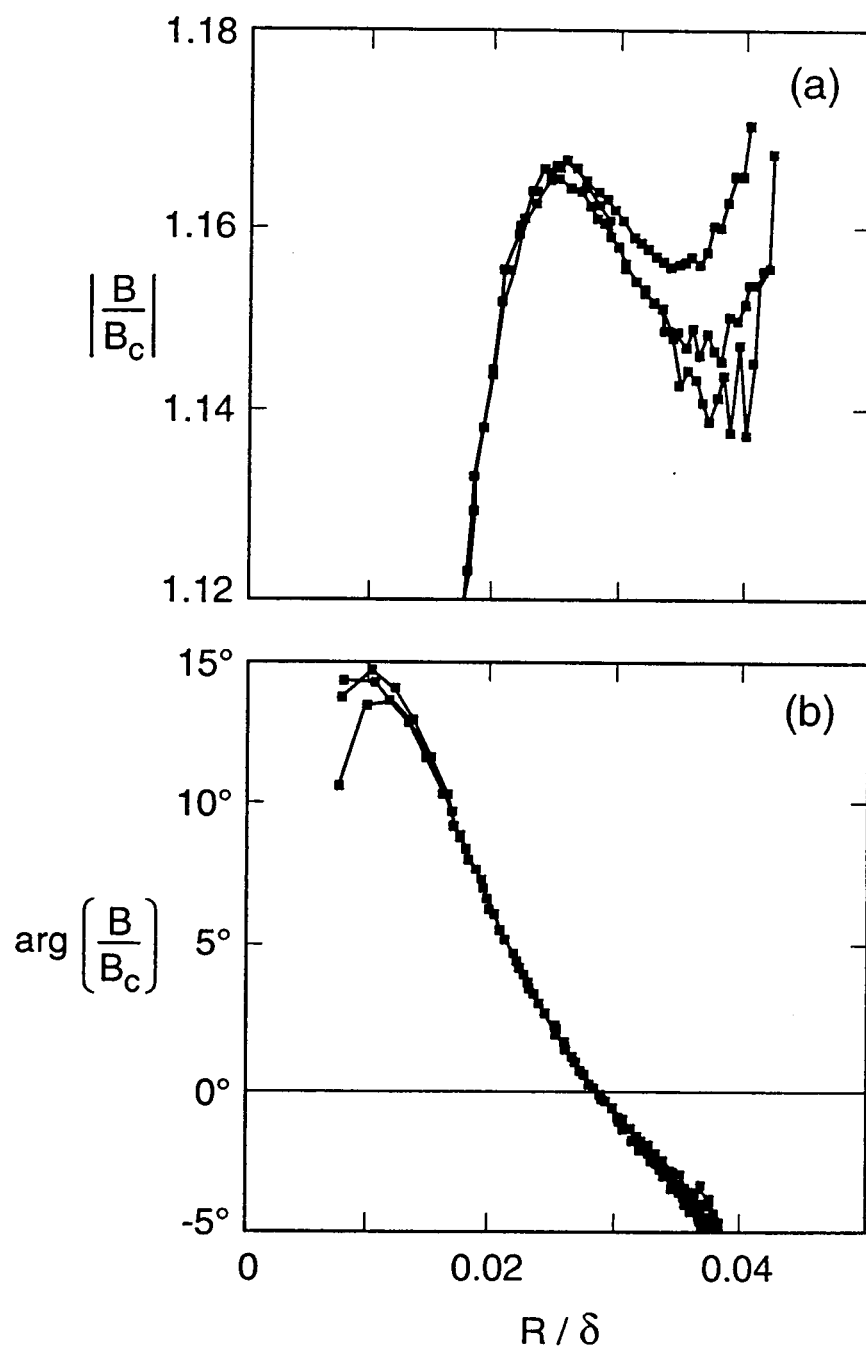


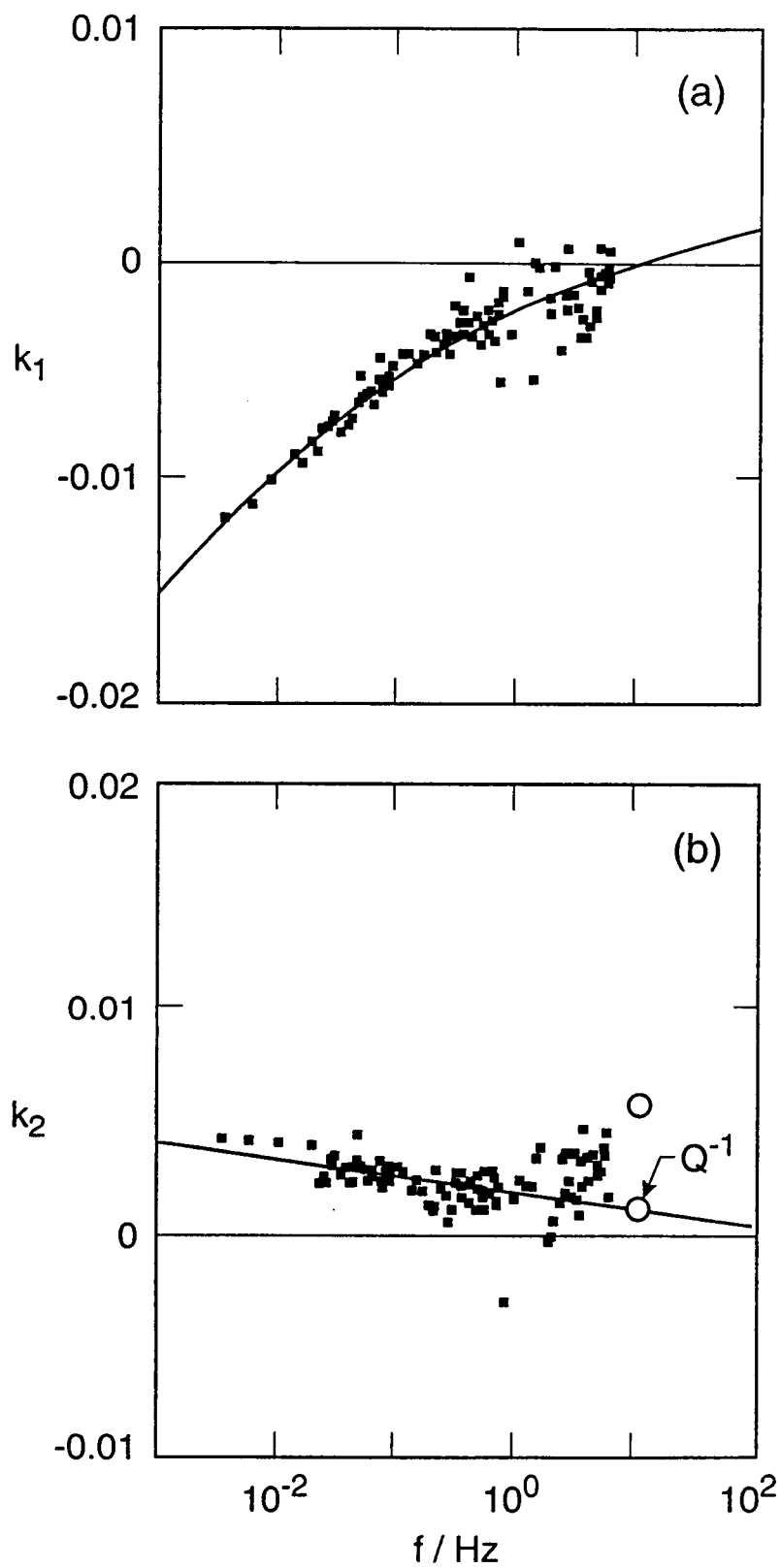
6

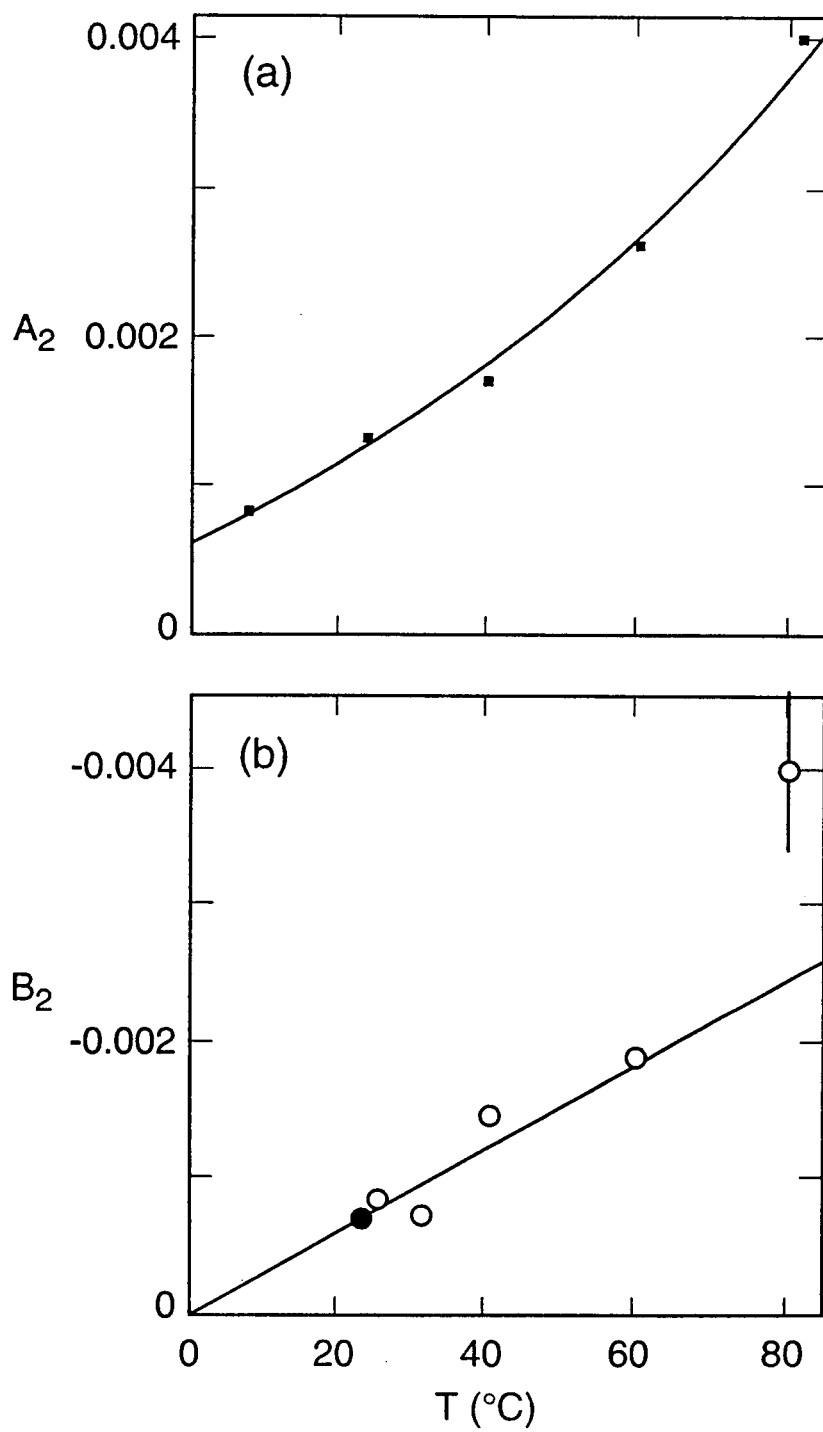




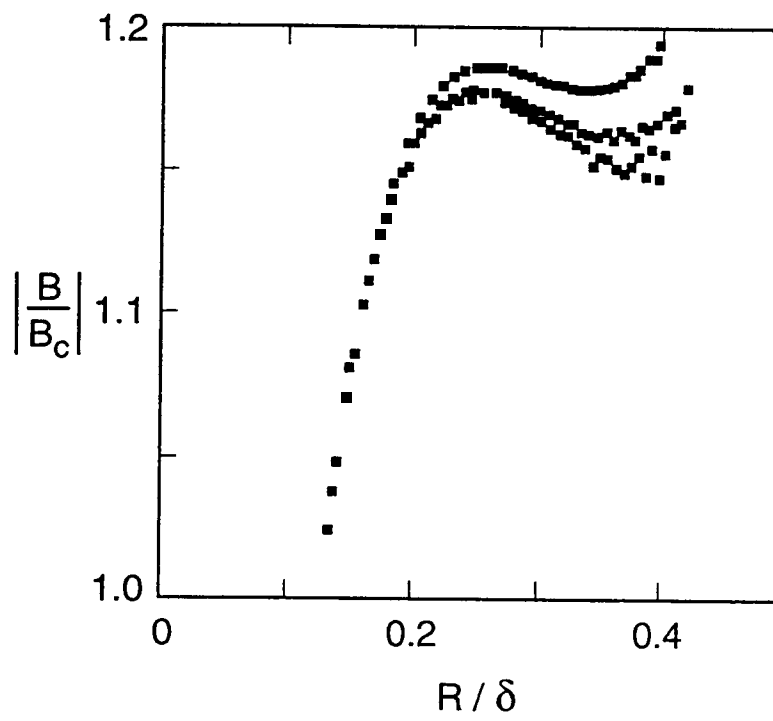
8

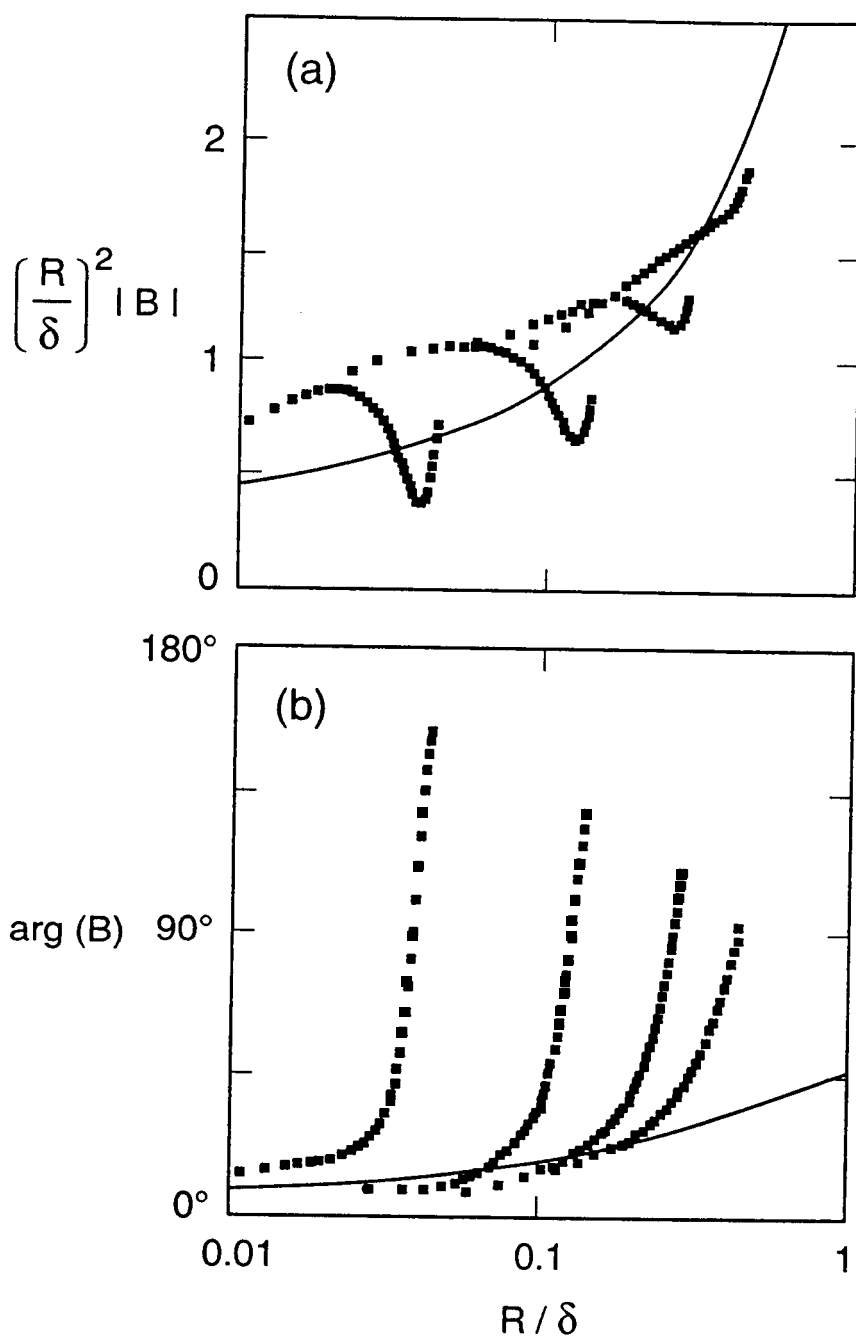






11





# NONHYDRODYNAMIC CHARACTERISTICS OF THE OSCILLATING SCREEN VISCOMETER

Robert F. Berg and Michael R. Moldover  
Thermophysics Division  
National Institute of Standards and Technology

[8 December 1993]

## Summary

Extraction of the viscosity from the oscillating screen's response function requires knowledge of its resonance frequency  $\omega_0$  and of the prefactor  $k_{tr}/k_\theta$  where  $k_{tr}$  is a transducer coefficient and  $k_\theta$  is the torsion spring constant. The determination of these parameters is described.

The effect of a possible anomaly in the dielectric constant near the critical point of xenon will be negligible.

Viscosity values are obtained from the oscillating screen viscometer by measuring the ratio of angular displacement  $\theta$  to torque  $\tau$ , namely its response function,

$$H(\omega) \equiv k_{tr} \frac{\theta}{\tau} = (k_{tr}/k_{\theta}) [(1 - \Omega^2) + i\Omega^2(\rho/\rho_s)B(\delta)]^{-1}. \quad (1)$$

The reduced frequency  $\Omega \equiv \omega/\omega_0$  is defined with respect to the undamped resonance frequency  $\omega_0$ . The oscillator's torsion spring constant  $k_{\theta}$  appears as a prefactor in combination with a transducer coefficient  $k_{tr}$ . The measurement of  $H(\omega)$  is inverted to obtain the function  $B(\delta)$  which depends only on the viscous penetration length  $\delta$ . (In practice the ratio of the density  $\rho$  of the fluid to the density  $\rho_s$  of the solid oscillator is absorbed into the function  $B(\delta)$ .) The value of  $\delta$ , and thus the viscosity, is then obtained by inverting  $B(\delta)$  [1].

Inversion of  $H(\omega)$  requires knowledge of the oscillator's characteristics, namely the parameters  $\omega_0$  and  $k_{tr}/k_{\theta}$ . The resonance frequency  $\omega_0$  is obtained by measuring its value in vacuum and then applying a small correction for the presence of the xenon sample. This correction is due to the static voltage  $V_{dc} = 30$  V which reduces the total spring constant (see Eq.(4.12) of the Science Requirements Document [2]). The linear function  $\omega_0(V_{dc}^2)$  can be measured only in vacuum. Its value in the presence of the xenon sample is derived from the vacuum measurements by correcting the slope of  $\omega_0(V_{dc}^2)$  by a factor of  $(\epsilon_c/\epsilon_0)^2$ , the square of the dielectric constant ratio.

Inversion of  $H(\omega)$  also requires knowledge of the prefactor  $k_{tr}/k_{\theta}$ . The torsion spring constant  $k_{\theta}$  has a slight frequency dependence because the oscillating screen's torsion fiber is anelastic. As a result,  $k_{\theta}$  is a complex function of frequency, namely

$$k_{\theta}(\omega) = k_0[1 + k_1(\omega) + ik_2(\omega)]. \quad (2)$$

As discussed in a previous report [1], both  $k_1$  and  $k_2$  are small and can be determined from measurements of the response function of the empty viscometer.

The transducer coefficient  $k_{tr}$  contains all factors, such as the electrode geometry and the amplifier gains, which determine the ratios between the oscillator's displacement and torque and their associated voltages. It has a small frequency dependence, due to lowpass electronic filters, which can be measured without the viscometer. (Although unnecessary in practice,  $k_{tr}$  could be generalized to include nonlinearity of the electronics as well.)

The factor  $k_{tr}/k_0$  would ideally be determined at 0 Hz. In practice  $k_{tr}/k_0$  must be measured at a nonzero frequency  $\omega'$  which is low enough to avoid significant hydrodynamic forces on the screen. We estimated the significance of hydrodynamic forces by modeling the viscometer as a sphere of radius  $R_1 \equiv 4$  mm oscillating within a larger sphere of radius  $R_2$  [3]. Setting the ratio  $R_1/R_2 \equiv 0.6$  described the low-frequency response function obtained in air at atmospheric pressure. (The modeled results changed by only a factor of two if  $R_1/R_2$  was reduced to 0.) The model predicted that  $|H/(k_{tr}/k_0)| \approx 1$ , which measures deviations from Hooke's law, drops to less than 0.1% below 0.01 Hz. Therefore, determinations of  $k_{tr}/k_0$  made at  $\omega'/2\pi \equiv 0.01$  Hz will be negligibly affected by anticipated changes of the viscosity.

The prefactor  $k_{tr}/k_0$  can be measured using the same frequency "chirp" employed for the viscosity measurements except with an upper frequency which is 32 times less (0.39 Hz instead of 12.5 Hz). A single measurement of 1024 s will then give a resolution of 1 mHz. In principle, the low-frequency measurement of  $k_{tr}/k_0$  is needed only once during the entire experiment. However, we require that the measurement be made at least once per 3 hours as a check against any slow change of  $k_{tr}$  caused by, say, drift of amplifier gain.

We anticipate no adverse effects due to a temperature dependence of the dielectric constant of xenon. Sengers et al. [4] reviewed experimental searches and the theory for a  $1-\alpha$  anomaly near the critical point. Measurements in  $^3\text{He}$  [5], Ne [6], and  $\text{SF}_6$  [7] found no anomalies greater than  $5 \times 10^{-6}$ . Xenon is a nonpolar fluid, and we expect it to behave similarly. Should any such effect exist near the critical point of xenon, its chief influence will be to change the temperature dependence of  $k_{tr}$ . This would be handled by the required low-frequency measurements of  $k_{tr}/k_0$ .

References

1. "Calibration of the oscillating screen viscometer", R.F. Berg and M.R. Moldover, report NASA Lewis Research Center (1993).
2. Science Requirements Document, report to NASA Lewis Research Center (1992).
3. "The motion of a ball oscillating in a bounded fluid: Inertial and wall effects", R. Tran-Son-Tay, B.E. Coffey, and R.M. Hochmuth, *J. Rheol.* 34, 169 (1990).
4. "Behavior of the dielectric constant of fluids near a critical point", J.V. Sengers, D. Bedeaux, P. Mazur, and S.C. Greer, *Physica* 104A, 573 (1980).
5. T. Doiron and H. Meyer, *Phys. Rev.* B17, 2141 (1978).
6. M.H.W. Chan, *Phys. Rev.* B21, 1187 (1980).
7. B.J. Thijsse, T. Doiron, and J.M.H. Levelt Sengers, *Chem. Phys. Lett.* 72, 546 (1980); B.J. Thijsse, *J. Chem. Phys.* 74 4678 (1981).

# EFFECT OF BULK VISCOSITY ON THE OSCILLATING SCREEN VISCOMETER

Robert F. Berg and Michael R. Moldover

[20 September 1993]

## Summary

Close to the critical temperature, the bulk viscosity of the xenon sample will exceed the shear viscosity by more than a factor of a billion. Nevertheless, the viscometer's low operating frequency ensures that the only significant force on the oscillating screen will be due to the shear viscosity.

The oscillating screen viscometer is intended to measure changes in the shear viscosity to an accuracy of 0.2%. However, in addition to a shearing force, the motion of the screen will also induce a slight, oscillating compressional force on the xenon. This force, in combination with the large compressibility of the xenon near its critical point, could in principle lead to additional dissipation which would complicate the experiment. This extra dissipation occurs because the force required to change a fluid's density can have a component proportional to the density's rate of change. The associated coefficient, which has the same dimensions as the ordinary shear viscosity  $\eta$ , is called the bulk viscosity  $\zeta$ . In the following we will show that the bulk viscosity is not negligible in comparison to the shear viscosity, obtain an estimate for  $\zeta$ , and then calculate the contribution of  $\zeta$  to total hydrodynamic force on the oscillating screen. The final result is that the bulk viscosity is of no concern for the planned measurement of shear viscosity.

The concept of bulk viscosity has proved useful for interpreting ultrasound experiments within the framework of conventional hydrodynamics. Accounting for compressibility in the Navier–Stokes equation requires a dissipation term in addition to the usual  $\eta \nabla^2 v$  term. This new term has the coefficient

$$\eta_L = \frac{4}{3}\eta + \zeta, \quad (1)$$

called the longitudinal viscosity.

Bulk viscosity, through its contribution to  $\eta_L$ , is believed to be important for polyatomic molecules where energy can be redistributed from translational to rotational and vibrational degrees of freedom. Although the bulk viscosity has been dismissed as negligible for monatomic gases (such as xenon) [1], it has proved to be a useful concept for the interpretation of Brillouin scattering and ultrasound experiments near the critical point. Even at temperatures as far removed from  $T_c$  as the triple point, Malbrunot et al. [2] claimed the ratio  $\zeta/\eta$  in liquid xenon to be as high as 0.3. Thus, bulk viscosity is an important consideration for the measurement of viscosity near the critical point.

Kadanoff and Swift [3] were the first to predict a divergence of the longitudinal viscosity near the critical point. Since that time, theorists have elaborated on this concept, with much work devoted to its behavior at frequencies above the fluid's characteristic relaxation frequency [4–7]. Others [8–10] have instead started with the concept of a frequency-dependent heat capacity. Although several experimental groups made comparisons of these theories with ultrasound measurements [11–14], the results were not always satisfactory. For example, Sarid and Cannell [12] reported discrepancies of as much as a factor of ten between Kawasaki's theory [4] and experimental data. Also, at high frequencies, the different theoretical approaches led to different predictions, with claims

opposed over which approach was more physically reasonable [6,10], and with papers devoted to comparisons of the different approaches [12,15].

Luckily, these troubles do not affect our estimate of the bulk viscosity. This is because we are concerned only about the simplest, low-frequency regime, where the measurement frequency  $\omega$  is less than the characteristic relaxation frequency  $\omega_D$  of the fluid, where the theories are in substantial agreement. (At the smallest reduced temperature planned,  $\epsilon=5\times 10^{-6}$ , the ratio  $\omega/\omega_D$  will exceed unity by about a factor of 5, and the bulk viscosity will have an imaginary component. However, the effects of the bulk viscosity will still be negligible.)

Because, at most, it is usually deemed merely an intermediate concept for the interpretation of ultrasound and light scattering experiments, the bulk viscosity has rarely been extracted as a separate quantity. An exception useful for our present purpose is the analysis of the ultrasound data of Mueller et al. [16] by Quentrec [17]. By considering only low-frequency data, Quentrec was able to assume that the bulk viscosity was purely real and that the dispersion relation could be simply modeled using only a single relaxation process. The derived values for the bulk viscosity of xenon on the critical isochore could then be described by the expression

$$\frac{\zeta}{\rho_c} = (2.1 \times 10^{-9} \text{ m}^2 \cdot \text{s}^{-1}) \epsilon^{-a}, \quad (2)$$

where  $\rho_c$  is critical density,  $\epsilon \equiv (T - T_c)/T_c$  is the reduced temperature, and  $a = 1.92 \pm 0.04$  is the exponent for the divergence near the critical temperature. Although Quentrec's analysis made use of a questionable adjustment of  $T_c$  by 0.10 K, 7 of the 9 data points are more than 0.5 K from  $T_c$ , so the fitted values in Eq.(2) were not sensitive to this adjustment. Also, the exponent is consistent with Kawasaki's prediction [6] of

$$a = 2 - \frac{\alpha}{2} = 1.94, \quad (3)$$

where  $\alpha=0.11$  is the exponent associated with the constant volume specific heat.

Eq.(2) can now be extrapolated to the closest reduced temperature planned for the Critical Viscosity Experiment, namely  $\epsilon=2\times 10^{-6}$ . The result is  $\zeta/\rho_c = 184 \text{ m}^2 \cdot \text{s}^{-1}$ , or a viscosity ratio of

$$\frac{\zeta}{\eta} = 3 \times 10^9. \quad (4)$$

The effect of the bulk viscosity on the oscillating screen can now be estimated by calculating its contribution to the hydrodynamic force felt by a cylinder oscillating transversely in a viscous, compressible fluid. Exactly this problem was addressed by

Gitterman [18,19]. The two important wavevectors in the problem are defined by

$$k_1^2 \equiv \frac{i\omega\rho}{\eta} \quad (5)$$

and

$$k_2^2 \equiv \omega^2 \left[ c^2 + \frac{i\omega}{\rho} \left[ \frac{4}{3}\eta + \zeta \right] \right]^{-1}, \quad (6)$$

where  $c$  is the low-frequency velocity of sound [20]. For the case  $|k_2 R| < 1$ , where  $R$  is the cylinder's radius, Gitterman expressed the force  $F$  on the cylinder as

$$\frac{-F}{i\pi\rho R^2 \omega u} = \frac{2K_2(k_1 R)}{K_0(k_1 R)} - 1 - \frac{K_2^2(k_1 R)}{K_0^2(k_1 R)} \left[ (k_2 R)^2 \ln(k_2 R) + \frac{i}{2}(k_2 R)^2 \right] \quad (7)$$

Here,  $u$  is the cylinder's velocity and  $K_0(z)$  and  $K_2(z)$  are Kelvin functions. For the usual incompressible case, corresponding to the limit  $k_2 R = 0$ , the term in square brackets disappears, and Eq.(7) reduces to the result first derived by Stokes. Though of course nonzero, the magnitude of  $k_2 R$  will be only

$$|k_2 R| \approx \frac{\omega R}{c} \leq \frac{(2\pi \cdot 10 \text{ Hz})(1.4 \times 10^{-5} \text{ m})}{(>50 \text{ m.s}^{-1})} < 2 \times 10^{-5}. \quad (8)$$

This is because, at 10 Hz, a wavelength of sound is much greater than the cylinder's radius.

The planned Critical Viscosity Experiment will operate at  $|k_1 R| \approx 0.3$ . By substitution of the small argument approximation

$$\frac{K_2(z)}{K_0(z)} \approx \frac{-2}{z^2 \ln(z)}, \quad (9)$$

for the ratio of the Kelvin functions, the terms in Eq.(7) containing  $(k_2 R)$  are seen to give a correction to the incompressible result of magnitude

$$\left[ \frac{|k_2 R|}{|k_1 R|} \right]^2 \frac{\ln|k_2 R|}{\ln|k_1 R|} < \left[ \frac{2 \times 10^{-5}}{0.3} \right]^2 \frac{\ln(2 \times 10^{-5})}{\ln(0.3)} = 4 \times 10^{-8}, \quad (10)$$

which is completely negligible. Thus, in spite of its large divergence near the critical point, the bulk viscosity will not interfere with the measurement of the shear viscosity.

## References

1. P.M. Morse and K.U. Ingard, Theoretical Acoustics (Princeton Univ. Press, Princeton, 1968).

2. P. Malbrunot, A. Boyer, E. Charles, and H. Abachi, Phys. Rev. A 27, 1523 (1983).
3. L.P. Kadanoff and J. Swift, Phys. Rev. 166, 89 (1968).
4. K. Kawasaki, Phys. Rev. A 1, 1750 (1970).
5. Y. Shiwa and K. Kawasaki, Prog. Theor. Phys. 66, 406 (1981).
6. K. Kawasaki and Y. Shiwa, Physica 113A, 27 (1982).
7. D.M. Kroll and J.M. Ruhland, Phys. Lett. 80A, 45 (1980); D.M. Kroll and J.M. Ruhland, Phys. Rev. A 23, 371 (1981).
8. L. Mistura, J. Chem. Phys. 57, 2311 (1972).
9. J.K. Bhattacharjee and R.A. Ferrell, Phys. Rev. A 24, 1643 (1981); J.K. Bhattacharjee and R.A. Ferrell, Phys. Lett 86A, 109 (1981).
10. R.A. Ferrell and J.K. Bhattacharjee, Phys. Rev. A 31, 1788 (1985).
11. C.W. Garland, D. Eden, and L. Mistura, Phys. Rev. Lett. 25, 1161 (1970); D. Eden, C.W. Garland, and J. Thoen, Phys. Rev. Lett. 28, 726 (1972); J. Thoen and C.W. Garland, Phys. Rev. A 10, 1311 (1974).
12. D. Sarid and D. S. Cannell, Phys. Rev. A 15, 735 (1977).
13. D.B. Roe and H. Meyer, J. Low Temp. Phys. 30, 91 (1978).
14. J.A. Cowan and J.W. Leech, Can J. Phys. 61, 895 (1983).
15. H. Tanaka and Y. Wada, Phys. Rev. A 32, 512 (1985).
16. P.E. Mueller, D. Eden, C.W. Garland, and R.C. Williamson, Phys. Rev A 6, 2272 (1972).
17. B. Quentrec, J. Phys. -Lett. 40, L-257 (1979).
18. M. Gitterman, Il Nuovo Cimento, 25B, 328 (1975).
19. M. Gitterman, Rev. Mod. Phys., 50, 85 (1978).
20. C.W. Garland and R.D. Williams, Phys. Rev. A 10, 1328 (1974).

## THE NEED FOR COMMUNICATION WITH THE CRITICAL VISCOSITY EXPERIMENT

Robert F. Berg  
[5 May 1993]

The principal investigators will need the ability to communicate with the Critical Viscosity Experiment in flight. Although the nominal plan calls for the experiment to proceed automatically, communication ability will greatly reduce the chance of experiment failure.

Examples of technical problems which could be mitigated by communication include an unexpected shift in the apparent critical temperature and an unexpected, prolonged period of severe vibration. The first problem could be corrected by modifying the temperature control schedule. The second problem could be mitigated by taking additional data in the affected temperature range.

Examples of problems due to unexpected sample behavior include difficulty in automatically resolving  $T_c$  and unexpectedly long equilibration times. The former might be handled by manual analysis and the latter would require a change in the temperature schedule.

Real-time communication is not necessary. For the examples cited above, the slow speed of the viscosity experiment's temperature sweeps would make tolerable communication delays of as much as one hour. Full control of the experiment or complete reporting of all acquired data is also not necessary. For example, only an occasional interrogation of the oscillator's frequency response would be needed to verify its proper operation.

The Critical Point Facility which flew on IML-1 experienced thermometry difficulties about 50 mK in amplitude. This would have been disastrous for the Thermal Equilibration Experiment had it been allowed to run automatically according to the nominal plan. However, observation of the apparent shift in  $T_c$  allowed the TEQ investigators to partially compensate for the problem by reprogramming the CPF's temperature control schedule. An additional problem, peculiar to TEQ, was that the planned method for excitation of density gradients by stepping the temperature proved ineffective. This also was mitigated during the flight by reprogramming the stirrer to create transient temperature gradients. The experience with CPF convinced us of the value of communication with the experiment.

FEASIBILITY OF ELECTROSTRICTION  
FOR MEASUREMENT OF THE CRITICAL TEMPERATURE  
IN THE CRITICAL VISCOSITY EXPERIMENT

Robert F. Berg and Michael R. Moldover  
Thermophysics Division  
National Institute of Standards and Technology  
Gaithersburg, MD 20899

[10 March 1993]

The large compressibility of a pure fluid near its critical point is a potential means of measuring the critical temperature. At the suggestion of Prof. Ferrell we observed electrostriction in xenon by applying a large voltage across a small, open capacitor immersed in the sample and then measuring the capacitance change caused by the subsequent increase in the xenon's local density. This scheme was attractive because the compressibility is a large, well-understood effect and because we were already familiar with low-voltage capacitance measurements. We found qualitative agreement with our initial expectations based on the fluid's compressibility. However, we also found an additional effect comparable in size to the expected electrostriction but proportional to the applied voltage. We have no explanation for this effect. Thus, given the Science Panel's recommendation against investing extensive effort in this direction, we are abandoning further development of an alternate means for measuring the critical temperature.

### Background

Near the critical temperature  $T_c$  the compressibility  $\chi$  is very large, and it is associated with the exponent  $\gamma=1.24$  through the relation

$$\chi \sim t^{-\gamma} \quad (1)$$

where  $t$  is the reduced temperature. To derive the critical temperature to a precision  $\Delta T_c$  from measurements of  $\chi$  at a reduced temperature  $t$  near  $T_c$ , the precision  $\Delta\chi$  must be

$$\frac{\Delta\chi}{\chi} \simeq \gamma \frac{\Delta T_c}{t T_c} = (1.24) \frac{(2.9 \times 10^{-5} \text{ K})}{(2 \times 10^{-6})(290 \text{ K})} = 0.06, \quad (2)$$

where  $t$  was chosen as the reduced temperature closest to  $T_c$  where viscosity data will be acquired.

We estimated the expected density change caused by the electric field  $E$  by equating the shift in the chemical potential per unit mass  $\mu$  with the change in the electrostatic energy density. In the limit of a small density change  $\Delta\rho$ , this is

$$\rho_c [\mu(\rho_c + \Delta\rho, T) - \mu(\rho_c, T)] = \frac{1}{2}(\epsilon_c - \epsilon_0)E^2. \quad (3)$$

Here,  $\epsilon_0$  is the vacuum permittivity, and  $\epsilon_c$  is the permittivity of xenon at the critical density  $\rho_c$ . Using the cubic model [1] for the equation of state of xenon near its critical point, Eq.(3) becomes

$$\frac{\Delta\rho}{\rho_c} = \frac{\Gamma(\epsilon_c - \epsilon_0)E^2}{2P_c} t^{-\gamma}, \quad (4)$$

where  $\Gamma=0.058$  is the amplitude of the reduced susceptibility and  $P_c=5.84$  MPa is the critical pressure.

The Clausius-Mossotti relation connects the change in the dielectric constant to the change in density according to

$$\frac{\rho}{\epsilon} \frac{\partial \epsilon}{\partial \rho} = \frac{\epsilon - \epsilon_0}{\epsilon}. \quad (5)$$

Thus the shift  $\Delta C$  in the measured capacitance is

$$\frac{\Delta C}{C_{\text{cell}}} = \left[ \frac{\epsilon_c - \epsilon_0}{\epsilon_c} \right] \left[ \frac{\Delta\rho}{\rho_c} \right] \left[ \frac{C_1}{C_{\text{cell}}} \right], \quad (6)$$

where the sensitivity of the measurement is reduced by the ratio of the fluid-filled portion of the capacitor  $C_1$  to the total capacitance  $C_{\text{cell}}$ .

The magnitude of the electric field is constrained by upper and lower bounds. The desired signal-to-noise ratio limits the minimum allowed electric field. Very large electric fields can lead to undesirable effects such as dielectric breakdown or a shift in  $T_c$  [1].

However, a more restrictive upper bound is the requirement that the fluid's susceptibility not be significantly affected by the density change. Using the cubic model again, this limit is

$$E = \left[ \frac{2aP}{(\epsilon_c - \epsilon_0)} \left[ \frac{(\Delta\chi/\chi)}{\gamma b^2} \right]^{1/2} \right]^{1/2} t^{\beta\delta/2} = 1.3 \times 10^5 \text{ V/m}, \quad (7)$$

where  $\beta=0.325$  and  $\delta=4.815$  are critical exponents,  $b^2=1.28$ , and  $a=15.4$  is a cubic model parameter [1]. The numerical result for  $E$  assumed a minimum reduced temperature of  $t=2 \times 10^{-6}$  and an allowed error of  $\Delta\chi/\chi=0.06$ , estimated in Eq.(2).

#### Measurements by others

Although sensitive capacitance measurements have been employed in pure fluids to characterize gravity-induced stratification (e.g. [2]) and to search for an anomaly in the dielectric constant (e.g. [3]), they were all low-voltage ( $< 20$  V) techniques. We are unaware of previous measurements of electrostriction near the liquid-vapor critical point. In contrast, there are numerous reports of a "nonlinear dielectric effect" near the consolute point of binary mixtures (e.g. [4]). Most of these latter experiments made use of a rapid pulse technique, inappropriate for our expected long equilibration times. The theory associated with the binary mixture measurements is based on induced anisotropy of the concentration fluctuations [5]. However, when we applied the predictions [6] of this model to xenon we found a negligible effect in comparison to electrostriction. Therefore, other than our use of the cubic model equation of state, we received little guidance from theory and previous experiments.

#### Apparatus

There were several constraints in the capacitor's design. First, the gap containing the xenon between the capacitor's plates needed to be small to avoid problems with long thermal relaxation times. Second, the capacitor needed to be small enough to be added to the existing viscometer. Third, the capacitor needed to be mechanically stable and made out of materials unlikely to contaminate the xenon. Our design, indicated in Fig. 1, consisting of a sandwich of copper and glass soldered together with indium, met all three requirements. The gap size was determined by the 0.18 mm thick glass spacers (microscope cover slips), and other dimensions of the capacitor were near the limit of easy manual construction.

Our measurements made use of a cylindrical cell similar to that described in the Science Requirements Document. The screen oscillator and its associated electrodes were not present. Instead, a tuning fork mixer (unused in these tests) and the capacitor were placed into positions determined by their attachments to electrical feedthroughs located at the end of the cell. The cell was filled to within 0.3% of the critical density. Weighing showed that less than 0.03% of the sample leaked out over the next 46 days.

Two circuits were used to measure the cell's capacitance while applying a DC bias voltage. We first used a circuit, shown in Fig. 2, similar to that used for the oscillating screen. Problems with the stability of the reference capacitor and the 10 kHz oscillator prompted the use of a commercial capacitance bridge and a synthesized 10 kHz source, indicated in Fig. 3.

#### Technique

We considered two methods for locating  $T_c$  in the low-gravity experiment. The simplest would be to maintain a large voltage across the capacitor and observe the

"signature" of capacitance changes associated with crossing  $T_c$ . Slow systematic errors such as drift of the electronics would be unimportant provided the capacitance signal changed sufficiently rapidly near  $T_c$ . Unfortunately, because of the planned minimum ramp speed of  $3 \times 10^{-8}$  K/s and the complicating effects of equilibration in the capacitor gap very close to  $T_c$ , we have no theory to reliably associate  $T_c$  with the observed signature to the desired precision of  $29 \mu\text{K}$ .

The second method would avoid the equilibration problem by using capacitance measurements made only at  $0.6 \text{ mK}$  and more above  $T_c$ . The required extrapolation places a greater burden on the measurement's accuracy, indicated by Eq.(2) above. Obtaining the required accuracy would be eased by the use of a difference method, namely observing the change in capacitance following a change in the bias voltage, after allowing sufficient time for equilibration.

The thermal time constant associated with density relaxation in the capacitor gap following a change in the electric field can be calculated from xenon's thermal diffusivity  $D_T$  and the gap size  $2x_0$ . For example, at  $1 \text{ mK}$  above  $T_c$ ,

$$\tau = \frac{x_0^2}{\pi^2 D_T} = \frac{(9 \times 10^{-5} \text{ m})^2}{\pi^2 (6 \times 10^{-12} \text{ m} \cdot \text{s}^{-2})} = 1.4 \times 10^2 \text{ s}, \quad (8)$$

compatible with the time of a viscosity measurement. Eq.(8) assumes a reduction in  $\tau$  by the factor of four applicable to closed, effectively one-dimensional systems near the critical point [7]. A better estimate would require a more careful accounting of thermodynamics in the presence of an inhomogeneous electric field [8].

#### Electrical parameters and the signal-to-noise ratio.

With the bridge of Fig. 3 driven at  $10030 \text{ Hz}$  at five to ten volts amplitude, the lock-in gain was typically set to give an output sensitivity of one to three  $\text{kV/pF}$ . The measured total capacitance was typically  $C_{\text{cell}} = 25.4 \text{ pF}$ . The bridge's dissipation setting depended much more strongly on frequency than on temperature. The equivalent parallel resistance was  $2 \times 10^8 \text{ ohms}$  at  $10 \text{ kHz}$ , but this increased linearly to  $8 \times 10^9 \text{ ohms}$  at  $100 \text{ Hz}$  (compatible with "DC" measurements of  $\geq 2 \times 10^{11} \text{ ohms}$ ).

The circuit's output wandered slowly under typical operating conditions. As a result there was a roughly "1/f" noise spectrum below  $5 \text{ Hz}$ . Above  $5 \text{ Hz}$  the noise was limited by the lock-in's preamp to  $2 \times 10^{-6} \text{ pF/Hz}^{1/2}$ . We observed similar behavior when measuring a fixed silver mica capacitor at room temperature.

We do not know the source of the low-frequency noise. One possibility considered was the temperature dependence of the capacitance bridge, rated at less than  $5 \times 10^{-6} \text{ K}^{-1}$ . However, the noise observed at  $0.1 \text{ Hz}$  would then correspond to temperature noise in the bridge's  $100 \text{ pF}$  standard of at least  $4 \times 10^{-3} \text{ K/Hz}^{1/2}$ .

#### Relaxation following a change in the bias voltage

Using the circuit of Fig. 2, we observed the evolution of the apparent capacitance following a change in the bias voltage. At  $19$  and  $48 \text{ mK}$  above  $T_c$  we observed relaxation characterized by time constants in the range of five to ten seconds, consistent to within a

factor of two with calculations using Eq.(8). At 98 mK above  $T_c$ , very little relaxation was seen on this time scale.

We also found unusually slow relaxation behavior at all temperatures. This unexplained behavior was characterized by a  $10^{-4}$  pF drift over several hundred seconds in the same direction as the "proportional effect" described below.

#### Low-voltage measurements of capacitance vs. temperature

Fig. 4 plots our measurements of capacitance as a function of temperature. Above  $T_c$  the relative change of  $3.4 \times 10^{-4} \text{ K}^{-1}$  was about 10 times larger than expected from the thermal expansion of the capacitor. Below  $T_c$  the data were fit by a function incorporating the known coexistence curve of xenon and the free parameters  $T_c$  and  $C_1$ , the fluid portion of the capacitor. We found  $T_c = 16.655 \pm 0.005 \text{ }^\circ\text{C}$  and  $C_1 = 3.14 \pm 0.01 \text{ pF}$ , where the errors were estimated from fits optimized through trial and error.

#### Measurements of capacitance vs. voltage

The electrostriction measurements were complicated by an unexpected apparent capacitance change proportional to the applied bias voltage and whose sign depended on the "polarity" of connections made to the cell. This can be seen in the typical data of Fig. 5 taken at 48 mK above  $T_c$ . Most of this "proportional effect" took place within one second. A much slower, subsequent drift, proportional to the voltage change, was also seen. Both effects hindered our efforts to unambiguously measure the electrostriction.

Fig. 6 shows the temperature dependence of the proportional effect. The effect remained when the capacitor was removed and measured in air.

Fig. 7 shows measurements of the observed "quadratic effect", believed to be caused by electrostriction. The proportional effect was removed by using the average of measurements taken at bias voltages of +150 V and -150 V. A calculation of the expected capacitance change is also plotted. For the calculation, which relied on no free parameters, we used the values of  $C_1$  and  $T_c$  found from the two-phase measurements. The dominant uncertainty, the capacitor gap  $d$ , is indicated by the two curves calculated with the values  $d = 0.16$  and  $0.18 \text{ mm}$ .

The calculated curve describes the data only qualitatively. We neglected the effects of density stratification close to  $T_c$ , and the errors close to  $T_c$  are of the same sign as

expected from such neglect. Far from  $T_c$  the errors are  $2 \times 10^{-4} \text{ pF}$  or smaller, though much greater than the expected values. Because of its comparable size, the unexplained proportional effect may be the source of these latter errors.

#### Further work

No further work on electrostriction is planned. The encountered technical problems, in particular the proportional effect and the associated slow drift following changes in the bias voltage, prevent the accurate location of  $T_c$  with the present apparatus. Assuming these effects were due to an unintended asymmetry in the capacitor, they could be eliminated by a different choice of capacitor materials or by an improved cleaning technique.

We also considered the use of a large AC bias voltage as a means of eliminating the proportional effect. Use of the capacitance bridge's 10 kHz drive voltage for this purpose would require addressing the possible effects of electronic crosstalk and of detector nonlinearity. In any case, the proportional effect seen with DC bias voltages must be

either reduced or understood sufficiently to trust the results of measurements made with AC bias voltages.

After demonstrating the accuracy of electrostriction measurements for locating  $T_c$ , the device could be incorporated into the viscometer only after proving that it would not interfere mechanically or electrically with the viscosity measurements.

# References

1. "Gravity effects in fluids near the gas-liquid critical point", M.R. Moldover, J.V. Sengers, R.W. Gammon, R.J. Hocken, Rev. Mod. Phys. 51, 79 (1979).
2. "Density and compressibility of oxygen in the critical region", L.A. Weber, Phys. Rev. A 2, 2379 (1970). "Equation of state and critical exponents of  $^2\text{He}$  and a  $^3\text{He}$ - $^4\text{He}$  mixture near their liquid-vapor critical point", Phys. Rev. B 20, 3678 (1979).
3. Dielectric constant anomaly of polar and nonpolar fluids near their critical point", M.W. Pestak and M.H.W. Chan, Proceedings of the Eighth Symposium on Thermophysical Properties, p.467 (ed. J.V. Sengers, ASME, New York, 1981).  
"Behavior of the dielectric constant of fluids near a critical point", J.V. Sengers, D. Bedequeux, P. Mazur, and X.C. Greer, Physica 104A, 573 (1980).
4. "The influence of pressure and temperature on the critical properties of a nitrobenzene-hexane solution by the NDE method", J. Chrapec, Š.J. Rzoska, and J. Ziolo, Phase Transitions 5, 49 (1985).
5. "Droplet model for the analysis of the dielectric properties of critical binary mixtures", J. Goulon, J.-L. Greffe, and D.W. Oxtoby, J. Chem. Phys. 70, 4742 (1979).
6. "Induced birefringence and electric permittivity changes in critical binary liquids", W. Pyzuk, J. Phys. Chem. 90, 699 (1986).
7. R.P. Behringer, H. Meyer, and A. Onuki, J. Low Temp. Phys. 81, 71 (1990).
8. "Thermodynamics of a fluid substance in the electrostatic field", J. Chem. Phys. 23, 2023 (1955).

### Figures

1. The electrostriction capacitor. It was fixed in a plane tilted about  $30^\circ$  from vertical with one open end near the cell's midline.
2. The circuit used to observe the electrostriction time constant.
3. The circuit used for most of the electrostriction measurements relied on a General Radio model 1615 capacitance bridge.
4. Low-voltage measurements of the capacitance as a function of temperature. The slope above  $T_c$  was about 10 times greater than expected from the thermal expansion of copper. The temperature dependence below  $T_c$  could be described by the known liquid and vapor densities of saturated xenon.
5. Observed changes of the capacitance from an arbitrary zero. Note the expected quadratic shape is modified by an additional "proportional effect". The scatter in the data reflect ambiguity caused by slow drift associated with the proportional effect.
6. The size of the the proportional effect. Although it depended on temperature, it was present even after xenon was removed from the cell (not shown).
7. The magnitude of the electrostriction effect, defined from the average of the measurements at  $-150$  V and  $+150$  V. The curves are calculations, with no free parameters, of the expected amplitude. The main uncertainty is the capacitor gap  $d$ , defined by the 0.18 mm thick glass spacers. Far from  $T_c$  the measurements are complicated by the presence of the proportional effect and its associated drift. The complications of gravity-induced stratification close to  $T_c$  were not included in the calculation.

copper sheet  
8 x 9 mm

indium

indium-coated  
glass cover slip  
0.18 mm thick

wire soldered  
to sheet

